Recombinant protein-based scaffolds:

extracellular secretion, purification, and mineralization

By:

Zahra Abdali

Department of Chemical Engineering

McGill University

Montreal, Quebec

Spring 2022

A thesis submitted to McGill University in partial fulfillment of the requirements of the degree of
Doctor of Philosophy

© Zahra Abdali

Abstract

Recombinant proteins are biocompatible material sources, and their simple genetics makes their manipulation easy for different clinical applications. Their hierarchical organization and well-defined morphology make them suitable templates for bio-inspired mineralization. Specifically, collagen is a common scaffold for mineralization and fabrication of biomaterials, due to its high content of carboxylate groups.

Recombinant streptococcal collagen-like proteins have been widely used as an alternative source of collagen. Because of their high content of proline and charged residues, they have thermal stability comparable to type I collagen. Bacterial collagen has been previously produced intracellularly in *Escherichia coli (E. coli).* However, its intracellular expression demands cell lysis for extraction, which combined with costly chromatography methods, limits its scalability.

Here, we studied the possibility of using the curli secretion system to secrete recombinant proteins that we then purified using simple and scalable methods. The curli extracellular secretion pathway is natively found in *E. coli* and consists of components necessary for the secretion and assembly of an amyloid protein called CsgA. CsgA is composed of five pseudo-repeats and assembles into curli fibers after secretion. Here, we secreted bacterial collagen and CsgA-like proteins from *E. coli* and investigated their potential for use as mineralization scaffolds.

As a first attempt, we removed the internal repeats of CsgA and replaced them with hydroxyapatite (HAP)-binding peptide, thus using CsgA to assemble the short peptide. X-ray diffraction and TEM showed the functionality of the HAP-binding domain for the formation of HAP crystals. Overall, we demonstrated that CsgA can still be secreted extracellularly after being genetically modified and that its fusion with the HAP-binding peptide makes the protein specific for interacting with HAP crystals.

Next, we used the curli secretion pathway for the extracellular secretion of bacterial collagen. We removed the components that are specific for the secretion and assembly of CsgA. We confirmed the secretion of a considerable fraction of triple helical collagen (~70%) into the extracellular medium, with ~50% purity in the crude supernatant. This study was proof of the concept that the curli secretion pathway is non-specific to CsgA. We also introduced protocols (based on digestion, filtration, and precipitation) for the simple isolation of bacterial collagen. We characterized the morphology and secondary structure of the isolated collagen, concluding that the final collagen structure is process-dependent.

Next, we studied the processability of bacterial collagen. Through its silicification, bacterial collagen held a porous gel-like structure that could be shaped using molds. We also used collagen for nucleation and assembly of HAP and silver nanoparticles. Driven by its charged residues, collagen provided controlled nucleation of these particles. We highlighted the advantages of combining bacterial collagen with inorganic particles to expand their applications in the field of biomaterials and tissue engineering.

Overall, in this thesis, we showed the use of the curli secretion system for efficient secretion of recombinant proteins, the simple and scalable purification of bacterial collagen, and finally highlighted the potential of recombinant proteins as a scaffold for mineralization.

Résumé

Les protéines recombinantes sont des sources de matériaux biocompatibles et leur génétique simple facilite leur manipulation pour différentes applications cliniques. Leur organisation hiérarchique et leur morphologie bien définie en font des modèles appropriés pour la biominéralisation. Plus précisément, le collagène est un échafaudage couramment utilisé pour la

minéralisation et la fabrication de biomatériaux, en raison de sa teneur élevée en groupes carboxylate.

Les protéines recombinantes de type collagène streptococcique ont été largement utilisées comme source alternative de collagène. En raison de leur forte teneur en proline et en résidus chargés, elles ont une stabilité thermique comparable au collagène de type I. Le collagène bactérien a déjà été produit de manière intracellulaire dans *Escherichia coli* (*E. coli*). Cependant, son expression intracellulaire nécessite une lyse cellulaire pour l'extraction, qui, combinée à des méthodes de chromatographie coûteuses, limite son évolutivité.

Ici, nous avons étudié la possibilité d'utiliser le système de sécrétion curli pour sécréter des protéines recombinantes que nous avons ensuite purifiées à l'aide de méthodes simples et évolutives. La voie de sécrétion extracellulaire curli se trouve nativement dans *E. coli* et se compose de composants nécessaires à la sécrétion et à l'assemblage d'une protéine amyloïde appelée CsgA. CsgA est composé de cinq pseudo-répétitions et s'assemble en fibres curli après sécrétion. Ici, nous avons sécrété du collagène bactérien et des protéines de type CsgA à partir d'*E. coli* et étudié leur potentiel d'utilisation comme échafaudages de minéralisation.

D'abord, nous avons supprimé les répétitions internes de CsgA et les avons remplacées par un peptide de liaison à l'hydroxyapatite (HAP), utilisant ainsi CsgA pour assembler le peptide court. La diffractométrie de rayons X et la TEM ont montré la fonctionnalité du domaine de liaison HAP pour la formation de cristaux HAP. Dans l'ensemble, nous avons démontré que la CsgA peut encore être sécrétée de manière extracellulaire après avoir été génétiquement modifiée et que sa fusion avec le peptide de liaison HAP rend la protéine spécifique pour interagir avec les cristaux HAP.

Ensuite, nous avons utilisé la voie de sécrétion curli pour la sécrétion extracellulaire de collagène bactérien. Nous avons supprimé les composants spécifiques de la sécrétion et de l'assemblage de CsgA. Nous avons confirmé la sécrétion d'une fraction considérable de collagène triple hélicoïdal (~ 70 %) dans le milieu extracellulaire, avec une pureté d'environ 50 % dans le surnageant brut. Cette étude était la preuve du concept que la voie de sécrétion curli est non spécifique à CsgA. Nous avons également introduit des protocoles (basés sur la digestion, la filtration et la précipitation) pour l'isolement simple du collagène bactérien. Nous avons caractérisé la morphologie et la structure secondaire du collagène isolé, concluant que la structure finale du collagène dépend du processus.

Ensuite, nous avons étudié la transformabilité du collagène bactérien. Grâce à sa silicification, le collagène bactérien a conservé une structure poreuse semblable à un gel qui pouvait être façonnée à l'aide de moules. Nous avons également utilisé du collagène pour la nucléation et l'assemblage de nanoparticules de HAP et d'argent. Poussé par ses résidus chargés, le collagène a fourni une nucléation contrôlée de ces particules. Nous avons mis en évidence les avantages de combiner le collagène bactérien avec des particules inorganiques pour étendre leurs applications dans le domaine des biomatériaux et de l'ingénierie tissulaire.

Dans l'ensemble de cette thèse, nous avons montré l'utilisation du système de sécrétion curli pour une sécrétion efficace de protéines recombinantes, la purification simple et évolutive du collagène bactérien, et, enfin, mis en évidence le potentiel des protéines recombinantes comme échafaudage pour la minéralisation.

Acknowledgments

First, I would love to sincerely thank my amazing supervisor, Professor Noémie-Manuelle Dorval Courchesne. Starting my Ph.D. program under the supervision of an intelligent, supportive, open-minded professor with a prestigious academic background was the greatest opportunity of my life. Joining her lab helped me to learn from her fresh high-quality experiences and challenges to find the best path for my future. She was always open to new ideas and discussing new projects. She gave me the opportunity to take on many leadership tasks while she was setting up her new lab, which was a remarkable experience during my graduate program.

I would like to thank Professors Corinne Hoesli, Showan Nazhat, Christopher Moraes, and Matthew James Harrington that kindly accepted to be the committee members for reviewing my Ph.D. proposal and annual reports and advising me through these years. Professor Harrington welcomed me to his lab and let me use the facilities with the kind help of his students Max Renner-Rao and Mostafa Rammal.

I would like to thank all of my colleagues and lab mates especially Dalia, Daniel, Mario, Masoud, and Angie. Aside from the outside the lab amazing times that we had together, I had a great time with them in the lab and office. We always had great discussions about our projects and how to troubleshoot the problems, which made me stay motivated. And I thank all my friends outside the lab especially Isabel, Naghmeh, Darya, and Shima. They all made me miss my family less.

I would like to thank all the staff in the Chemical Engineering Department for all their help and training, especially our former graduate coordinator, Mrs. Louise Miller-Aspin, Ranjan Roy, Frank Caporuscio, and Andrew Golsztajn.

During my Ph.D., I had the opportunity to work with eleven talented undergraduate students and two master's students, Armita Amini, Alexander Lambert, Scott Jian, Xiaodan Zhu, Alexander Bevacqua, Elia Benchekroun-Jolicoeur, Lei Wang, Coralie Jabra Khabbaz, Xinxin Hao, Pew Dey, Riley Sun, Amy Chow, and Angie Cai. I would like to thank them for the opportunity to teach them about bio-derived materials and for their passion and perseverance.

Finally, I would love to thank my parents, who taught me to be a tough but kind person, a forgiver but firm and a hard worker, always wanting the best and most but being happy and satisfied with the little but precious things, like seeing their smile on the phone screen, when video calling. My brothers, sister, and my nephew are the meaning of having a real family that is always beside you, loves, and supports you unconditionally, no matter who I am or where I am. I am so lucky and thankful for having them.

This work is dedicated to all the kids in the world that are deprived of the basic rights, education, safety, food, play, and the love of their parents.

Table of contents

List of figures

of collagen, where CsgB and CsgA are removed (top, right). CsgE and CsgG are necessary for both pathways. (B) Distribution of collagen in the bacterial culture after separation of the pellet and supernatant. Detection of His-tagged collagen in each fraction via Western Blot (right) and its representative stained SDS-PAGE gel (left). 1: bacterial culture, 2: supernatant, 3: pellet. (C) The modified secretion pathway where CsgB, CsgA, CsgC, and CsgF components are removed, and the corresponding gene arrangement. CsgA, CsgB, CsgC, and CsgF are only necessary when secreting curli fibers. (D) The extracellular secretion of collagen in the bacterial culture through the modified pathway shown by SDS-PAGE. Distribution of the collagen in the bacterial collagen after separation of the pellet and supernatant related to the different modified vectors, 1: pET21d-v'cl-csgCEFG, 2: pET21d-v'cl-csgEFG, 3: pET21d-v'cl-csgEG. (E) SEM images of bacterial cultures expressing collagen, showing extracellular fibrillar structures. (F, G) Observation of secreted triple helical structures from collagen-secreting PQN4 cells. Images of Sirius Red stained cultures are taken both under the light microscope (F) and polarized light microscope (G). The triple helical structure of the collagen appears red under the polarized light, compared with the untransformed PQN4 cells, indicating the collagen secreted extracellularly was able to form a stable triple helix. Scale bars: 20 µm. 90

Figure 4. 2. Purification of extracellular collagen using scalable methods. (A) Scheme of two scalable purification methods: digestion/precipitation or (D-P, top) and digestion/cross-flow filtration (D-CF, bottom). After the filtration, the collagen domain (CL) will be trapped in the retentate and the digested variable domain (V') and other small digested proteins will be removed through permeate. The supernatant is first separated from bacterial cells via centrifugation and digested with pepsin. It is then subjected to separation via precipitation or filtration. (B) SDS-PAGE analysis of the purified collagen samples showed comparable purity with collagen/Ni and

List of tables

List of abbreviations

3D	Three-dimensional
AFM	Atomic force microscopy
AgNp	Silver nanoparticle
Arg (R)	Arginine
Asp (D)	Aspartic acid
CD	Circular Dichroism
CL domain	Collagen-like domain
CL/D-CF	Collagen obtained from pepsin digestion of supernatant followed by filtration with 30 kDa MWCO centrifugal filter.
CL/D-P	Collagen obtained from pepsin digestion of supernatant followed by acid precipitation.
E. coli	Escherichia coli
EDS	Energy-dispersive X-ray spectroscopy
ELP	Elastin-like polypeptides
GdmCl	Guanidinium chloride
Gln (Q)	Glutamine
Glu ()	Glutamic acid
Gly (G)	Glycine
HAP	Hydroxyapatite
HFIP	Hexafluoroisopropanol
HisTag	Six-histidine tag
Hyp	Hydroxyproline
LB	Lysogeny broth
Lys (K)	Lysine
MBP	Maltose-binding proteins
NCP	Non-collagenous protein
OD	Optical density
P4H	Prolyl-4-hydroxylase
Pro	Proline
SBF	Simulated body fluid
SDS	Sodium dodecyl sulfate

SEM	Scanning electron microscopy
TEE	Translational enhancing element
TEM	Transmission electron microscopy
TFA	Trifluoroacetic acid
UV-Vis	Ultraviolet-visible
V domain	Variable domain
V’	Variable domain + N22 + His-tag + translation enhancing element
V’CL/CF	Collagen was obtained from filtration with 50 kDa and 30 kDa MWCO centrifugal filter.
V’CL/Ni	Collagen obtained from Ni-NTA
WT	Wild-type
XRD	X-ray diffraction

Thesis preface

This is a manuscript-based thesis and consists of the following three manuscripts:

1. **Curli-Mediated Self-Assembly of a Fibrous Protein Scaffold for Hydroxyapatite Mineralization**

Zahra Abdali, Masoud Aminzare, Xiaodan Zhu, Elizabeth DeBenedictis, Oliver Xie, Sinan Keten, and Noémie-Manuelle Dorval Courchesne

(2020) ACS Synth. Biol., 9, 12, 3334–3343

2. Extracellular Secretion and Simple Purification of Bacterial Collagen from *Escherichia coli*

Zahra Abdali, Max Renner-Rao, Amy Chow, Anqi Cai, Matthew J. Harrington, and Noémie-Manuelle Dorval Courchesne

(2022) Biomacromolecules, 23, 4, 1557–1568

3. Bacterial Collagen-Templated Synthesis and Assembly of Inorganic Particles

Zahra Abdali, Masoud Aminzare, Amy Chow, Noémie-Manuelle Dorval Courchesne

(2022) In preparation

Chapter 1. Introduction

The high market demand for protein-based materials necessitates a scalable and safe method for their fabrication. As opposed to proteins from animal sources, bacterial recombinant proteins are not a concerning source for transmitting viral animal diseases, therefore, they have been used widely for biomaterials and cosmetic products manufacturing.

In this thesis, we study the recombinant production of two self-associating bacterial proteins that are inherently secreted on the surface of *Streptococcus pyogenes* and *Escherichia coli* bacteria, and their use for biomineralization. Recombinant Streptococcal collagen-like proteins have been used as an alternative for animal collagen, because of their structural similarities and thermal stability compared with type I animal collagen. CsgA protein is another recombinant protein, inherently secreted by *Escherichia coli*, that assembles into curli amyloid fibers after extracellular secretion. CsgA and bacterial collagen are tolerant to genetic engineering and have been genetically modified to produce functional recombinant proteins.

Simplifying the production of recombinant proteins, from the expression step to purification, will help with their massive production.

Through bacterial intracellular secretion systems, the protein of interest is susceptible to protease digestions, and cell rupturing is required for extraction of the proteins, thus, potentially affecting the activity and functionality of the recombinant proteins and complicating the downstream process. A simple downstream process is a big step toward scaling up the production of recombinant proteins. The current chromatography-based methods for purification of the proteins are costly and time-consuming for large volumes of samples, despite the high purity that they

provide. Using an extracellular secretion system and a simple non-chromatography could confront these challenges.

The main goals of this thesis are to use recombinant bacterial collagen for bio-inspired mineralization, extracellularly produce it using the adapted curli secretion system, and purify it using simple non-chromatography methods. We started with a modified CsgA that was fused to a hydroxyapatite-binding peptide and used it as a scaffold for hydroxyapatite mineralization.

1.1. Research Objectives

The main objectives of this thesis are as follows:

1. To verify if the CsgA protein could be minimized, keeping only essential sequence components for assembling peptides that do not self-assemble by themselves, such as a hydroxyapatite-binding peptide.
2. To adapt and modify the curli secretion pathway for the extracellular secretion of bacterial collagen, as a non-CsgA protein.

3. To establish a simple, fast, and scalable method for the purification of bacterial collagen.

4. To investigate the potential of CsgA-like proteins and bacterial collagen for the nucleation of inorganic particles.

2.1. Thesis organization

Chapter 2 provides background information about recombinant proteins, their extracellular secretion, and purification. We also review the literature on bacterial collagen and curli proteins, their applications, and secretion pathway. Finally, we focus on proteins as a scaffold for bioinspired mineralization.

Chapter 3 presents a self-assembly mechanism for short functional peptides that we derived from curli. We use the curli self-assembly system to assemble a free functional peptide (hydroxyapatite-binding peptide) into fiber-like structures that can subsequently aggregate to form macroscopic hydrogel biomaterials. In addition, we verify that modified CsgA protein (after being truncated and fused with a functional peptide) could still be secreted extracellularly. The final engineered CsgA protein serves as a scaffold for hydroxyapatite mineralization and opens up broader applications for curli in biomaterials fields and bone tissue engineering.

Chapter 4 demonstrates that the minimized curli secretion pathway, with only the essential genes for the extracellular secretion of non-CsgA proteins, can be used to direct bacterial collagen into the extracellular medium. In addition, we introduce a simplified downstream process for scalable and fast purification of bacterial collagen. Using these approaches (extracellular secretion and scalable purification) enable the use of bacterial collagen for a range of biomedical applications and the development of biomaterials with collagen as their main component.

Chapter 5 highlights the potential of bacterial collagen as a scaffold for nucleation and mineralization of inorganic particles, such as hydroxyapatite crystals, silver nanoparticles, and silica particles. The bacterial collagen-based composites consisting of inorganic particles broaden the applications of bacterial collagen in the field of biomaterials and tissue engineering especially the bone regenerative scaffolds

Chapter 6 includes the concluding remarks and suggestions for future works.

3.1. Contribution of authors

The original contributions of the authors are summarized below:

1. **Curli-Mediated Self-Assembly of a Fibrous Protein Scaffold for Hydroxyapatite Mineralization**

Authors: Zahra Abdali, Masoud Aminzare, Xiaodan Zhu, Elizabeth DeBenedictis, Oliver Xie, Sinan Keten, and Noémie-Manuelle Dorval Courchesne

Contributions: The idea of truncating the CsgA protein was initiated by Dr. Dorval Courchesne, Zahra Abdali, and Oliver Xie, and the method for removing the internal repeats, adding the HAP-binding peptide, and synthesizing the gene using overlapped PCR were suggested by Zahra Abdali. Zahra Abdali genetically modified CsgA protein and purified them, characterized the proteins and mineralized them, and wrote the original draft of the manuscript. Masoud Aminzare conducted transmission electron microscopy and X-ray diffraction of the mineralized samples, Xiaodan Zhu, an undergraduate student, helped with the synthesis of the gene for the fusion of the hydroxyapatite peptide and vacuum filtration, Elizabeth DeBenedictis, from Northwestern University, Department of Mechanical Engineering, conducted the molecular dynamics modeling of the modified structures of the CsgA under supervision of Dr. Keten. Oliver Xie helped with atomic force microscopy of the proteins.

2. **Extracellular Secretion and Simple Purification of Bacterial Collagen from *Escherichia coli***

Authors: Zahra Abdali, Max Renner-Rao, Amy Chow, Anqi Cai, Matthew J. Harrington, and Noémie-Manuelle Dorval Courchesne

Contributions: The idea of using the curli secretion system for the extracellular secretion of bacterial collagen was initiated by Dr. Dorval Courchesne and Zahra Abdali, and the protocols for scalable purification were suggested by Zahra Abdali.

Zahra Abdali modified the curli secretion pathway, produced bacterial collagen, characterized the proteins, and wrote the original draft of the manuscript. Max Renner-Rao conducted the Sirius Red staining and Raman spectroscopy of the purified samples under the supervision of Dr. Harrington. Amy Chow helped with crosslinking the samples. Anqi Cai helped with obtaining the thermal unfolding curves in the revision step.

3. **Bacterial Collagen-Templated Synthesis and Assembly of Inorganic Particles**

Authors: Zahra Abdali, Masoud Aminzare, Amy Chow, Noémie-Manuelle Dorval Courchesne

Contributions: The idea of using bacterial collagen as a scaffold for the three inorganic particles was initiated by Zahra Abdali and Dr. Dorval Courchesne. Zahra Abdali fabricated the mineralized samples, characterized them, and wrote the original draft of the manuscript. Masoud Aminzare conducted X-ray diffraction and energy-dispersive X-ray spectroscopy of the mineralized samples. Amy Chow helped with the synthesis of the collagen/silver nanoparticle samples and colony counting antibacterial test.

In all three manuscripts, Dr. Dorval Courchesne supervised the projects. All authors reviewed the manuscripts, with the bulk of the editing being performed by Dr. Dorval Courchesne.

Chapter 2. Background

2.1. Recombinant collagen

There is a tremendous need for protein-based materials from safe and biocompatible sources in different fields from biotechnology and biomaterials to cosmetic products. Specifically, collagen is one of the most common proteins with a wide variety of applications in the field of biomaterials and tissue engineering. [1] Collagen is defined by its characteristic triple-helix structure and the unique $(Gly\text{-}Xaa\text{-}Yaa)_n$ repeating sequence, with X and Y often being proline (Pro). About 10% of the Pro residues are normally post-translationally modified to 4-hydroxyproline (Hyp) using the prolyl-4-hydroxylase (P4H) enzyme. This modification is crucial for several reasons: 1) it increases the thermal stability of collagen, with melting temperature around 37 °C through hydration; [2] 2) by its circular structure, proline creates and strengthens the triple helix; [3, 4] 3) it is the target for interaction with certain receptors. [4] All types of collagens, fibrillar and non-fibrillar, contain a triple-helical domain composed of three chains that are linked by water-mediated interactions and hydrogen bonds between the amine functional group, from glycine (Gly), and the carbonyl group from Pro in X position of another chain (Figure 2.1).

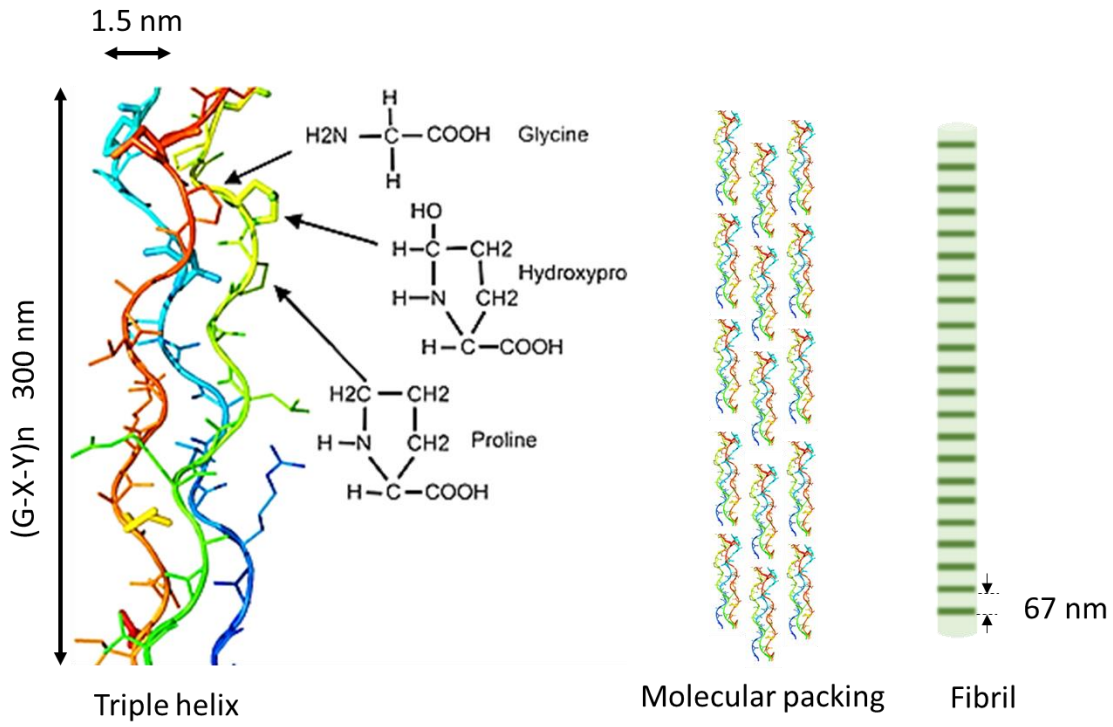

Figure 2. 1. The triple helix structure of animal collagen, assembly, and molecular packing for the formation of fibrils. Adapted from [5]

The global collagen market size has been estimated at USD 8.36 billion in 2020 and is expected to reach USD 16.7 billion by 2028, [6] with extensive applications in various clinical applications, such as wound healing, cardiovascular disease, skincare, and cosmetic surgery. However, specifications associated with the testing of animal-based products, possible disease transmission and contamination with pathogens, and slaughtering of the massive population of animals hinder the immense manufacturing of animal collagen. There are other sources of animal collagen with a lower risk of immunogenicity and inflammation, such as avian, fish, and jellyfish. However, after all the hydrolysis and treatment for the extraction, no triple-helix structure remains in the collagen and the extracted product is like a soluble protein that usually needs to be combined with other biopolymers for the fabrication process. [7]

Compared with animal sources, recombinant proteins are safer sources, and their simple and well-understood genetics makes it easy to modify and manipulate them for different clinical applications. [8] Therefore, the field of recombinant protein production has been developed to introduce efficient expression systems that allow the formation of recombinant collagen safely. For example, a variety of approaches have been used to make recombinant animal collagen constructs using different organisms. Contrary to animal cells, plant and microbial systems lack the P4H enzyme, thus, it needs further genetic engineering for this modification. However, it is not easy to achieve a high yield of post-translational modification in these systems. [5] Therefore, recombinant bacterial collagen-like proteins, with no need for post-translation modifications have been used as an alternative for animal collagen (*Table 2. 1*).

Table 2. 1. The common systems have been used for the expression of different collagens (According to [2]).

Organism	Post-translational modification	Reference
Animal collagen expression systems		
Transgenic mice	Endogenous P4H enzyme	[9]
Transgenic silkworm		[10]
Plant	✓ No inherent hydroxylation ✓ Add P4H enzyme	[11]
Micro-organisms: *Escherichia coli* (*E. coli*), *Pichia*		[12]
Bacterial/Non-animal collagen expression		
Streptococcus pyogenes	No need for the P4H enzyme and post-translational modification	[13]
E. coli		[14]

2.2. Recombinant bacterial collagen

Sequnces that resemble animal collagen, with Gly at every third residue and high proline content, have also been found in bacteriophages and bacteria. [15] Although bacteria lack the P4H enzyme and cannot post-translationally modify Pro to Hyp, there are several expressed bacterial collagen-like proteins that can form stable triple-helix structures. Streptococcal proteins (Scl1 and Scl2) are some of the most characterized triple helical collagen-like proteins found on the cell surface of group A Streptococcus pyogenes.[2] Scl2 consists of variable N-terminal globular domain (V domain) and a collagen-like helical domain (CL domain), with repeating $(Gly\text{-}Xaa\text{-}Yaa)_n$ sequence. Although this protein lacks Hyp residues for stabilization, the thermal stability of the triple-helix still is comparable to the type I animal collagen. [16] This stability comes from a high content of Pro (~12%) and charged residues (~30%) which together can support electrostatic stabilization of the triple-helix (Figure 2.2). [17] Table 2. 2 summarizes the structural comparison between bacterial collagen and type I animal collagen.

Table 2. 2. Structural comparison between bacterial collagen and type I animal collagen

	Animal Collagen	**Streptococcal collagen**
Number of amino acids	Type I collagen (α1): 1464 (488 triplets) Reference: UniProt- P02452 (CO1A1_HUMAN)	237 (79 triplets)
Size of the triple helix	5 nm diameter 300 nm length	1 nm diameter 50 nm length
The mechanism the for stabilitythe of triple helix	Post-translational modification of Pro to Hyp and formation of hydrogen bonds.	The high content of charged amino acids and proline
Proline content (%)	19	12
Content of charged amino acids (%)	Asp (4.5) + Glu (5.1) + Lys (3.9) + Arg (4.8) = 18.3	Asp (8.4) + Glu (7.2) + Lys (8.9) + Arg (5.1) = 29.6

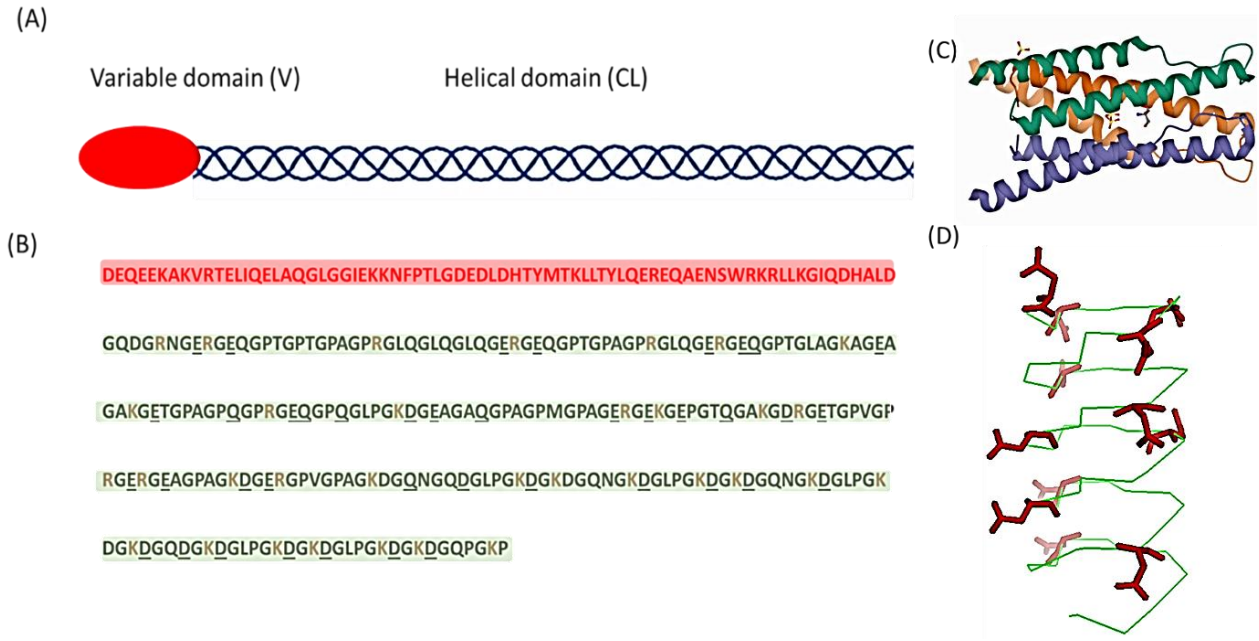

*Figure 2. 2. (A) Bacterial collagen consists of a variable domain and helical domain. (B) The helical domain consists of the high content of charged residues (brown color amino acids: positively charged (*Arginine (R) and Lysine (*K*)*), underlined amino acids: negatively charged (*Aspartic acid (*D*), Glutamic acid (*E*)), (C) Crystal structure of the globular domain from streptococcal collagen-like protein (PDB DOI: 10.2210/pdb4NSM/pdb), (D)Helical structure of bacterial collagen (domain position: 247 to 306) and accumulation of aspartic acid (UniProtKB - Q8RLX7 (Q8RLX7_STRPY)).*

The exact mechanism of triple helix formation and assembly of bacterial collagen, in the absence of Hyp, is not well understood but is mainly dependent on the electrostatic interactions between the charged amino acids. Near the C-terminal end of bacterial collagen, there are several repeats of sequence GKD-GKD-GQN-GKD-GLP, which play a key role in the stabilization of the triple helix. In addition, there are many GQN repeats, which contain glutamine (Q), a polar residue, and can support a hydration network in the collagen-like domain. [15]

2.3. Applications of bacterial collagen

Streptococcal collagen is non-immunogenic, non-toxic, and non-thrombogenic. [16, 17] Therefore, there is no concern regarding its biocompatibility for use in the field of biomaterials and tissue engineering. However, bacterial collagen lacks any active biological sites for interaction with cell surface receptors and other extracellular matrix molecules. Therefore, it has been genetically and non-genetically modified to improve its bioactivity and provide new functionalities. The addition of integrin and fibronectin-binding domains for cell adhesion applications, [18] a fusion of silk and elastin domains to improve mechanical properties, [19] and photo crosslinked poly(ethylene glycol) diacrylate and bacterial collagen hydrogel for tissue-engineered vascular grafts [20] are some of the reported modifications of bacterial collagen. Integrin-incorporated bacterial collagen was used to be grafted on Titanium. After grafting, bacterial collagen maintained its potency for osteoblast cells adhesion and differentiation, increased the accumulation of Ca^{2+}, and inhibited bacterial attachment and biofilm formation. [21] Table 2. 3 summarizes some of the modifications of the bacterial collagen and their applications.

Table 2. 3. Different modifications were introduced to the bacterial collagen.

Introduced modifications	New function/application	Reference
Genetic modification		
Integrin binding domains (GLPGER, GFPGER, GFPGEN, GERGFP, GERGVE) using site-direct mutagenesis	Higher affinity to integrin receptors and improving the adhesion of endothelial cells for cardiovascular substitutes.	[18, 22]
Fibronectin binding domain (GLA-GQR-GIV-GLP-GQR-GER)	Binding to fibronectin specifically at its gelatin binding domain.	[23]
Fusion of silk tag $(GAGAGS)_n$ and elastin $(GAGAGS)_n$ to the C-terminal of the bacterial collagen	Improving the mechanical properties without introducing chemical crosslinking agents.	[19]

Chemical modification		
Chemically binding with Poly(ethylene glycol) diacrylate and using a photo-crosslinking agent	Improving the gelation and the strength of bacterial collagen	[20]

2.4. Bacterial production of recombinant proteins - Extracellular secretion

Bacterial collagen has been genetically modified previously and produced intracellularly in *E. coli* for biomedical applications. [18, 24-26] In these reports, cell lysis has been used as a necessary step for extracting intracellular collagen. However, there are some downsides to conventional intracellular production of proteins compared with extracellular secretion.

When the recombinant proteins are expressed and localized in the cytoplasm, there is a high risk of their accumulation, which can result in the formation of inclusion bodies and degradation by proteases. However, by continuous secretion of these proteins into the periplasm or culture medium, they are more diluted, therefore, protected from proteolysis by periplasmic proteases. Thus, their stability and solubility increase, which makes them fold correctly and be active biologically. [27, 28] Further, since during translocation into the periplasm N-terminal signal sequences and the methionine are removed, the recombinant protein has an authentic N-terminus that potentially avoids negative impacts on protein activity and stability. In addition, intracellular systems increase the amount of contaminating host proteins and protein loss during the cell disruption process. In contrast, extracellular systems are exempt from cell lysis, which further simplify downstream processing. [29] For these reasons, using an extracellular secretion system is an efficient way to produce recombinant proteins in *E. coli*.

Secretion of recombinant proteins in *E. coli* can be categorized into one-step or two-step secretion systems. In the one-step secretion systems, the proteins translocate through both inner and outer membranes via the membrane proteins. In these systems, the C-terminal signal sequence of the secreted proteins is not cleaved during translocation. In the two-step systems, the recombinant proteins are directed into the periplasm first (using SEC-, general secretory, or Tat-, twin-arginine translocation, pathway), followed by releasing outside of the cell (through permeation, fusion tags, and downstream processing). [28]

2.4.1. Curli secretion pathway

Curli secretion pathway is a two-step secretion system and one of the well-known and established extracellular secretion systems that is natively found in *E. coli* bacteria (Figure 2. 3). Contrary to the pathogenic amyloids involved in human degenerative diseases, curli amyloids protect bacteria from physical and chemical stresses, invasion of the host cell, and therapeutic antimicrobial agents by the formation of biofilm. [30] The curli biogenesis system is also known as the nucleation-precipitation system, which is responsible for secreting curli subunits, called CsgA, into the extracellular medium to form highly aggregative amyloid fibrils. [31-33] In *E. coli*, two separate transcribed operons (*csgBAC* and *csgDEFG*) produce seven proteins (CsgA, CsgB, CsgC, CsgD, CsgE, CsgF, and CsgG), which cooperate to form the curli amyloids. [31]

The amyloid fibers consist of the CsgA, the major structural subunit, which adopts a β-helix fold (association of parallel beta strands in a helical pattern). CsgB is the nucleating subunit for the nucleation of CsgA monomers into amyloid fibers and binding them to the cell surface. Both subunits consist of three domains, a signal peptide (SEC), an N-terminal segment ($CsgA_{N22}$ and $CsgB_{N23}$), and a C-terminal amyloid core domain. The amyloid domain consists of five pseudo-

repeats (R1-R5). The SEC peptide is a translocase machinery to transport CsgA across the internal membrane and is cleaved after secretion of CsgA into the periplasmic area. The 22 N-terminal sequence (N22) of the CsgA directs the monomers to the outer membrane through the membrane channels. [34, 35]

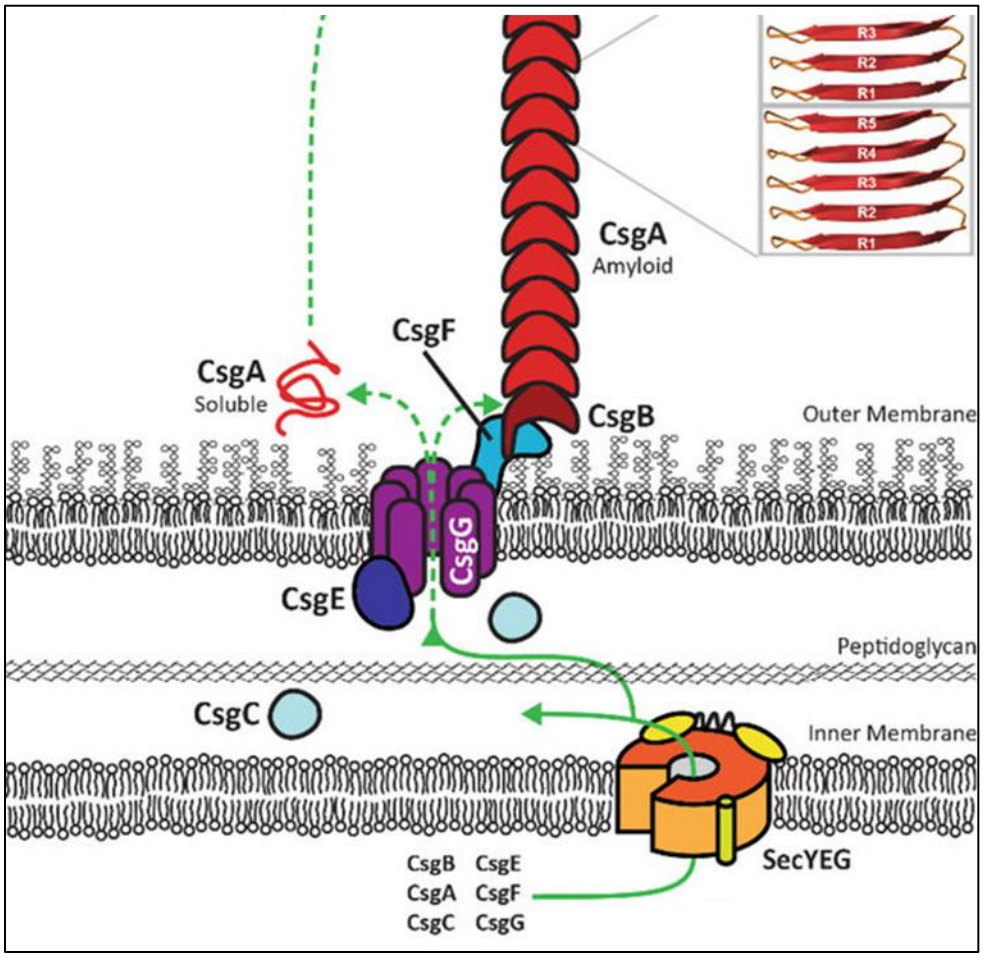

Figure 2. 3. Model for demonstration of the components curli extracellular secretion pathway, secretion of CsgA monomers, and their assembly into amyloid-like fibers. [36]

CsgG is a lipoprotein that oligomerizes into a pore-like structure (nonameric transport complex) that is required for secretion of the major subunit CsgA and the minor subunit CsgB into the extracellular milieu. CsgG cooperatively works with other periplasmic and extracellular accessory

proteins, such as CsgE and CsgF, respectively.[37, 38] To explore whether CsgG is specific to the CsgA sequence and structure the heterologous sequences have been fused to the CsgA C-terminus. It has been shown that the CsgG is a non-selective and ungated protein secretion channel and can transport the non-amyloid proteins using its diffusion-based mechanism into the extracellular medium. [38] It has been reported that the fused proteins with transverse diameters of 2.5 nm or less were able to be secreted in a CsgG-dependent manner. [37]

CsgE is a small periplasmic factor that acts as a cap for CsgG and blocks the unfolded CsgA from returning into the periplasm and by binding directly to CsgA inhibits the premature aggregation and polymerization of the monomers. [39]

CsgF is an extracellular accessory protein (exposed to the surface) that binds to the CsgG secretion pore and controls the CsgB-mediated nucleation of CsgA. It has been shown that the lack of the *csgF* gene can still result in the extracellular secretion of CsgA monomers, but the monomers will inefficiently be assembled and form aggregated curli fibers. [40]

The exact function of CsgC protein during curli biogenesis is less defined. CsgC protein with a crystal structure, has a putative oxidoreductase role, with a possible target of CsgG. It has been investigated that CsgC creates or removes disulfide bonds of CsgG transmembrane helices and can change the CgsG pore characteristics, such as radius or selectivity, therefore, possibly affecting the porosity and flux of the export complex. [41] Lacking the *csgC* gene in the mutant strains can result in the assembly of the curli but defected auto-aggregation. [41] Table 2. 4 summarizes the role of each component in the curli secretion system.

Curli fibers are very versatile and can be modified by fusing different small peptides or large proteins to its structural subunit, CsgA. For example, the genetic fusion of a pH-responsive red

fluorescent with CsgA resulted in a curli fiber-based sensor that can respond to pH changes and distinguish between alkaline and acidic solutions.[42]

Table 2. 4. The role of components in the curli secretion system.

SEC	Signal peptide, translocase machinery (periplasmic secretion).
N22	Targets CsgA to CsgG transmembrane (extracellular secretion).
CsgA	The major subunit of curli fiber.
CsgB	The minor subunit of curli fiber and the nucleator protein.
CsgG	Oligomerizes into pore-like structures and is required for secretion into the extracellular milieu.
CsgC	Not well-defined, but possibly has oxidoreductase activity.
CsgE	Directs CsgA to the CsgG secretion complex.
CsgF	Necessary for CsgB-mediated assembly of CsgA
CsgC	Possibly has oxidoreductase activity.

2.5. Purification of recombinant proteins

Using the secretion pathway results in simplifying the downstream process, by eliminating the need for cell lysis. As we discussed in section 2.4, cell rupture can affect the activity and stability of the protein of interest. The cell lysis process can be done by either reagent-based methods or physical methods. Lysing reagents such as enzymes and detergents can cause denaturation and degradation of the proteins. The physical methods such as ultrasonication, crushing and grinding, freeze-thaw, and osmotic shock can elevate the heat and shear stress and degrade the proteins. [43] Overall, by eliminating the cell lysis step, the purification process becomes simple, easy, and less costly.

Affinity-based chromatography is a prevalent technique for purifying recombinant proteins. In this technique, an affinity tag is fused to the protein of interest that selectively binds to the resin. These methods result in high-purity protein products, but they can be challenging with some disadvantages. At the large industrial scale, the cost of large volumes of resin can become excessively expensive. Protein loss due to metal ions leakage is another limitation of chromatography methods. [44]

Fusing the proteins of interest with thermally responsive proteins, such as elastin-like polypeptides (ELPs), is known as a strategy for non-chromatography purifications. ELPs are highly soluble in the water below their inverse transition temperature but undergo a sharp phase transition above this temperature, which results in their de-solvation and aggregation. [45] For instance, Mills *et al*. [44] showed that ELP-tagged proteins were precipitated selectively by increasing the temperature at a certain salt and ethanol content. [44] Another non-chromatography purification was introduced by Dorval *et al*., [46] for isolation of the curli fibers using filtration. Filtration is a common approach for isolating amyloids that relies on their resistance to denaturation in the presence of detergents, as compared to other proteins in the cell lysate. Curli fibers are extremely resistant to denaturing agents, heat, enzymes, and harsh solvents. In the latter work, extracellularly secreted curli fibers were isolated with ~80% purity by fast and easily accessible vacuum filtration procedure and through chemical and enzymatic treatments, such as treating with guanidinium chloride, sodium dodecyl sulfate, and nuclease. [46]

2.6. Proteins and bio-inspired mineralization

Biomineralization is the process of creating composite materials from living organisms for a variety of purposes, such as mechanical support, navigation, and protection against predation.

[47] Biomineralization process starts with nucleation step followed by growth that results in the formation of a new crystalline phase. The nucleation, which happens very fast and is hard to control, usually is the key step in building up the complex mineralized structure and starts with the formation of spherical molecular clusters. Stabilized nuclei, also called ‘‘delayed nucleation’’, can result in monodisperse nuclei, consequently the formation of nanocrystals with nearly monodisperse size. The growth of the nuclei can be controlled by thermodynamic and kinetic paraments. For example, the shape of inorganic crystals is normally related to the intrinsic unit cell structure and their surface energy. The surface energy of a crystal face can be lowered by the adsorption of an additive; thus, the crystallization process and the final morphologies can be modified. In addition, the kinetic crystallization control can be achieved by modifying the activation-energy barriers of nucleation, growth, and phase transformation. For instance, structured organic surfaces can lower the activation energy of nucleation of specific crystal faces and polymorphs. [48]

The *in vivo* process of bone mineralization is mostly directed by the non-collagenous proteins (NCPs), including osteonectin and osteopontin, osteocalcin, phosphophoryn, and bone sialoprotein. NCPs are rich in aspartic and glutamic acid residues, therefore, have a high content of carboxylate groups, which can bind calcium ions present in the body fluids. [49] Therefore, inspired by this biologically controlled mineral formation, carboxylate-rich proteins and peptides have been used as effective biotemplates to fabricate organic-inorganic complex composites.

Special arrangement of different proteins, depending on their three-dimensional (3D) structures or unique sequence-specific self-assembly properties, can direct the ‘‘bottom-up’’ syntheses of inorganic materials. [50] There are several advantages to the protein-mediated synthesis process, such as (1) milder reaction conditions (usually aqueous solution and reaction temperature at 37°C)

compared with the traditional material-processing techniques, which rely on inorganic solvents, complicated ligands, and strong reducing agents, (2) controlling the size, shape, and physicochemical properties of inorganic particles based on the structure or amino acid sequence of proteins, (3) the protein-inorganic particles composite is further modifiable through the chemical groups and binding sites in proteins. [51]

Bovine serum albumin, [52] ferritin, [53] trypsin, [54] lysozyme, [55], and collagen are among the proteins that have been used for the synthesis of different inorganic particles such as iron oxide nanoparticles, gold nanoparticles, calcium carbonate, hydroxyapatite, and silica. In general, the use of proteins can help with the interaction of ions andtheir nucleation and growth, and providing a scaffold for mechanical support.[56]

More specifically, type I collagen is known as the universal template for mineral deposition, such as hydroxyapatite, [57] calcium carbonate, [58] silica, [59, 60] metal oxides [61], and metal nanoparticles. [62, 63] For example, the special arrangement of collagen fibrils makes them a proper template for nucleation and growth of hydroxyapatite crystals. [64] The fibrils assemble in a parallel arrangement to form a repeated 40 nm gap, called the “hole zone” with the net positive charge, [65] which is known to be an important site for the nucleation of hydroxyapatite crystals (Figure 2. 4). [64] Besides, the collagen scaffold drives the adsorption of Ca^{2+} ions by ionic bonds and PO_4^{3-} ions by hydrogen bonds which initiate the nucleation of hydroxyapatite crystals along the fibrils.

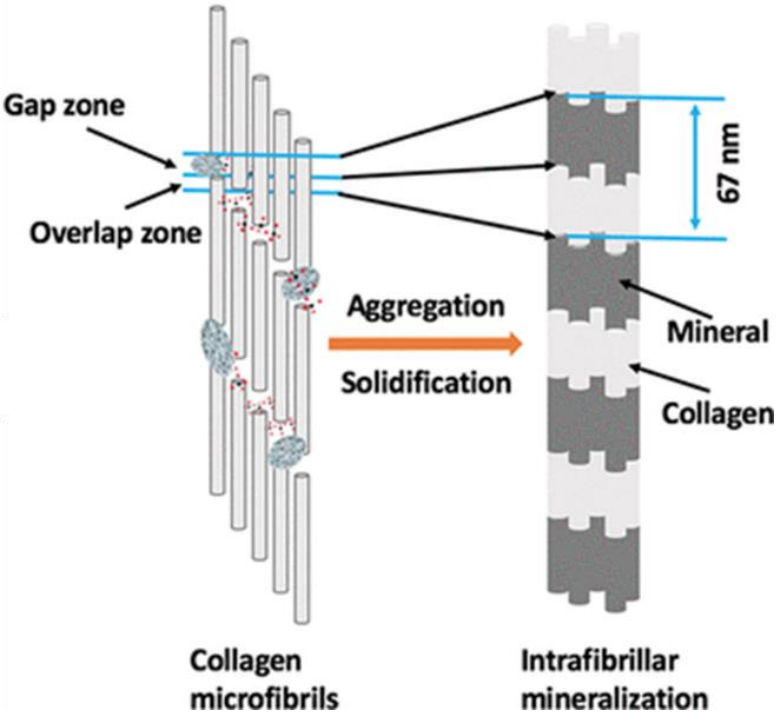

Figure 2. 4. Schematic illustration of the intrafibrillar mineralization. [57]

In addition, collagen have been used for the green synthesis of metal nanoparticles, such as a silver nanoparticle, for a range of applications, from wound dressings [66] and to cardiac patches. [62] The high content of carboxylate groups in the collagen electrostatically interacts with silver ions and can enhance the colloidal stability of nanoparticles during the nucleation and growth stages and prevent the agglomeration of the particles. [49, 67] In addition, the nanoparticles can be distributed uniformly along the collagen fibers, which potentially can be useful to design electroconductive collagen nanofibers. [68]

Collagen-silica composites also have been used for bone tissue scaffolds [69] and wound healing. [59] The surface silanol groups in silica can enhance the bioactivity and osteoconductivity of silica by promoting the formation of biologically active bone-like apatite and calcium phosphate deposition.

The surface silanol groups can interact with carboxylate groups in collagen by hydrogen binding and make an interconnected network of collagen-silica through polycondensation.

Recombinant collagen protein can be a safe material source for biomineralization. By modifying the sequences and structures of the recombinant proteins, they can modulate the nucleation and growth of inorganic particles in biomineralization processes. The complex shape, hierarchical organization, and well-defined morphology and size of the recombinant proteins make them suitable templates for bio-inspired mineralization processes.

As we mentioned before, bacterial collagen contains a high content of proline and charged amino acids that support the stability of bacterial collagen. The charged residues such as aspartic acid (Asp, D), glutamic acid (Glu, E), lysine (Lys, K), and arginine (Arg, R) can participate in electrostatic interactions and support interchain hydrogen bonding. The pool of charged amino acids in the bacterial collagen can play the role of an initiator for the interaction of the collagen and inorganic precursors to direct the synthesis of the particles.

Curli fibers have also been used as a template to nucleate the gold nanoparticles and modulate their growth and characteristics. For example, various gold and silver-binding peptides have been fused to the C-terminus of CsgA to achieve tunable electrical conductivity. [70, 71]

Chapter 3. Curli-mediated self-assembly of a fibrous protein scaffold for hydroxyapatite mineralization

3.1. Rationale for Chapter 3

Nanostructures formed by self-assembled peptides have been increasingly exploited as functional materials for applications as biomaterials. However, it is often challenging to assemble free short peptides into functional supramolecular structures, since many peptides of interest cannot self-assemble. There are major challenges associated with the physical or chemical tethering of the free peptides onto polymeric scaffolds or substrates, such as weak bonding, harsh and destructive reagents, changes in peptides positioning after assembly, and poor control over unwanted side reactions. This chapter presents a method for overcoming these challenges utilizing the curli system. In addition to establishing the curli system as a means to self-assemble free peptides, we demonstrated that truncated CsgA proteins can form nanofibers with a morphology similar to native curli fibers and can form macroscopic functional hydrogel material.

The final engineered proteins serve as a template for hydroxyapatite mineralization and open up broader applications for curli proteins in biomaterials fields and bone tissue engineering.

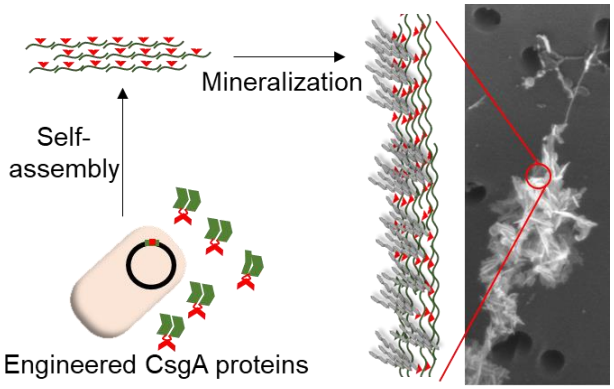

Chapter 3 is based on a manuscript entitled “Curli-mediated self-assembly of a fibrous protein scaffold for hydroxyapatite mineralization”, published in *ACS Synth. Biol.* (2020, 9, 12, 3334–3343) which was co-authored by: Masoud Aminzare, Xiaodan Zhu, Elizabeth DeBenedictis, Oliver Xie, Sinan Keten, and Noémie-Manuelle Dorval Courchesne.

3.2. Abstract

Nanostructures formed by self-assembled peptides have been increasingly exploited as functional materials for a wide variety of applications, from biotechnology to energy. However, it is sometimes challenging to assemble free short peptides into functional supramolecular structures, since not all peptides have the ability to self-assemble. Here, we report a self-assembly mechanism for short functional peptides that we derived from a class of fiber-forming amyloid proteins called curli. CsgA, the major subunit of curli fibers, is a self-assembling β-helical subunit composed of five pseudo-repeats (R1-R5). We first deleted the internal repeats (R2, R3, R4), known to be less essential for the aggregation of CsgA monomers into fibers, forming a truncated CsgA variant (R1/R5). As a proof-of-concept to introduce functionality in the fibers, we then genetically substituted the internal repeats by a hydroxyapatite (HAP)-binding peptide, resulting in a R1/HAP/R5 construct. Our method thus utilizes the R1/R5-driven self-assembly mechanism to assemble the HAP-binding peptide and form hydrogel-like materials in macroscopic quantities suitable for biomineralization. We confirmed the expression and fibrillar morphology of the truncated and HAP-containing curli-like amyloid fibers. X-ray diffraction and TEM showed the functionality of the HAP-binding peptide for mineralization and formation of nanocrystalline HAP. Overall, we show that fusion to the R1 and R5 repeats of CsgA enables the self-assembly of functional peptides into micron long fibers. Further, the mineral-templating ability that the

R1/HAP/R5 fibers possesses opens up broader applications for curli proteins in the tissue engineering and biomaterials fields.

Keywords: self-assembling proteins, curli fibers, hydroxyapatite-binding peptide, supramolecular protein materials, biomaterials, biomineralization.

3.3. Introduction

Curli fibers are a group of functional amyloids assembled by many Gram-negative bacteria, such as *E. coli*, as part of their extracellular matrix.[72, 73] Curli fibers are composed of repeated self-assembling subunits, called CsgA, which consist of a β-helix structure composed of five pseudo-repeats (R1-R5). Each repeat comprises two β-strands on opposite sides of the protein, which adopts an overall β-helical tertiary structure.[72, 73] Due to this characteristic β-helical structure and their high propensity to aggregate after extracellular secretion, self-assembled CsgA proteins form mechanically and chemically resistant amyloid fibers. Furthermore, these fibers are extremely versatile for customization with functional domains – the protein core of CsgA can be directly mutated,[74, 75] and the protein can be genetically fused with small peptides or large protein domains for a wide variety of applications.[46, 70, 76, 77]

Although the five repeats of CsgA have very similar sequences, it has been found that only the external N- and C-terminal repeats are crucial for CsgA self-assembly and seeding.[73, 78] Wang *et al*, studied the polymerization rate of different repeat-deletion CsgA mutants using Thioflavin T fluorescence.[78] They observed a defective polymerization for R5-deleted CsgA with a long lag phase (~ 25 h) compared with other mutations. In contrast, the polymerization of CsgA mutants with removed R2, R3, or R4 was not impaired, but showed a longer lag phase (~ 2 h) compared with WT CsgA (~ 1 h). Besides, studying the polymerization of chemically synthesized monomers

showed no detectable lag phase for R5, a shorter lag phase for R1 compared with R3 (2 times shorter), and no polymerization for R2 and R4 after removal of the denaturant. These observations indicate the greatest contribution of R1 and R5 to protein aggregation compared with the internal repeats. Collectively, these results demonstrated that R1 and R5, the N- and C- terminal external repeats of CsgA, play an important role in the self-polymerization of CsgA, while R2, R3, and R4 are not essential for amyloid formation.

These observations raise the questions of whether a synthetic truncated CsgA-like protein (with deleted internal repeats) could retain the ability to assemble into amyloid fibers, and whether this new CsgA-like self-assembling scaffold (consisting of R1 and R5) could be used as a minimum required structure to drive the assembly of protein materials. The unique ability of a truncated CsgA to self-assemble into fibers, and to aggregate into supramolecular materials and hydrogels [76, 79, 80] could be employed to mediate the assembly of functional peptides or proteins that do not have the ability to self-assemble by themselves. Motivated by this hypothesis, here we report the deletion of the R2, R3, and R4 pseudo-repeats of CsgA and the study of the assembly of the new truncated CsgA (R1/R5). We further replaced the internal repeats by a functional peptide to utilize the R1/R5-driven self-assembly mechanism to assemble non-amyloidogenic functional protein domains (Figure 1A). We chose to replace the internal repeats of CsgA with a functional peptide - rather than fusing the peptide to the N- or C-terminus of the truncated CsgA - in order to minimize steric hindrance of the fused domain. In fact, it has been reported that the fusion of protein domains at N- or C-terminus of CsgA can affect assembly rate, morphology, and stiffness of the resultant fibrils by interfering with monomer interactions.[81] Substituting the internal repeats with a peptide also allows for introducing new functionalities in curli-like fibers. In addition, truncating CsgA could provide the opportunity of fusing large proteins that may otherwise be challenging to secret

extracellularly through the native CsgA secretion pathway. As a proof of concept, we used a short 12-amino acid peptide that has a specific binding affinity to single-crystal hydroxyapatite (HAP), and that can template the nucleation and growth of crystalline HAP.[82] HAP is the main component of bone, acting as a template for the mineral phase deposition and stimulating new bone formation.[83] The HAP-binding peptide sequence resembles the tripeptide repeat (Gly-Pro-Hyp) of type I collagen, a major component of bone extracellular matrix. The main factor promoting specific interactions between the binding peptide and single-crystal HAP is the unique spatial arrangement of the residues in the HAP-binding site. Cooperative interactions of hydrogen bonding, van der Waals, and Coulombic types between the peptide and the HAP surface are other key contributing factors to increase the HAP binding.[82] Recently, hydrogels loaded with HAP were reported to show high osteointegration because of the spontaneous formation of a gel/bone hybrid layer at the interface of bone and scaffold that could effectively induce the osteogenic differentiation of human mesenchymal stem cells.[83-85] Among the methods of preparing mineralized scaffolds, soaking the scaffold in simulated body fluid (SBF) is the most commonly used surface mineralization technique. [86] However, it is difficult for the solution to reach the interior of the nanofibrous block, thus resulting in surface mineralization with randomly oriented clusters of the HAP crystals, as opposed to a bulk mineralization.[87]

Self-assembled peptide nanostructures have been increasingly exploited as functional materials for applications in biomedicine and energy. [88-91] To assist with the assembly of the free peptides, physical or chemical tethering within the non-natural organic compounds, such as hydrophobic long chain alkyl or aromatic molecules, has been employed. [88] For instance, HAP-binding peptides have been chemically conjugated with hydrophobic alkyl chains to fabricate nanofiber-forming amphiphilic peptides that can assemble into hierarchically organized functional biomaterials.[92]

Due to complexities associated with chemical conjugation, such as harsh and destructive reagents, weak bonding, change in peptides positioning after assembly, and low control over unwanted side reactions, genetic modifications open up new possibilities to engineer self-assembly of functional free peptides. Hence, our use of the curli self-assembly system to form fibers containing the HAP-binding peptide provides a means for genetically programming the self-assembly process without the need for chemical post-modifications. The self-assembled nanofibrous materials proposed here are suggestive to develop biomimetic materials, because they are similar to extracellular matrices as they display the high densities of biochemical cues and provide physical cues due to the unique geometry of the nanofibrous structures. [92] Fusing the HAP-binding peptide with each R1/R5 monomers, will further increase the density of the HAP nucleation sites and could facilitate bulk mineralization of the biomaterials.

Our work here verifies the hypothesis that a truncated CsgA can still self-assemble into curli-like fibers, and that the assembly of the HAP-binding peptide can be driven by the R1 and R5 repeats of CsgA. We characterized the secondary structure of these genetically engineered proteins and the aggregation and assembly behavior of the fibers. We also confirmed the functionality of the HAP-binding site incorporated into the protein fibers by comparing the HAP mineralization of the unmodified, truncated, and HAP-containing curli fibers as templates. This work opens up a new direction to use the self-assembling behavior of the curli system to mediate the formation of protein fibers with other functional peptides.

3.4. Materials and methods

Cell strains, plasmids, and curli expression. The pET21d-*csgACEFG* plasmid and the curli operon deletion mutant strain of *E. coli*, PQN4,[46] were gifts from the Joshi Lab (Harvard

University, Boston, MA). We used this pET21d plasmid, with the curli operon (without the CsgB nucleator protein) under the control of the T7 promoter, as template vector to synthesize different genetic variants of the CsgA protein. To truncate wild-type CsgA (WT), whole CsgA fragment was replaced with a modified CsgA (R1/R5) fragment consisting only R1 and R5 (Life technologies) using Gibson assembly (New England Biolabs). The pET21d-*csgACEFG* plasmid was linearized using forward and reverse primers starting at the C-terminal end of the CsgA and at the end of N22, respectively. The double-stranded DNA fragment of encoding R1/R5 was inserted in the linearized plasmid. To remove the internal repeats and replace with the HAP-binding peptide, the pET21d-*csgACEFG* plasmid was linearized using forward and reverse primers starting at the beginning of R5 and at the end of R1, respectively. The oligonucleotide (108 bp) encoding HAP-binding peptide, with two flexible glycine-serine linkers (L12) at the C- and N-terminals of HAP, was synthesized by overlap elongation PCR and inserted in between R1 and R5 using Gibson assembly (R1/HAP/R5). Based on the size of the fusion domain used here (HAP binding site: 12 residues), we selected (GSG)4 (L12) as a linker with a reasonable length and flexibility to guarantee the availability of the binding peptide. A six-histidine tag (HisTag) was added to the C-terminus of all the WT and modified CsgA monomers to allow for immunodetection. A pET21d plasmid containing the *malE* gene was used to express maltose-binding proteins (MBP) as a negative control for amyloid formation. Sequences of the all the genes and primers are listed in supporting information (Table S3. 1 and Figure S3. 1).

To express the proteins, the transformed PQN4 cells were streaked onto lysogeny broth (LB) agar plates containing 100 μg/mL carbenicillin and 0.5% (m/v) glucose (for catabolite repression of T7RNAP). Colonies were picked from the plates, and 5 mL cultures were inoculated (in LB containing and 100 μg/mL carbenicillin and 2% (m/v) glucose). Cultures were grown overnight at

37 °C. The overnight cultures were diluted 100-fold in fresh LB medium with 100 μg/mL carbenicillin and cultured at 37 °C overnight. The expression was stopped at an optical density at 600 nm of ~ 2.7.

Isolation of curli fibers using vacuum filtration. After the protein expression step, isolation of the curli-like proteins was conducted based on an established protocol.[46] Briefly, before the filtration, the cultures were incubated with guanidinium chloride (GdmCl, final concentration of 0.8 M) for 20 min at 4 °C. 50 mL of the GdmCl-containing cultures were then vacuum-filtered onto 47 mm polycarbonate filter membranes with 10 μm pores (Thermo Fisher). The filtered biomass was subjected to three steps of incubation including; 1) 5 mL of 8 M GdmCl for 5 min, 2) 5 mL of an aqueous solution of Benzonase nuclease (Sigma-Aldrich, 1.5 U/ mL) for 10 min, and 3) 5 mL of 5% (m/v) sodium dodecyl sulfate (SDS) in water for 5 min. Each step was followed by 3 rinses with 5 mL of DI water. Semi-purified curli-like proteins were collected from the filter membrane by gently scraping the filter with a flat spatula. They were then lyophilized, and stored at 4 °C. However, filtration of the R1/R5 protein demanded a slight modification to the original protocol. To provide milder filtration conditions for R1/R5 proteins, which aggregated less than WT and R1/HAP/R5 proteins, the cultures were filtered without performing the 20-min pre-incubation step with GdmCl, and with a shorter incubation time (3 min) for all the reagents during the filtration process.

Assessment of Curli Expression. The first step to confirm the curli nanofiber expression was performed using the binding affinity of Congo Red dye to amyloid proteins.[46] 1-mL samples were taken directly from the bacteria cultures and centrifuged. The collected pellet was resuspended in phosphate buffer and incubated with Congo Red (final concentration of 0.00015% (m/v)) for 10 min. After a centrifugation step, absorbance of the supernatant was measured at 490 nm to quantify

the amount of Congo Red that did not bind to the cells. After vacuum filtration, the deposition of curli nanofibers on the filter membranes was also assessed by incubating the filters in 5 mL of 0.015% (m/v) of Congo Red dye solution for 10 min, followed by vacuum filtration of the liquid and 3 rinses with 5 mL of DI water.

SDS-PAGE. The expression of the modified curli proteins was assessed by confirming their molecular weights using SDS-PAGE. 0.5 mg of curli proteins were disassembled by dissolving them in a 1:1 (v/v) Hexafluoroisopropanol:Trifluoroacetic acid (HFIP:TFA) (Oakwood Chemical) mixture and sonication for 1 h. After evaporating the solvent, the samples were resuspended in DI water and loading buffer. After electrophoresis at 200 V for 30 min, the gel was stained using Coomassie blue for 30 min, destained for 1 h, and imaged.

Electron Microscopy of bacterial cultures. Scanning electron microscopy (SEM) samples were prepared by depositing the samples, taken directly from bacterial culture, on 0.2 μm polycarbonate filter membranes (Whatman® Nuclepore from Millipore Sigma). The membranes were washed with 0.1 M sodium cacodylate buffer (Electron Microscopy Sciences), fixed with 2% (v/v) glutaraldehyde (Bio Basic) and 2% (v/v) paraformaldehyde (Electron Microscopy Sciences) for 2 h at room temperature, and solvent-exchanged sequentially in 0%, 25%, 50%, 75%, and 100% (v/v) ethanol (for 15 min in each solvent). The membranes were dried in a critical point dryer (CPD) and sputtered until they were coated with a 5 nm layer of Pt. Imaging was performed using a FEI Quanta 450 ESEM at 5 kV.

Fibrillation analysis of the modified CsgA monomers. Atomic force microscopy (AFM) was used to study the nanostructure of the disassembled curli-like nanofibers and their growth behavior during reassembly. The lyophilized proteins (0.5 mg/ml) were re-solubilized in 1 mL HFIP:TFA (1:1) and sonicated for 15 min. The stock solutions were diluted three times in DI water. After

different incubation times, 4 μL of the protein solutions was added onto freshly cleaved mica sheets and allowed to dry overnight. The samples were imaged using a Veeco Multimode Nanoscope III AFM with a 240AC-NA micro cantilever tip (Opus).

Circular Dichroism (CD) spectroscopy. To evaluate the secondary structure of the engineered proteins, they were assayed in a Chirascan spectrophotometer (Applied Photophysics) from 180 to 260 nm in a quartz cell with a 1-mm path length at 20 °C, using 1 nm step size and a bandwidth of 1 nm. The protein solutions were prepared by immersing 0.5 mg of the proteins in 1 mL DI water overnight, followed by vigorous vortexing. Since curli fibers do not fully dissolve in water, the true concentrations of dissolved proteins in the CD cuvettes were calculated using the absorbance (A_{280}) of the solutions and their extinction coefficients predicted by Benchling (The Life Sciences R&D Cloud) at 280 nm. The molar ellipticity values were normalized by the concentration for each protein. All spectra were baseline corrected with respect to DI water.

Molecular dynamics modeling of the structure of truncated CsgA. To construct the mutant R1/R5 model, the sequence of the R1 and R5 repeats in CsgA was mapped onto R1 and R2 repeat structures from the predicted model introduced in reference 19.[93] The mapping was completed using MODELLER [94] and produced a monomer of 64 residues containing two β-strand repeats and a flexible 22-residue N-terminus. Next, the R1/R5 monomers were stacked into a multimer by aligning the interface between R1 of one monomer and R5 of another monomer to the same R1-R5 interface of the CsgA dimers created in reference 21.[95] This procedure was repeated to build multimer structures made up of 6 stacked monomers. A similar R1/HAP/R5 mutant model was also created by using MODELLER to insert the HAP sequence between R1 and R5 and multimers were built using the same steps as above.

Both multimer structures first underwent energy minimization for 12,000 steps using the conjugate gradient method and equilibration for 1.2 ns with all backbone atoms fixed excluding the 22-residue N-terminus and HAP insertion. Next, both structures underwent equilibration for an additional 5 ns with no atoms fixed. Simulations were conducted using the Generalized Born Implicit Solvent as implemented in NAMD.[96] The alpha cutoff used was 15 Å and the ion concentration 0.05 molar, with solvent accessible surface area (SASA) calculations on. Simulations were run under the NVT ensemble with at 1 fs timestep and temperature of 300K. The latest CHARMM 36 parameter set is used.[97-99]

Mineralization of HAP crystals onto curli-like fibers and their characterization. To mineralize the proteins, 0.5 mg of the lyophilized proteins was dissolved in the mixture of the 100 µL of the 100 mM $CaCl_2$ and 100 µL of the 50 mM Na_2HPO_4 solution and incubated overnight at 37 °C. To remove excess salts, the samples were centrifuged and washed thorough 0.2 µm filter membranes. To investigate the morphology of the mineralized proteins using SEM, 50 µL of the mineralized protein solution was deposited on 0.2 µm polycarbonate filter membrane and rinsed with DI water. The samples were fixed using the protocol described above for bacterial cultures, dried by CPD, and sputtered coated by a 5 nm layer of Carbon. In addition, mineralized samples were lyophilized and analyzed to confirm the formation of the HAP crystals using X-ray diffraction (XRD; Bruker D8 Discovery X-Ray Diffractometer (VANTEC Detector, Cu-Ka (alpha)).

Furthermore, the HAP nucleation ability of the modified proteins was studied by directly mineralizing the proteins on a TEM grid to minimize the effects of sample preparation, adapting an approach previously reported. 7 µL of protein solution (0.5 mg/L) was applied over a carbon coated TEM grid (200 mesh) for 2 min. The protein loaded TEM grid was then treated with 10 µL of 5 mM Na_2HPO_4 on one side and 10 µL of 10 mM $CaCl_2$ on the other side. After 2 h, the TEM

grid was washed three times by dipping the grid in DI water and dried under ambient conditions before TEM analysis. A control sample without protein was also prepared and underwent the same mineralization treatment. Transmission electron microscopy (TEM; FEI Tecnai G2 F20 200 kV Cryo-STEM) was used to observe the formation of the nucleated HAP minerals on the protein templates.

3.5. Results and discussion

Expression and morphological characterization of curli-like protein fibers

To confirm the expression of engineered proteins and their assembly into curli-like fibers, we first used the Congo Red amyloid-binding dye and studied the expression of amyloid fibers quantitatively and qualitatively (Figure 3. 1B). Cells expressing the modified CsgA proteins showed binding to Congo Red comparable with cells expressing WT curli fibers (positive control), and significantly higher compared with cells expressing maltose-binding proteins (MBP) (negative control). R1/HAP/R5 and R1/R5 showed 17% more and 15% less binding to Congo Red compared with the WT curli fibers. The greater dye binding capacity of R1/HAP/R5 could be due to non-specific binding of Congo Red to HAP-binding peptide or linker, and the lower dye binding by R1/R5 could be a result of the weaker tendency of R1/R5 proteins to aggregate to form bundles (refer to the upcoming discussion on structure self-assembly of R1/R5), thus entrapping fewer dye molecules. Although the expression of the R1/R5 was lower than WT, the yield of the isolated protein was still sufficient to support the fabrication process of protein hydrogels, thin films and mineralized hydrogels (Figure S3. 2). Second, we also showed the deposition of assembled curli-like fibers on filter membranes during the filtration process. All filter membranes that served for filtering WT, truncated or HAP-containing curli-like fibers showed a red color after incubation

with Congo Red, indicating the presence of amyloid fibers retained on the membranes. These results indicate that the modified CsgA proteins can assemble into curli-like amyloid fibers, despite the deletion of internal R2, R3, and R4 repeats.

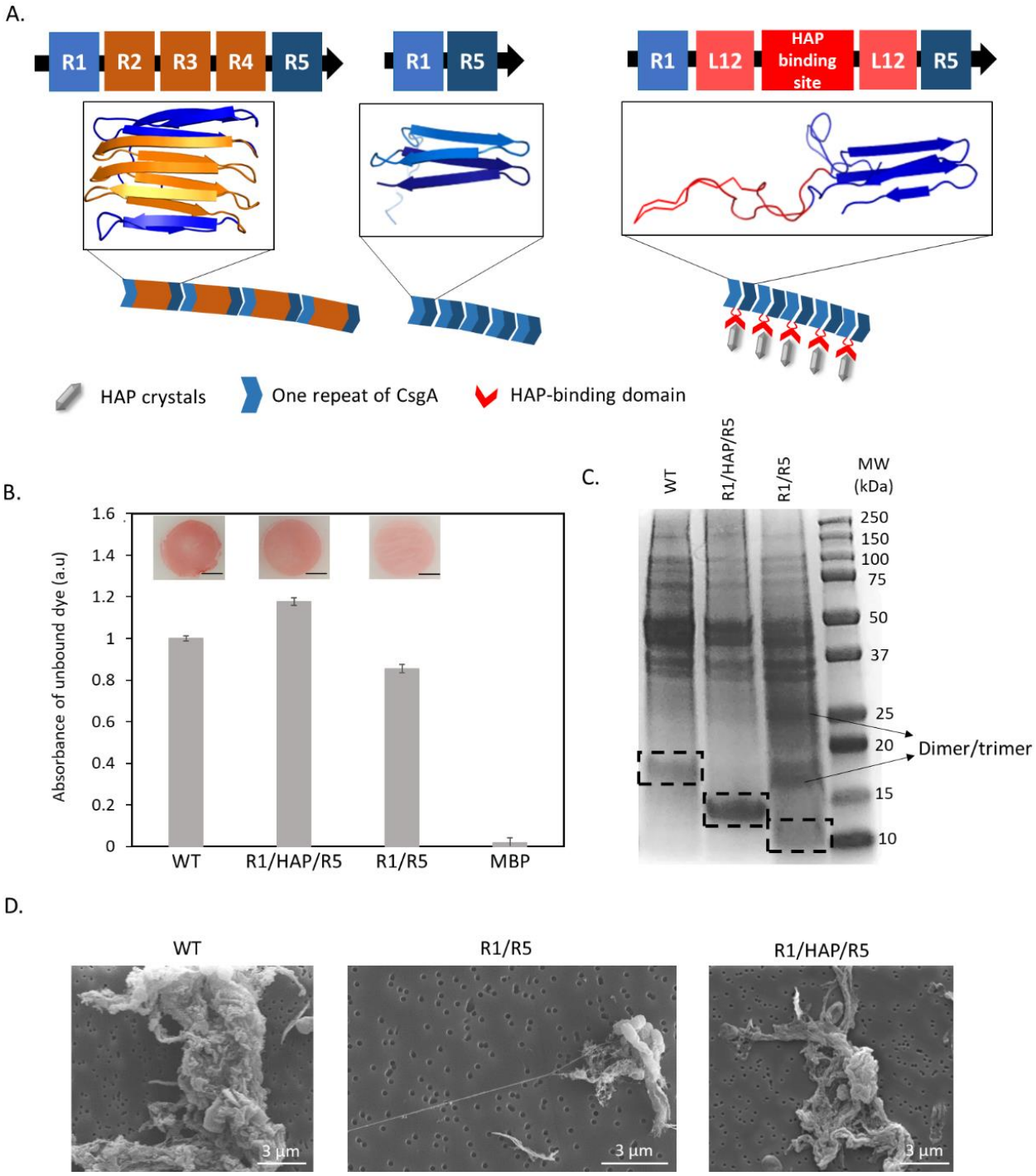

Figure 3. 1. Expression of modified curli-like protein fibers assembled via R1-R5 interactions. (A) Proposed constructs for curli-like proteins (top) and their expected structures and assembly into fibers (bottom). (B) Qualitative and quantitative assessment of curli-like proteins expression using Congo Red staining method by staining the deposited proteins on filter membranes after vacuum filtration (top pictures), and by measuring the absorbance of unbound dye to protein expressing culture (absorbance values). Absorbance values were normalized by the cell density (A 490/ A 600) and relative to WT. Scale bars = 2 mm. (C) SDS-PAGE analysis of the semi-purified proteins showing bands of the expected molecular weight for wild type and modified CsgA proteins (black dash boxes), and bands for the dimer and trimer of R1/R5 (black arrows), (D) SEM images of bacterial cultures expressing curli-like proteins, showing bacterial cells and fibrous protein aggregates. Scale bars = 3 μm.

To further characterize the modified CsgA proteins, we isolated the proteins using vacuum filtration and obtained hydrogel proteins for all mutants (Figure S3. 2). The yield of semi-purified curli fibers obtained via vacuum filtration has been determined previously to be around 50 mg per liter of culture, for filtration on 47 mm diameter filter membranes, with a purity as high as 80%. [46] We collected the products and confirmed the expression of each modified protein using SDS-PAGE to assess the presence of proteins with the predicted molecular weight (Figure 3. 1C). We observed bands at molecular weights close to those expected for all three CsgA-like proteins (WT: 14.7 kDa, R1/HAP/R5: 10.9 kDa, R1/R5: 7.8 kDa), confirming the expression of the proteins, the deletion of the internal repeats for R1/R5, and their substitution with the HAP construct for R1/HAP/R5. In the case of R1/R5, additional bands were visible around 17 kDa, and around 25 kDa. These bands appeared to correspond to dimers and trimers of R1/R5 (close to the expected MW of dimers, ~16 kDa, and trimers, ~24 kDa), respectively. The fact that these bands are clearly observed in this lane only could indicate that short oligomers of R1/R5 proteins are more resistant to disassembly by incubation in a mixture of HFIP and TFA compared with larger curli subunits (CsgA or R1/HAP/R5), or that they can re-assemble faster when resuspended in an aqueous buffer.

Additional bands of higher molecular weights observed in all three lanes correspond to others *E. coli* proteins (impurities) or CsgA oligomers.

We then analyzed the morphology and aggregation behavior of curli-like fibers after extracellular secretion using SEM (Figure 3. 1D). SEM images of bacterial cultures (Figure 1D) show that all proteins exhibit fibrous structures that tend to aggregate together to form micron-sized bundles. The modified CsgA monomers thus retained the ability to self-assemble into fibrils, in a very similar fashion compared with WT CsgA. However, R1/R5-based fibers formed slightly less aggregated and longer fibers. This weaker tendency of R1/R5 monomers to aggregate laterally and form large structures was consistent with our observation that milder conditions and shorter incubation times were necessary during vacuum filtration to retain the proteins on the filter membrane and obtain a high fiber isolation yield. Overall, the SEM images support the results obtained from the Congo Red binding assay and the fact that the modified proteins can assemble into fibrous structures after secretion into the extracellular medium. Although we deleted three internal repeats from the CsgA monomer, R1 and R5 still drive the assembly and interactions between the truncated monomers, thus serving as a template for assembly of the HAP-binding peptide. This short peptide does not spontaneously self-assemble into higher order structures, but R1 and R5 enabled its assembly into supramolecular fiber-like structures. Besides, the modified proteins exhibited a fibrillar extracellular matrix-like structure with a porous hydrogel microarchitecture that has proven to be important for potential applications, such as bone tissue engineering, that involves in cell integration.[100]

Next, we decided to further probe the differences in fiber length and aggregation of the modified proteins by analyzing the morphology and re-assembly kinetics of disassembled fibers using atomic force microscopy (AFM) (Figure 3. 2). To study the effect of time on the fibrillation of the

monomers, we allowed disassembled monomer solutions to re-assemble in DI water for 20 s, 20 min, and 3 h (enough time for WT CsgA monomers to fibrillate into an extended network of fibrils), and cast the mixture onto mica for AFM imaging. Immediately after mixing with water, CsgA and CsgA-like monomers began forming short filaments. After 3 h, WT monomers still appeared as relatively short fibrils, with a maximum length of around 200 nm. The R1/HAP/R5 monomers polymerized into slightly longer fibers, ranging between 200 and 500 nm in length. In contrast, R1/R5 monomers showed a faster growth and fibrillation even after a short incubation time. After 20 min, we observed fibers of over 2 μm in length. The formation of truncated CsgA fibrils therefore supports the hypothesis that removing the internal repeats of CsgA does not compromise self-assembly, and that instead it promotes the formation of longer fibers. Indeed, as previously reported,[73, 78] R1 and R5 are the most aggregation prone repeats of CsgA and can drive the assembly of amyloid fibers. These observations combined with the rapid di/trimerization of the R1/R5 monomers observed by SDS-PAGE further illustrated the fast re-assembly of truncated CsgA proteins into fibers.

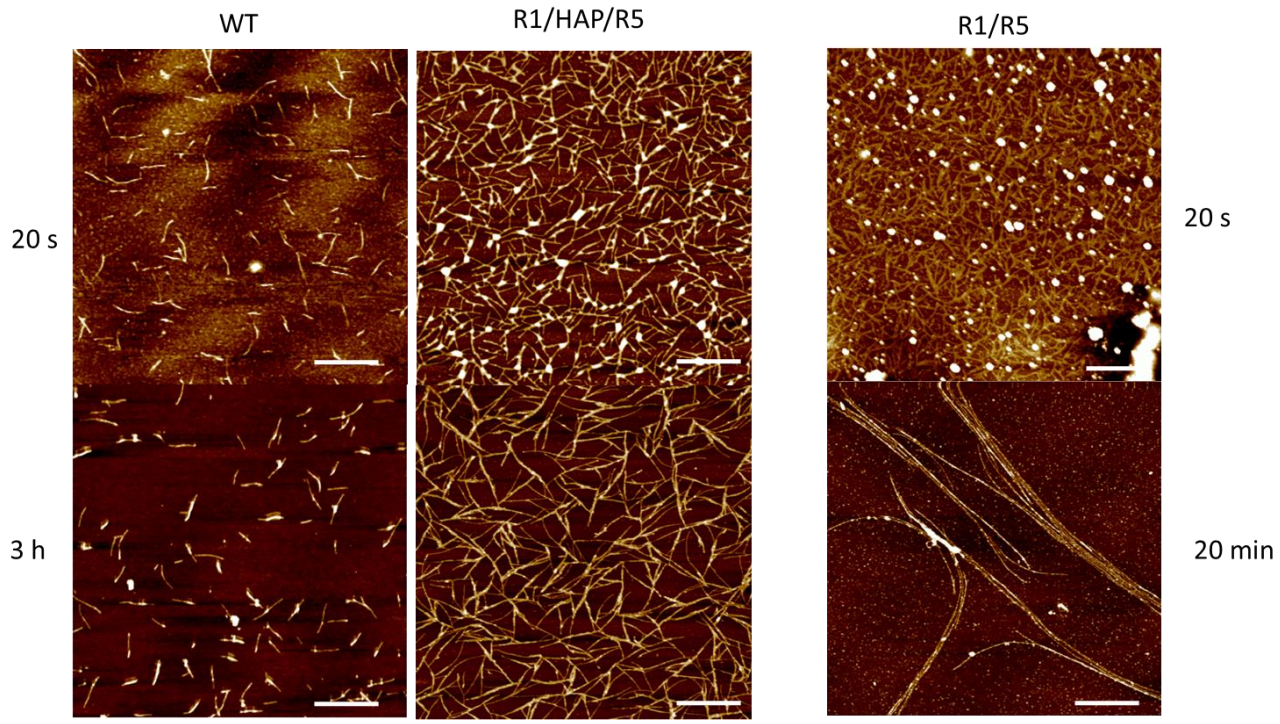

Figure 3. 2. AFM micrographs of curli-like fibers after re-assembling with different growth times in water. Significantly long fibers formed after re-assembly of the R1/R5 within 20 min. Scale bar is 500 nm.

Structural characterization and modelling of modified CsgA proteins

To investigate the folding of individual curli-like proteins and their oligomers, we studied their secondary, tertiary and quaternary structures using experimental and modelling techniques. First, to find out whether the mutated proteins folded into the characteristic secondary structure of the CsgA after modification, we studied their structure using circular dichroism (CD) (Figure 3. 3A). We observed a characteristic minimum in the range of 215-220 nm and maximum in the range of 188-191 nm exhibiting strong β-sheet signatures for all the modified proteins. The β-helical fold of CsgA proteins is supported by the extensive hydrogen bond network between the amino acids on the adjacent strands .[101, 102] The intensity of the characteristic peak around 215 nm is slightly lower for R1/HAP/R5 than for WT and R1/R5, which is likely due to the incorporation of the HAP-

binding peptide in the truncated CsgA monomer. The random coil structure of the HAP-binding peptide and flexible linkers could lower the intensity of the β-sheet signature peaks.[82] Besides, the HAP-binding peptide and the flexible linkers could also disrupt some of the inter-strand hydrogen bonds between R1 and R5, and therefore the overall stability of the protein. Nevertheless, the interactions between the side chains, such as polar interactions and hydrogen bonding, are still abundant to support the formation of the β-sheet.

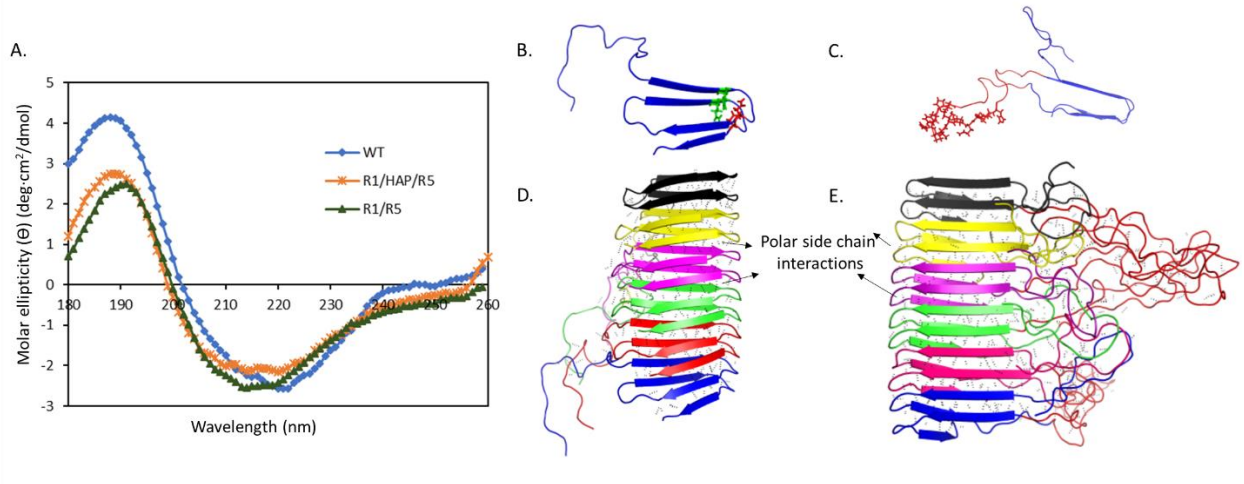

Figure 3. 3. Figure 1. Structural characterization and modelling of curli-like proteins. (A) CD spectrum of the modified proteins showing characteristic peaks indicating strong β-sheet signatures for all proteins. (B through E) Molecular dynamic models of the (B) R1/R5 monomer, mapped onto R1/R2 of the wild type CsgA monomer, showing aligned Gln7 (green) and Asn12 (red), (C) R1/HAP/R5 monomer (top view) with fused flexible linker and HAP-binding peptide, (D) R1/R5 6-mer and (E) R1/HAP/R5 6-mer minimized and equilibrated in implicit solvent in NAMD.

To investigate the tertiary and quaternary structures of truncated CsgA subunits, we developed a monomer model with the R2-R4 repeats removed and stacked the truncated monomers to build oligomers (Figure 3. 3B, D). We also constructed a variant with the HAP protein inserted between repeats R1 and R5 (Figure 3. 3C, E). The R1 and R5 β-strand repeats are aligned as in Chapman's proposed β-helical model of CsgA,[72] only with the middle R2-R4 repeats missing. In these

multimers, β-sheets still form across adjacent monomers and conserved polar residues inside the amyloid core (Ser, Gln, Asn) remain aligned, including preservation of the four residues critical for self-assembly in WT CsgA (Q29, N34, Q119, and N124).[103]

The β-sheet secondary structure is also maintained with the addition of the HAP protein between the R1 and R5 repeats. The HAP protein is modeled as unstructured and positioned to the side of the amyloid core, connected by flexible linkers. While β-sheets across the R1/R5 strands still form, it is possible that the incorporated HAP proteins may interact with the amyloid core, disrupting β-strand hydrogen bonding and the stability of the core. It is also possible that the bulky insertion may eventually split apart the β-sheet faces nearest the HAP protein slightly. While the β-helical structure is preserved in these variants, the self-assembly process likely differs. The R1 and R5 repeats direct the polymerization of WT CsgA,[104] while R2-R4 contain multiple "gatekeeper" residues (of aspartic acid or glycine) that slow curli growth of WT CsgA.[105] The removal of the R2-R4 beta strands includes removing charged residues from the β-sheet surface and turn regions. WT CsgA typically has a -6e charge, removing strands R2-R4 means removing 8 negatively charged residues and 3 positively charged residues variants, resulting in a net change of +5e from the WT CsgA and a total charge of -1e in the R1/R5 variants. While molecular-level details of fiber aggregation are not currently known, we expect that changing the charge distribution on the surface of the monomers will impact (and potentially impede) self-assembly and bundled structure. We also anticipate that including the HAP protein will alter bundle formation as fibril diameter has been shown to increase with the molecular weight of proteins fused to CsgA.[106] Previous investigation of CsgA-fusion proteins found the fibers still able to self-assemble, although with slower growth.[106] Overall, both the experimental circular dichroism data and our modelling

predictions indicate that truncated CsgA subunits adopts a β-helical fold that resembles that of WT CsgA.

Mineralization of curli-like proteins with HAP crystals

To analyze the functionality of the HAP-binding peptide integrated in the R1/HAP/R5 fibers, we performed mineralization studies on all three protein types. We compared the mineralized R1/HAP/R5 fibers with mineralized WT CsgA and truncated CsgA fibers in terms of composition, mineral density, and crystallinity.

To mineralize R1/HAP/R5 fibers, we first attempted to submerging the protein hydrogel in simulated body fluid (SBF). However, mineralization in SBF resulted in inhomogeneous and surface-only distribution of crystalline particles. The formation of large particles (2-3 microns) of various shapes (rod, flakes, hexagonal) indicated a rapid and uncontrolled deposition of minerals on the surface of the sample, with limited diffusion of calcium and phosphate ions into the bulk of the hydrogel (Figure S3. 3A). Second, to dilute the fibers and allow for *in situ* mineralization during expression, we attempted to mineralize the fibers directly in the culture medium as bacteria express the proteins by adding SBF to the culture. However, this method resulted in a two-fold lower protein expression (verified by a Congo Red pull-down assay) compared with proteins expressed in the absence of SBF, and in a low density of the mineral deposition on the proteins (Figure S3. 3B). Third, we mineralized the proteins using $CaCl_2$ and Na_2HPO_4 precursors instead of SBF, which yielded a uniform and dense formation of nano-sized minerals (Figure 3. 4A and Figure S3. 3C). Using this optimized method, we obtained a uniform deposition of the HAP nanostructures alongside the fibers. SEM images also show that the porous fibrous structure of the protein hydrogels was preserved after mineralization, a feature that would be important for using the mineralized scaffolds for bone tissue engineering applications. Furthermore, we confirmed the

formation of HAP crystals in the interior of the hydrogels by analyzing the cross-sectional morphology of the mineralized R1/HAP/R5 (Figure S3. 4).

To verify the crystallinity of these HAP nanostructures, we obtained the XRD pattern of the R1/HAP/R5 composite (Figure 3. 4B). The penetration depth of energetic X-rays within a sample is on the scale of ≈ 100 μm,[107] thus providing information about crystallinity within the bulk of the sample rather than the surface only. The XRD pattern of the mineralized proteins showed sharp peaks at 27.4°, 31.8°, 36.6°, and 45.7°, characteristic of crystalline HAP, which are assigned to (211), (300), (113), and (002) planes and are an indication of the crystallization of the hydrogel with HAP.[83, 108]

To better compare the extent of mineral formation onto the R1/HAP/R5 fibers with WT and R1/R5 fibers, residual salts and non-specifically bound HAP needed to be thoroughly washed off the samples prior to imaging. Therefore, we adapted a different protocol with a lower concentration of proteins and mineralization solution for TEM analysis. Figure 3. 4C shows images of curli-like proteins mineralized directly on TEM grids, along with a control grid incubated in the mineralization solution only (no proteins). We first used a control without proteins to determine how HAP would nucleate on the TEM grid without a protein template. We observed no formation of the crystalline HAP on these protein-free grids, highlighting the importance of protein templating for nucleation and crystal growth. Next, R1/R5-coated grids showed aggregates of particles, which we later characterized as amorphous particles. In contrast, TEM grids coated with R1/HAP/R5 and WT curli fibers showed substantial growth of flake-like crystals. We obtained dense aggregations of the flake-like particles of approximately 200 nm in the presence of R1/HAP/R5 nanofibers. While the density of HAP crystals was higher for R1/HAP/R5 fibers compared with WT, WT hydrogel also served as template for the growth of HAP. The formation

of HAP flakes (layers) onto WT proteins could be due to the presence of the charged amino acids in WT CsgA. Removing the internal repeats of CsgA resulted in removing the majority of the anionic amino acids (aspartic acid, glutamic acid) and cationic amino acids (arginine, histidine, and lysine). Charged amino acids are attracted to Ca^{2+} and PO_4^{3-} ions and promote HAP precipitation and the local supersaturation.[109] Therefore, they provide energetically favorable binding sites for the initial nucleation (and growth) of the minerals, which results in more stable and crystalline HAP nanoparticles. As a result, the R1/R5 protein, which lacks the favorable binding sites, showed no crystalline phase. Although we removed the internal repeats in the R1/HAP/R5 proteins, they are effective templates for formation of crystals. The dense and homogeneous deposition of the HAP nanocrystals in the mineralized R1/HAP/R5 was due to the incorporated HAP-binding peptides. Specific affinity of the HAP crystals to the binding peptide, along with the hydrogen bindings and electrostatic interactions, induced more specific and stable interaction as well as higher concentrations of the HAP nanocrystals with R1/HAP/R5.

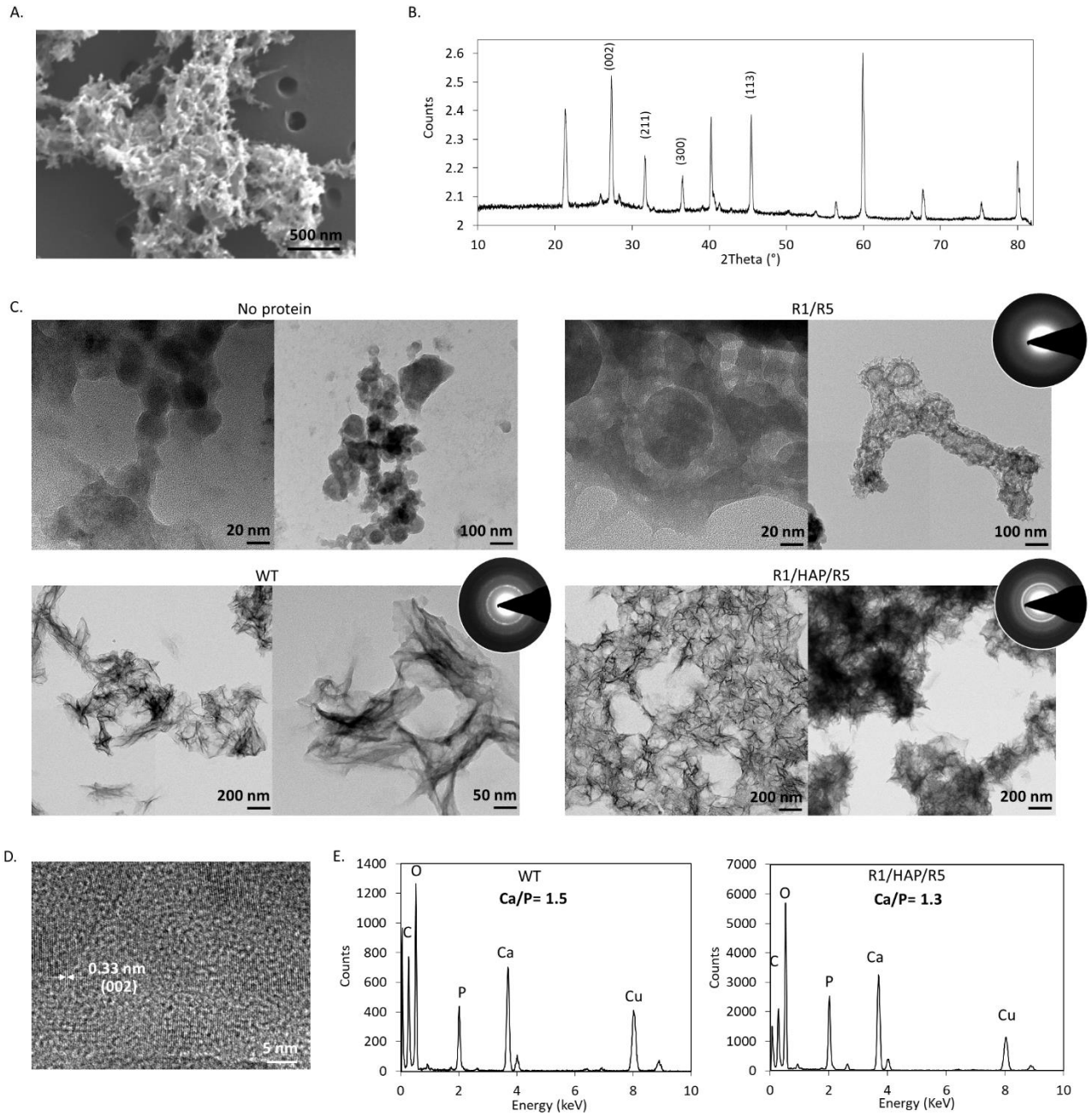

Figure 3. 4. Figure 2. Characterization of curli-based proteins mineralized with hydroxyapatite. (A) SEM image and (B) XRD spectrum of mineralized R1/HAP/R5 protein fibers. (C) HAP mineralized directly on TEM grids, without template (top left), and with protein fibers as templates (R1/R5, WT and R1/HAP/R5). TEM images show HAP nanoflakes formed by WT and R1/HAP/R5 proteins. SEAD patterns are shown for protein-templated HAP. Continuous rings are indicative of crystalline phase. (D) TEM image showing the interplanar spacing corresponding to the (002) plane of HAP nanoflakes. (E) EDS spectra highlighting the Ca/P ratio in the protein-templated HAP samples.

To compare the crystallinity of the minerals onto different protein templates, we obtained the selected area electron diffraction (SAED) patterns of the mineralized samples (Figure 3. 4C). R1/R5 with a halo pattern and R1/HAP/R5 with a sharp continuous arc-shaped pattern demonstrated the amorphous and crystalline phases of these samples, respectively.[87] The R1/R5 protein template generated amorphous HAP without any clear SAED pattern, while characteristic patterns confirmed the crystalline HAP mineral phase in the R1/HAP/R5-templated sample. When comparing R1/HAP/R5 with WT, we observed distinct diffraction rings for the R1/HAP/R5 sample corresponding to the hexagonal phase of HAP. The intensity of the diffraction rings in R1/HAP/R5 is indicative of the highly crystalline nature of the sample. In contrast, the SAED pattern for WT-templated HAP showed discrete spotted rings, indicating that WT proteins produce HAP crystals with a broader size distribution compared with R1/HAP/R5.[110] In addition, the interplanar spacing of 0.33 nm between the HAP lattice places in the R1/HAP/R5-HAP nanocomposites (observed by TEM, Figure 3. 4D) were ascribed to the (002) plane of HAP nanoflakes, further confirming the expected HAP crystal structure.[111] Together, these results indicate that the HAP-binding peptide plays an important role for directing the nucleation and growth of crystalline HAP in the modified curli-like fibers.

Finally, we investigated the composition of the protein-HAP samples by performing EDS analyses of the TEM samples. These analyses confirmed the presence of HAP templated by WT and R1/HAP/R5 proteins through a quantification of the calcium and phosphorus present in the mineralized proteins (Figure 3. 4E). The theoretical Ca/P atomic ratio for HAP ($Ca_{10}(PO_4)_6(OH)_2$) is 1.67, which corresponds roughly to the ratio calculated via EDS in the mineralized R1/HAP/R5 and WT (1.3 and 1.5, respectively).[112] It should be noted that EDS approximately characterizes only the surface of the sample and that the Ca/P ratio could change with airborne contaminations

or any remaining ions (PO_4^{3-} and Ca^{2+}) adsorbed on the surface, explaining the slight differences with the theoretical ratio. Overall, the similarity between the experimental and predicted ratios suggests that the nanoflakes are truly HAP nanocrystals.

Collectively, the mineralization results confirm the functionality of the HAP-binding peptide incorporated in the truncated CsgA subunit. We observed a greater density of HAP crystals for the R1/HAP/R5 samples compared with WT CsgA and truncated R1/R5 proteins. Therefore, the incorporation of the HAP-binding peptide is an opportunity to use the curli-like fibers as a template for mineralization for various applications.

3.6. Conclusion

With their ability to self-assemble and to tolerate genetic modifications, CsgA proteins are promising candidates for fabrication of the protein-based materials for a wide variety of applications. Herein, we analyzed the functionality and self-assembly ability of the CsgA-like proteins after removing the internal repeats (R2-R4) and replacing them with a HAP-binding peptide. We obtained detailed information about the fibrillation and mineralization of the modified CsgA. We observed a fibrillar structure for R1/R5 and R1/HAP/R5 proteins, supporting the fact that R1 and R5 are the necessary aggregation prone repeats to form fibers. We confirmed the functionality of the incorporated HAP-binding peptide after mineralization of the modified proteins, and we assessed the formation of the HAP crystals. Overall, the resulting HAP-containing hydrogels are potential candidates for bone tissue engineering applications requiring porous and densely HAP-mineralized 3D scaffolds.

Further, we showed that reducing the CsgA proteins into R1/R5 complementary self-assembling monomers is a means to genetically assist in the self-assembly of a short functional peptide into a

fibrous structure. This method circumvents the needs for post-processing chemical conjugation reactions that are traditionally required to attach free peptides to larger molecular scaffolds. Our new self-assembly tool thus brings an opportunity to repurpose free peptides as functional supramolecules to produce functional fibrous materials and hydrogels for a wide range of the applications, ranging from biotechnology, to tissue engineering, and energy.

Aside from assisting the assembly of the free peptides and increasing the density of the active sites within a material, the fibers that we have engineered here also share many fascinating properties of the native curli system of *E. coli*. The truncated curli materials form hydrogels with a high genetic customizability, that can resist harsh processing conditions, and can be isolated from bacterial cultures in macroscopic quantities. The versatile processability of these materials makes them suitable for fabrication of the proteins-based materials in different forms, such as films, hydrogels, and aerogels. Besides, the curli system can be used as scaffold to introduce different functional peptides to tune its physicochemical properties for a wide variety of applications.

3.7. Supporting information

Table S3. 1. Primers and sequences used in this study.

Constructs name	**Sequence**
Reverse primer (to remove CsgA)	5’ ATTTGGGCCGCTATTATTACCGCC 3’
Forward primer (to remove CsgA)	5’ TAC ATC ATT TGT ATT ACA GAA ACA GGG CGC 3’
Forward primer (to remove R2/R3/R4)	TCCTCCGTCAACGTGACTCAGGTTGGC
Reverse primer (to remove R2/R3/R4)	GCACTTGCTCTGCAAACTGATGCCCGTAAC
Flexible linker (L12)	GGATCGGCAGGTTCTGCAGCCGGTTCAGGTGA GTTT
Hydroxy apatite (HAP) binding site	AACCCGTACCATCCTACCATTCCCCAGTCAGT CCAC
Gblock for insertion of HAP-binding site	GCTCTGCAAACTGATGCCCGTAACGGATCGGC AGGTTCTGCAGCCGGTTCAGGTGAGTTTAACC CGTACCATCCTACCATTCCCCAGTCAGTCCAC GGATCGGCAGGTTCTGCAGCCGGTTCAGGTGA GTTTTCCTCCGTCAACGTGACTCAG
Gblock for insertion of R1/R5	GCGGTAATAATAGCGGCCCAAATTCTGAGCTG AACATTTACCAGTACGGTGGCGGTAACTCTGC ACTTGCTCTGCAAACTGATGCCCGTAACTCCTC CGTCAACGTGACTCAGGTTGGCTTTGGTAACA ACGCGACCGCTCATCAGTACTAATACATCATT TGTATTACAGAAACAGGG

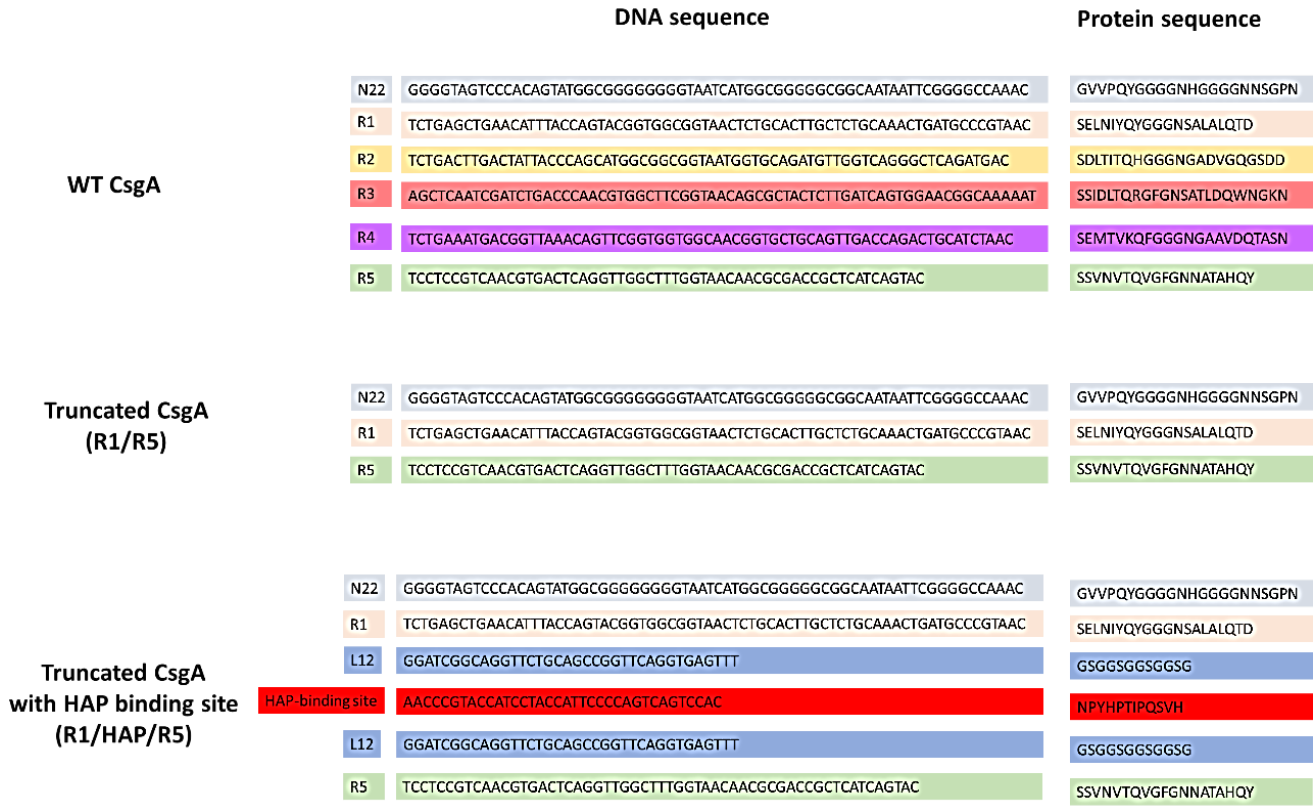

Figure S3. 1. DNA and protein sequences for CsgA and modified CsgA constructs.

Figure S3. 2. WT and modified curli proteins isolated on filter membranes after vacuum filtration. All three proteins form hydrogel-like substances once assembled.

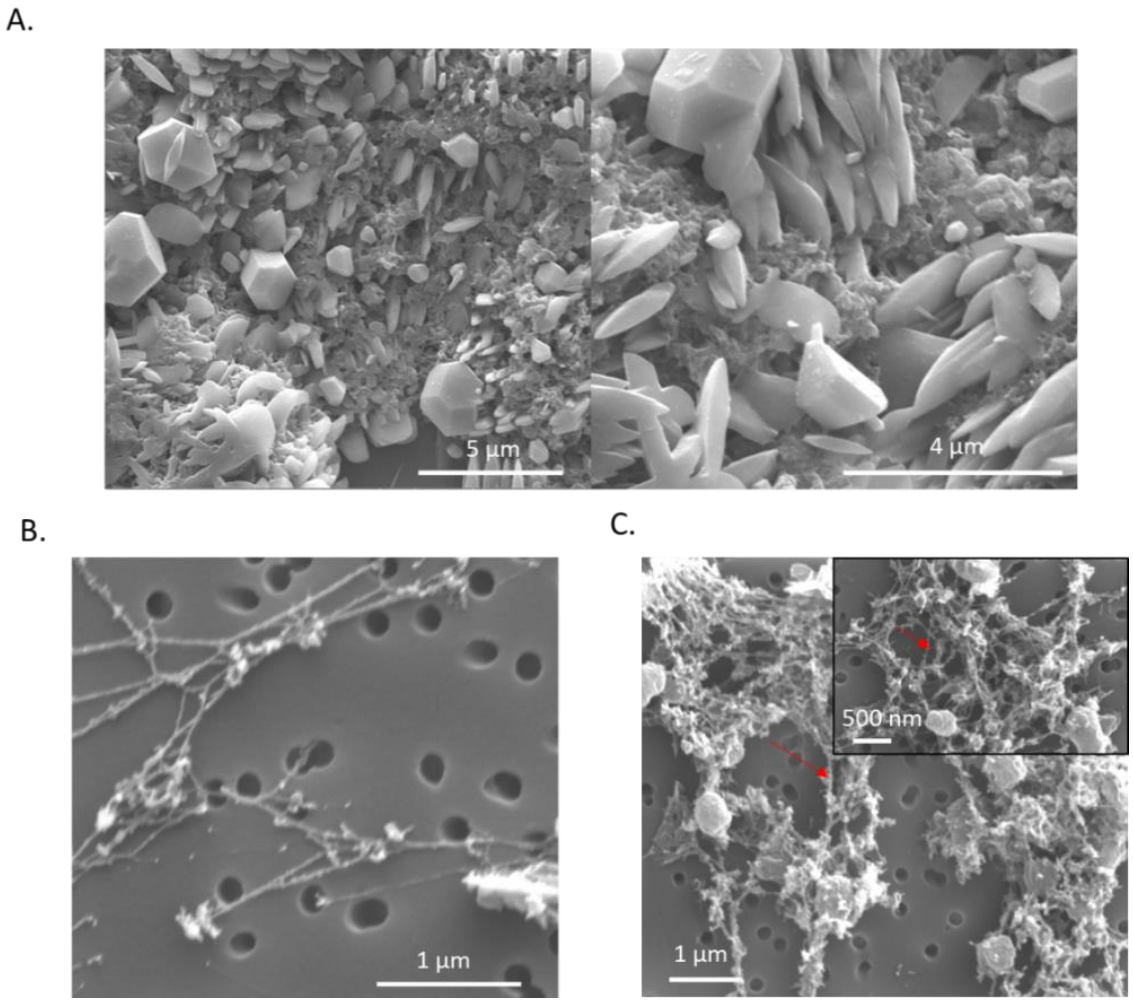

Figure S3. 3. SEM images of mineralized R1/HAP/R5 proteins with different protocols. (A) mineralized proteins by submerging the 1 mg of proteins in 2 mL of simulated body fluid (SBF) for overnight that resulted in micron-size minerals with various shapes, (B) In situ mineralization of the protein during expression by overnight incubation of the 5 mL of bacterial culture with 10 mL of SBF that resulted in less expression of proteins, (C) Mineralization of proteins using 100 mM CaCl2 and 50 mM Na2HPO4 precursors with uniform distribution of the HAP nanostructures alongside the fibers (Red arrows).

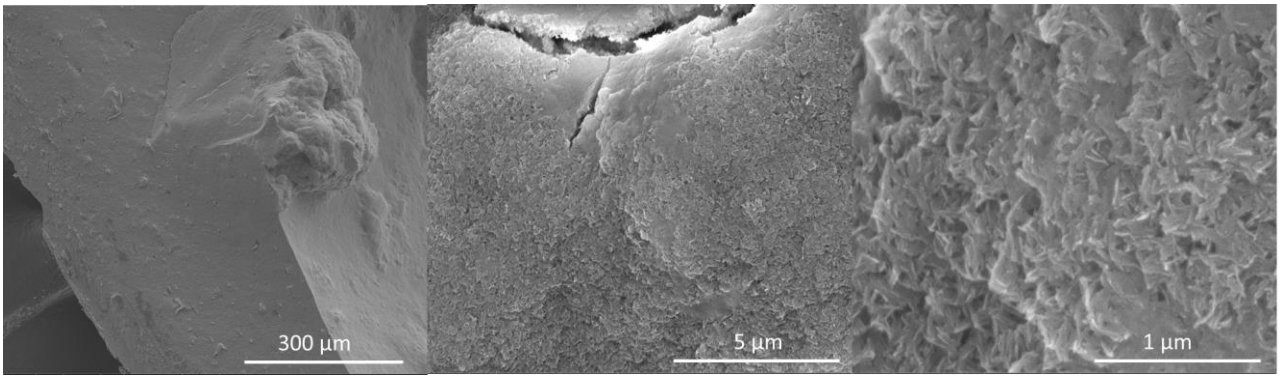

Figure S3. 4. SEM images of the cross-section of R1/HAP/R5 hydrogel after mineralization. The images show that HAP crystals are formed throughout the hydrogel.

3.8. Acknowledgments and funding sources

This research was funded, in part, by the Natural Sciences and Engineering Research Council of Canada (NSERC) through a Discovery grant (NSERC RGPIN-2017-04598), and it was undertaken, thanks to the support by the Canadian Foundation for Innovation (project #37524). This work was also supported, in part, by an Établissement de nouveaux chercheurs universitaires FRQNT grant (FRQ-NT NC-255846). S.K. acknowledges funding from the Office of Naval Research Young Investigator Program (grant #N00014-15-1-2701). This work was also supported by two research networks: the Québec Center for Advanced Materials (QCAM), and the Research Center for High Performance Polymer and Composite Systems (CREPEC), both supported by the FRQNT. Z.A. and M.A. are grateful for financial support by McGill Engineering Doctoral Awards (MEDA). O.X. is grateful for an NSERC Undergraduate Student Research Award. E.D.B. was additionally sponsored by the DoD, Air Force Office of Scientific Research, National Defense Science and Engineering Graduate (NDSEG) Fellowship, 32 CFR 168a. The authors acknowledge a supercomputing grant from the Northwestern University High Performance Computing Center and the Department of Defense Supercomputing Resource Center. E.D.B. gratefully

acknowledges support from the Ryan Fellowship and the Northwestern University International Institute for Nanotechnology. The authors thank the Facility for Electron Microscopy and Research (FEMR) at McGill for assistance with SEM and TEM, and McGill Chemistry Microscopy and Imaging Lab (MIlab) for access to AFM facility.

Chapter 4. Extracellular secretion and simple purification of bacterial collagen from *Escherichia coli*

4.1. Rationale for Chapter 4

Previously, bacterial collagen had been genetically modified and produced intracellularly in *E. coli* for biomedical applications. However, it is necessary to employ cell lysis for extracting the intracellular collagen, a step which could result in intracellular proteolysis, protein loss and contamination of the product with host proteins. Another current challenge for the massive production of the collagen comes from the downstream purification methods after expression. Traditional chromatography-based methods are costly, low yield, and difficult to scale-up. This chapter presents the methods for overcoming these challenges by extracellularly secreting bacterial collagen after its expression in *E. coli* and simplified purification protocols

We adapted and modified the extracellular secretion pathway of CsgA proteins and created a minimized secretion pathway with only essential genes for secretion of non-CsgA proteins. We also established downstream purification processes based on three main principles: 1) the enzymatic digestion of the unwanted proteins that are sensitive to proteases (while collagen is not), 2) the size-based separation of collagen via filtration, and 3) the concentration of the large volumes of the supernatant from bacterial cultures using acid precipitation. Using these approaches collagen recovery was facilitated.

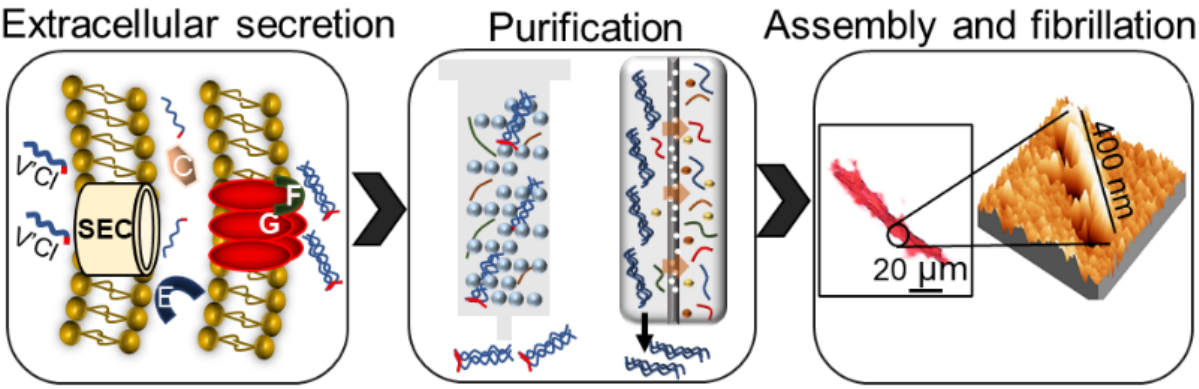

Chapter 4 is based on a manuscript entitled "Extracellular secretion and simple purification of bacterial collagen from *Escherichia coli"* published in *Biomacromolecules (2022,* 23, 4, 1557–1568*)* which was co-authored with Max Renner-Rao, Amy Chow, Anqi Cai, Matthew J. Harrington, and Noémie-Manuelle Dorval Courchesne.

4.2. Abstract

Due to structural similarities with type I animal collagen, recombinant bacterial collagen-like proteins have been progressively used as a source of collagen for biomaterials applications. However, the intracellular expression combined with current costly and time-consuming chromatography methods for purification makes the large-scale production of recombinant bacterial collagen challenging. Here, we report the use of an adapted secretion pathway, used natively by *E. coli* to secrete curli fibers, for extracellular secretion of the bacterial collagen. We confirmed that a considerable fraction of expressed collagen (~70%) is being secreted freely into the extracellular medium, with an initial purity of ~50% in the crude culture supernatant. To simplify the purification of extracellular collagen, we avoided cell lysis and used cross-flow filtration or acid precipitation to concentrate the voluminous supernatant and separate the collagen from impurities. We confirmed that the secreted collagen forms triple helical structures, using

Sirius Red staining and circular dichroism. We also detected collagen biomarkers via Raman spectroscopy, further supporting that the recombinant collagen forms a stable triple helical conformation. We further studied the effect of the isolation methods on the morphology and secondary structure, concluding that the final collagen structure is process-dependent. Overall, we show that the curli secretion system can be adapted for extracellular secretion of the bacterial collagen, eliminating the need for cell lysis, which simplifies the collagen isolation process and enables a simple cost-effective method with potential for scale-up.

Keywords: Bacterial collagen, recombinant collagen, extracellular secretion from *E. coli*, scalable protein purification, biomaterials.

4.3. Introduction

There is a tremendous need for protein-based materials that are derived from safe and biocompatible sources in the fields of biomaterials and tissue engineering. The occurrence of widespread disease among animals and associated health problems inhibits the production and use of animal source proteins. As a consequence, recombinant proteins are emerging as an important substitute that presents lower immunogenicity and inflammation response compared to animal sources. [113] Collagen is among the most abundant proteins in animals, and it plays a major structural and mechanical role in tissue formation. It is thus a protein of choice in different fields such as cosmetic, tissue engineering, and fabricating synthetic biomaterials. [1]

Among the different types of recombinant collagens, bacterial collagen-like proteins, such as Streptococcal collagen-like proteins, have a structure with mechanical and thermal stability compared to type I animal collagen.[15, 114, 115] The biofunctionality of this type of collagen is tailorable and has been genetically modified to alter its biological activities by fusing functional

protein domains, such as silk to the C-terminal end of bacterial collagen and single mutations to create integrin-binding domains in the backbone of the bacterial collagen. [18, 24, 26]

Bacterial collagen lacks hydroxyproline, which contributes to the stability of animal collagen and cannot be post-translationally modified in bacterial cells. Nonetheless, it still forms a stable triple helix structure.[15] Structurally, bacterial collagen consists of an N-terminal variable domain (globular domain, V) attached to a rod-shaped collagen-like domain (helical domain, CL). A high content of proline and highly charged repeating sequences can be found near the C-terminal and N-terminal ends of the collagenous domain, which are key for the structural stability of the bacterial collagen.[15] Investigations in synthetic peptides have demonstrated that charged residues found in the X and Y positions of the triplet (glycine-X-Y) can promote electrostatic interactions and water-mediated contact between the charged side chains, which accordingly stabilize the triple helix structure. [116, 117]

Bacterial collagen has been previously genetically modified and produced intracellularly in *E. coli* for biomedical applications. [18, 24-26] In these reports, cell lysis has been used as a necessary step for extracting intracellular collagen. However, the extracellular production of proteins has significant advantages compared to conventional intracellular production, on both analytical and industrial scales. For instance, the product quality (e.g. biological activity and stability) of the expressed proteins in the culture medium is better preserved by their continuous secretion and protection from intracellular proteolysis by periplasmic proteases.[27] Further, intracellular systems demand cell disruption, which results in protein loss and contamination with host proteins. In contrast, an extracellular system is exempt from cell lysis, which consequently makes the purification process simpler and less costly. [29]

One of the well-known and established extracellular secretion pathways is natively found in *Escherichia coli* bacteria and serves for the secretion of CsgA proteins. CsgA is a self-assembling bacterial protein that is secreted inherently by *E. coli* and assembles into membrane-bound extracellular curli fibers. [31-33] The structural components and assembly apparatus of CsgA consist of seven curli-specific genes (*csg*), which are encoded by two divergently transcribed operons (*csgBAC* and *csgDEFG*). These operons encode the structural subunit of the curli protein and other accessory proteins required for CsgA secretion and assembly.[31]

In the curli secretion pathway, the SEC peptide and N22 peptide are two important components responsible for directing the secretion of CsgA into the periplasm and then across the outer membrane, respectively. [31] These components are not specific to CsgA and are crucial for the extracellular secretion of other proteins through this pathway. CsgB is the nucleator protein, and in its absence, CsgA is secreted freely from the cell.[31] The CsgE protein is known as a curli secretion specificity factor that prevents premature amyloid fiber aggregation, and, therefore, is crucial for the secretion of CsgA and CsgA fusion proteins, but also does not interfere with the secretion of proteins containing the N22 secretion signal peptide.[118] CsgF is also responsible for the efficient nucleation of curli subunits into amyloid fibers and acts cooperatively with CsgB to initiate curli subunit polymerization near the cell surface. [119] It has been shown that the CsgG is an ungated, non-selective protein secretion channel in which the periplasmic polypeptides can be transported into the extracellular medium via its diffusion-based mechanism.[38] Additionally, the CsgG transporter is capable of exporting heterologous and non-native sequences, amyloid or not, when fused to the curli subunit CsgA [34] or a truncated form of CsgA.[120] The role of CsgC in this pathway remains to be fully elucidated, but it presumably has redox activity, with CsgG being the

potential substrate. Indeed, a mutant strain lacking the *csgC* gene was found to still assemble curli fibers but showing defects in auto-aggregation (Figure 4. 1A). [41]

The non-specificity of the CsgG transporter motivated us to seek inspiration from this existing system for extracellular secretion of the bacterial collagen. Thus, here, we propose an adapted secretion system that can be used for the extracellular secretion of bacterial collagen, using only the essential signal peptides and curli operon genes for the secretion of collagen. The extracellular production of proteins also indirectly permits their simplified purification, which is important for the scalable manufacturing of biomaterials. In addition, establishing a low-cost simple purification technique represents an important engineering contribution for the scalable manufacturing of protein-based materials. [33] Specifically, there are several main drawbacks with current chromatography-based methods, such as high cost, low yield, limited sample volume, and protein loss due to metal ions leakage, which all will limit the massive production of the collagen. Therefore, alongside extracellular collagen secretion, we also report simple purification protocols for isolating bacterial collagen, based on three main principles: the enzymatic digestion of the unwanted proteins by selectively cleaving proteins that are sensitive to proteases, the size-based separation of collagen via filtration, and the selective acid precipitation of collagen. [25, 121] Through precipitation and filtration, the large culture volumes can be processed and concentrated efficiently, facilitating collagen recovery.

Our work here verifies the hypothesis that the adapted curli extracellular secretion system can be used for the extracellular secretion of bacterial collagen. We also introduce the protocols for simple isolation of the secreted bacterial collagen. We characterize the morphology, secondary structure, and chemical structure of the isolated collagen samples, and study their processability for future potential applications in the fields of biomaterials and tissue engineering. This work opens up the

opportunity for using bacterial collagen as a major component of biomaterials, relying on the presented simplified secretion and scalable purification methods.

4.4. Materials and Methods

Cell strains, plasmids, and collagen expression. The pET21d-*csgACEFG* plasmid and the curli operon deletion mutant strain of *E. coli*, PQN4, were gifts from the Joshi Lab (Harvard University, Boston, MA). We used this pET21d plasmid, with the curli operon (without the CsgB nucleator protein) under the control of the T7 promoter, as a template vector to synthesize the bacterial collagen. On this template vector, we genetically added the encoding genes that are necessary for extracellular secretion of the bacterial collagen and eliminated the *csgA* gene, which encodes the major subunit of the curli fibers, CsgA, and replaced it with a gene encoding bacterial collagen. To do so, first, we linearized the pET21d-*csgACEFG* plasmid using forward and reverse primers starting immediately downstream and immediately upstream, respectively, to remove the csgA gene. Then, the collagen DNA fragment (Life technologies) was inserted downstream of N22 using an isothermal Gibson assembly reaction (New England Biolabs). Also, a translational enhancing element (TEE) encoding the amino acids MNHKVHM was added at the N-terminus of the collagen sequence, which has been shown to enhance translation initiation.[122] The TEE was followed by a six-histidine tag (His-tag) to allow for immunodetection. The templated vector for the secretion system, which consists of the genes expressing SEC, N22, His-tag, and collagen, and the curli-specific genes (*csg*), *csgC, csgE, csgF*, and *csgG* (pET21d-v'cl-csgCEFG) was transformed into *E. coli* PQN4 and BL21(DE3) (New Englan Biolabs). In another approach, we also deleted *csgC* and *csgF* to further investigate their effect on the extracellular secretion of the bacterial collagen (pET21d-*v'cl-csgEFG* and pET21d-*v'cl-csgEG*).

Figure 1A demonstrates the arrangement of the encoding genes on the template vector. To express the proteins, the transformed PQN4 cells were streaked onto lysogeny broth (LB) agar plates containing 100 μg/mL carbenicillin and 0.5% (m/v) glucose (for catabolite repression of T7 RNA polymerase). Colonies were picked from the plates, and 5 mL cultures were inoculated in LB medium (containing 100 μg/mL carbenicillin and 2% (m/v) glucose). Cultures were grown overnight at 37 °C with an agitation rate of 250 rpm. The overnight cultures were diluted 100-fold in fresh LB medium with 100 μg/ml carbenicillin, and protein expression was allowed to proceed at 37 °C overnight. The protein sequence of the bacterial collagen and DNA sequences of all the genes and primers are listed in Figure S4. 1.

Assessment of collagen expression, purity, and secretion by SDS-PAGE and Western blotting. We confirmed the expression of His-tagged collagen and its secretion into the culture medium by running an SDS-PAGE gel of different fractions of the culture and detecting collagen via Western blot. We used three samples; a 30 μL sample taken from a 5 mL freshly expressed culture, supernatant (30 μL), and washed bacterial pellets (30 μL). To prepare the pellets, we centrifuged 1 mL of the culture, removed the supernatant, and after 1 wash with HCl 0.05 M, and two washes with water, they were resuspended with 1 mL water. We ran all samples on a NuPAGE Novex 4−12% Bis-Tris gel and transferred them on an iBlot PVDF membrane (Invitrogen). We treated the membrane with a monoclonal mouse anti-His antibody, the HRP conjugate (Abcam), after blocking with 5% milk in TBST. We detected the chemiluminescence using a FluorChem M system (Protein Simple). We used ImageJ to calculate the intensity of the bands by quantifying the bands corresponding to supernatant and pellets relative to the intensity of the band corresponding to the culture.

We also loaded the same samples on TGX gel and stained them with Coomassie Blue for more assessment along with the western blot results. We also used SDS-PAGE to assess the purity of the purified collagen samples and confirm their molecular weights. After re-suspending the 30 µL of the purified collagen solution (5 mg/mL) in 10 µL 4X Laemmli loading buffer, it was loaded in every 50 µL-wells of a pre-cast Mini-Protean TGX gel (Bio-Rad Laboratories). The gels were electrophoresed at 200 V for 30 minutes and then stained with Coomassie Blue.

Assessment of collagen expression, secretion, and folding by Sirius Red staining. The supernatant of collagen expressing culture was stained with Sirius Red and Masson's Trichrome and was compared with the supernatant of a non-transformed PQN4 culture, as control. For Sirius Red staining, ~ 10 µL of the supernatant were air-dried on a glass slide for 5-10 min and were heat-fixed by gently passing the slides over a flame. The slides were immersed for 1 h in saturated picric acid containing 0.1% Direct Red 80 (i.e., Sirius Red, Sigma) and washed with 0.5% acetic acid (2 times for 2 min). The slides were dehydrated by increasing concentrations of absolute alcohol (95%, 100%, 100%) each for 2 min followed by a xylene wash and mounted in Neo-Mount resin (VWR). Birefringence images of the stained samples were taken using a polarized light microscope (Axio Scope.A1, Zeiss) equipped with a 6-megapixel CCD camera (Axiocam 505 color, Zeiss). We used rat tail collagen (Sigma-Aldrich) as a control for type I animal collagen. We also stained the purified collagen samples with Sirius Red to study the effect of the purification process on their structures.

For Masson's Trichrome (Sigma Aldrich) staining, the manufacturer's protocol was followed. Briefly, the samples were stained for 5 min stepwise in separate solutions of Weigert's Iron Hematoxylin, Biebrich Scarlet-Acid Fuchsin, phosphomolybdic-phosphotungstic acid, and aniline

blue. The same steps as Sirius Red staining were followed for washing, dehydrating, mounting, and imaging.

Purification of collagen proteins using Ni–NTA column. We used Ni–NTA column for collagen purification as a gold-standard method. To do so, we first filtered the collected supernatant through 0.2 µm bottle filters (Thermo Fisher) to remove the large particulates and possible remaining bacteria. We incubated the Ni–NTA column with the supernatant for 2 hours, washed with 40 mM imidazole solution 5 times to remove the non-specifically bound proteins, and washed with 500 mM imidazole solution to elute the bound proteins. Then, the eluate was concentrated and washed with a 30 kDa PALL centrifugal filter. To remove the non-collagen domain (V'), the purified protein was adjusted to pH=2.2 with HCl 0.5 M and incubated with trypsin (0.01 mg/mL) for 24 hours at 4 °C. To stop the digestion, the pH was adjusted with 0.5 N NaOH to pH 8.0 and the protein solution was washed through a 10 kDa PALL centrifugal filter.

Isolation of collagen proteins using digestion/cross-flow filtration. We collected the supernatant by 30 min centrifugation at 4000 x g. After filtering the supernatant through 0.2 µm bottle filters, we lowered the pH to 2 (optimum pH for pepsin function [123]), added pepsin to the supernatant at a final concentration of 0.01 mg/ml, and incubated at 4 °C for overnight for pepsin to digest the pepsin-sensitive impurities. Next, we concentrated the voluminous crude protein solution by cross-flow filtration. We used a Minimate^{TM} tangential flow filtration system (Pall Life Sciences) to filter 500 mL of digested supernatant through a 10 kDa molecular weight cut-off (MWCO) membrane. The permeate containing small solutes and digested proteins were discarded, and the concentrated retentate (containing collagen) was collected as the product (Figure 4. 2A). The retentate was further washed with 500 mL of 10 mM sodium phosphate buffer pH = 7.4.

Isolation of collagen proteins using digestion/precipitation. Another approach to concentrate the large volume of the digested supernatant was acid precipitation. We used phosphotungstic acid (PTA), at a final concentration of 0.1%, to precipitate the digested and non-digested proteins (collagen) from 100 mL supernatant. To prevent the denaturation of the collagen structure during acid precipitation, we added erythritol (0.5 M) to the protein solution and incubated it on ice for 2 min (Figure 4. 2A). After collecting the precipitated proteins by centrifugation at 4000 xg for 5 min, we washed the precipitates with 5 mL acetone 2 times and air-dried them for 30 min. Then, the precipitate was resolubilized in 10 mL NaOH (0.05 N) and washed with a 10 kDa centrifugal filter (Pall) to remove the remaining small-size digested impurities from the final product. After the isolation process, the collected purified collagen solution (1 mL) was further washed with 10 mM sodium phosphate buffer pH = 7.4 with the centrifugal filter and lyophilized.

Electron Microscopy. Samples for Scanning electron microscopy (SEM) were prepared by depositing 50 µL of the freshly expressed bacterial culture and the purified collagen samples on 0.2 µm polycarbonate filter membranes (Whatman® Nuclepore from Millipore Sigma). The membranes were washed with 0.1 M sodium cacodylate buffer (Electron Microscopy Sciences), fixed with 2% (v/v) glutaraldehyde (Bio Basic) and 2% (v/v) paraformaldehyde (Electron Microscopy Sciences) for 2 hours at room temperature, and solvent-exchanged sequentially in 0%, 25%, 50%, 75%, and 100% (v/v) ethanol (for 15 min in each solvent). The membranes were dried in a critical point dryer (CPD) and sputtered with 5 nm Pt. Imaging was performed using an FEI Quanta 450 ESEM at 5 kV.

Nanostructure of the collagen fibril. Atomic force microscopy (AFM) was used to study the nanostructure of self-associated collagen fibers. 0.5 mg of the collagen purified via Ni-NTA chromatography was re-solubilized in 1 mL of 1 mM phosphate buffer at pH= 7.4. The collagen

solution was incubated at 37 °C for 1 hour to facilitate the fibrillogenesis and self-association of the collagen fibrils. Then, 4 μL of the protein solution was added onto a freshly cleaved mica sheet and was allowed to dry overnight. The samples were imaged using a Veeco Multimode Nanoscope III AFM with a 240AC-NA microcantilever tip (Opus).

Circular Dichroism (CD) spectroscopy. A Chirascan spectrophotometer (Applied Photophysics) was used to evaluate the secondary structure of the engineered proteins. Measurements were performed in a quartz cell with a 1-mm path length from 180 to 260 nm at 20 °C, using a 1 nm step size and a bandwidth of 1 nm. The protein solutions were prepared by dissolving 0.5 mg of the proteins in 1 mL of water, followed by 30 s vortexing to fully dissolve the proteins. All spectra were baseline corrected with respect to water. Also, using a Jasco J-815 circular dichroism spectrophotometer the protein melting was monitored at 198 nm by increasing temperature in 1°C increments from 5 to 50°C, at pH=5. Proteins were maintained for 1 min at each temperature, with the average rate of temperature increase of 1 °C/min.

Polarized Confocal Raman Spectroscopy. Confocal Raman spectroscopy of the collagen samples was performed under dry conditions after casting the protein solutions onto glass slides. A green laser (Nd/YAG laser, λ = 532 nm) was focused using a confocal Raman microscope equipped with a motorized scanning stage (Alpha300R, WItec, Ulm, Germany). The scattered light was detected by a thermoelectrically cooled CCD detector (Andor, Belfast, North Ireland) placed behind the spectrometer (WItec). Using a 100× objective (Zeiss, NA = 0.9), individual point scans of vesicles contained large contributions from the surrounding glass and dried buffer; therefore, image scans were performed with laser power of 27 mW, polarization angles of 0° (perpendicular to major axis) and 90°(parallel to major axis), and integration time of 1.5 s per point.

Processing of collagen samples. To test the potency of the collagen for being used in different forms for biomaterials applications, collagen was processed in the forms of free-standing films and hydrogel crosslinked with genipin, a naturally derived chemical crosslinker. To form the collagen films, a collagen solution (10 mg/mL) in 0.01 M acetic acid was incubated at 4 °C overnight, cast on glass slides, and air-dried overnight. An aqueous solution of collagen (5 mg/mL) was crosslinked by mixing with a solution of genipin (Abcam) in DMSO: PBS (1:3) with final concentrations of 2.5 and 5 mM. The collagen-genipin mixture was incubated at 37 °C overnight. To induce the gelation of the collagen, an aqueous solution of collagen (5 mg/mL) was incubated with 2.5% sodium dodecyl sulfate (SDS) at 37 °C overnight.

UV-vis analysis was used to confirm cross-linking by observing a characteristic absorption peak at 585 nm. Since genipin also endows the crosslinked proteins with an intrinsic fluorescence, the fluorescent properties of the genipin-crosslinked hydrogels were studied by a fluorometer (Thermo Fisher). The excitation wavelength was 590 nm and emission spectra were collected from 600 to 700 nm. To assess the effects of SDS and genipin on the rheological properties of the collagen, we measured the viscosity of the samples at different shear rates using an Anton Paar MCR 302 rheometer. The measurements were operated with a 12 mm diameter cone-plate geometry (CP12). To prevent evaporation, the rheometer was equipped with a temperature-controlled hood. 200 µL of the samples were carefully placed onto the surface of the lower plate, and the upper cone was lowered to a 0.5 mm gap distance. Before testing, the hydrogels were resting for 2 min to equilibrate their mechanical stability. During the amplitude sweeps, the frequency was kept constant at 1 rad s^{-1}. The frequency sweep was conducted from 10 to 1 rad s^{-1}.

4.5. Results and Discussion

Expression and extracellular secretion of bacterial collagen

After transforming the bacteria, we sought to determine whether collagen could be expressed and secreted extracellularly as expected through the curli secretion pathway. To do so, we searched for the presence of His-tagged collagen in the whole bacterial culture, in the supernatant only, and in the bacterial pellet only, using SDS-PAGE and Western blotting (Figure 4. 1B). In the culture and supernatant, we observed a band close to the expected molecular weight of the bacterial collagen (~ 34 kDa), which consists of the N-terminal variable domain plus N22 (V'), translational enhancing element (TEE), His-tag, trypsin-sensitive region (for selective isolation of the collagen domain), and collagen domain (CL) (Figure 4. 1B, lane 1&2). This band was slightly higher (~ 44 kDa) than the theoretical molecular weight of the construct, which is common for rod-shaped proteins.[124] The intensity of this band extracted from the pellet was weak and hard to distinguish (with an intensity of less than 1% of that of the whole culture), which indicates that the fraction of bacterial collagen that remains trapped inside the cells is negligible (Figure 4. 1B, lane 3). As expected, the intensity of the band in the supernatant fraction was significantly higher (~70% of the intensity of the whole culture). Thus, after expression, a considerable fraction of the collagen (~70%) is being secreted freely in the extracellular medium. The remaining fraction (~30%), while not present in the washed pellet, may remain weakly associated with the pellet before washing with dilute hydrochloric acid and water. This extracellular, but pellet-associated collagen does not appear on the gels since the pellet that was run was washed. As a control for the pET21d vector and the secretion pathway, we used pET21d-MBP (maltose binding peptide, a 42.5 kDa soluble protein) and ran an SDS-PAGE for the fractions from culture, supernatant, and pellet (Figure S4. 3A). The control showed that in the absence of the curli secretion pathway, no MBP was secreted

into the extracellular medium. We also looked at the molecular weight of the proteins in the culture from untransformed PQN4 cells (control for the transformed cells) which indicated no protein corresponding to our protein of interest (collagen) (Figure S4. 3A).

Taken together, these observations indicate that the supernatant can be used in subsequent purification processes and can readily enable the recovery of more than 70% of the expressed collagen. Our observations also imply that the curli secretion pathway is not specific to the secretion of CsgA proteins, [34, 38] and is instead compatible with the secretion of other proteins that are not CsgA, CsgA-like, or fused to CsgA, such as collagen. Indeed, the N-terminal fusion of the SEC and N22 peptides was sufficient to ensure the efficient secretion of collagen.

We further modified the secretion pathway by removing CsgC and CsgF, and we assessed the secretion of the collagen into the extracellular medium using SDS-PAGE (Figure 4. 1C, D) and Western blot (Figure S4. 3B). Similar to the unmodified pathway (pET21d-*v'cl-csgCEFG*), the modified secretions pathways lacking CsgC and CsgF were able to direct the collagen into the extracellular media (Figure S4. 3B). The results indicate that collagen is secreted into the extracellular medium even in the absence of CsgC and CsgF. A sharp band at around 44 kDa was observed for all three modified pathways (pET21d-*v'cl-csgCEFG*, 2: pET21d-*v'cl-csgEFG*, 3: pET21d-v'cl-csgEG (Figure 4. 1D, lanes 1, 2, 3). In addition, the presence of the collagen was detected in the supernatant for all samples, indicating constant levels of extracellular secretion. This observation indicates that CsgC and CsgF are not necessary components for the extracellular secretion of the bacterial collagen, a principle which we postulate could be generalized to other non-CsgA proteins secreted via this pathway.

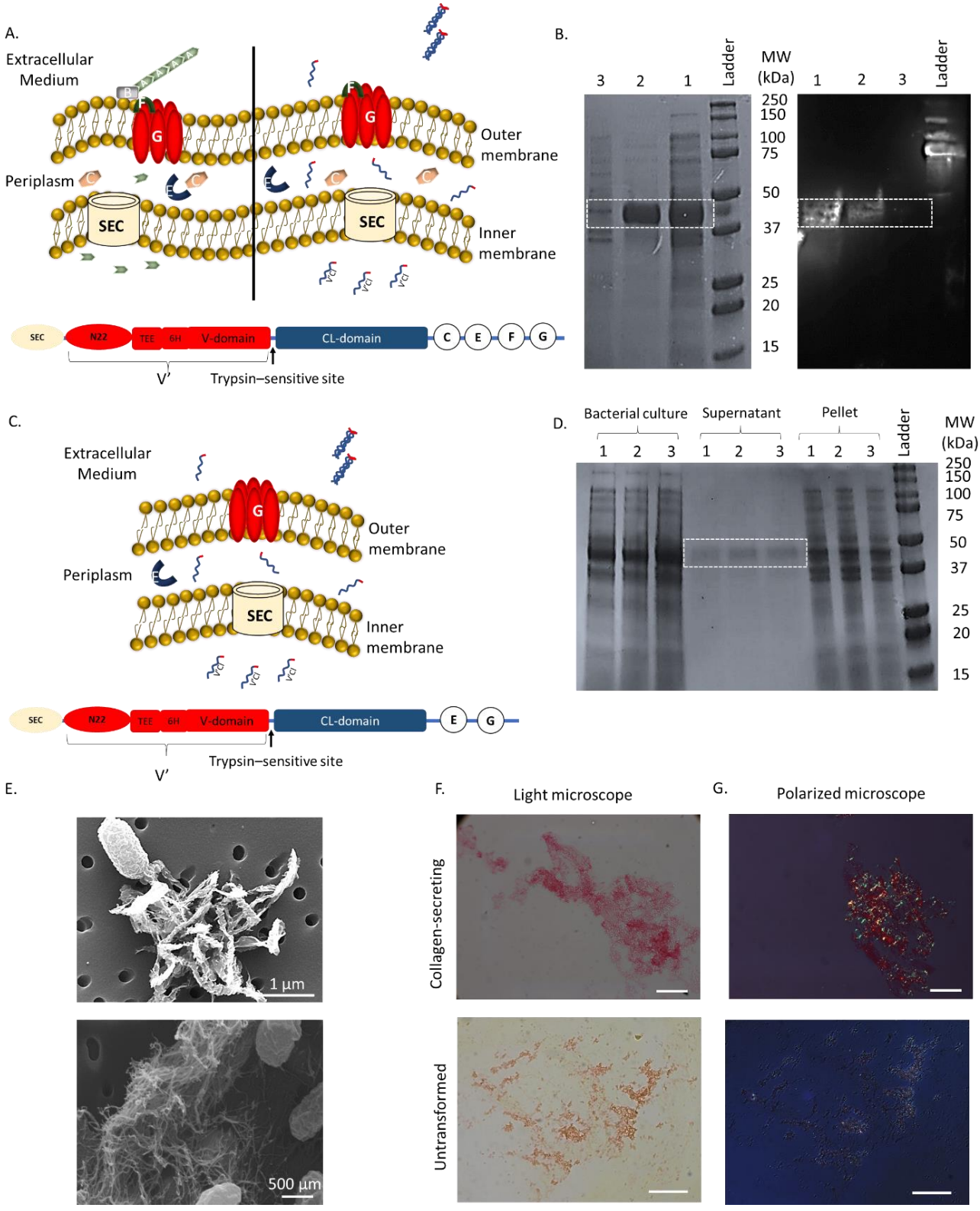
A.
Extracellular Medium
Outer membrane
Periplasm
SEC
SEC
Inner membrane
SEC
N22
TEE
6H
V-domain
CL-domain
C
E
F
G
V'
Trypsin–sensitive site
B.
3
2
1
Ladder
MW (kDa)
250
150
100
75
50
37
25
20
15
1
2
3
Ladder
C.
Extracellular Medium
Outer membrane
Periplasm
SEC
Inner membrane
SEC
N22
TEE
6H
V-domain
CL-domain
E
G
V'
Trypsin–sensitive site
D.
Bacterial culture
Supernatant
Pellet
1
2
3
1
2
3
1
2
3
Ladder
MW (kDa)
250
150
100
75
50
37
25
20
15
E.
1 µm
500 µm
F.
Light microscope
Collagen-secreting
Untransformed
G.
Polarized microscope

Figure 4. 1. Extracellular secretion of bacterial collagen from E. coli cells. (A) The arrangement of the encoding genes of the necessary components for extracellular secretion of the bacterial collagen (bottom) and the existing extracellular secretion pathway for curli fibers consists of SEC, N22, CsgB, CsgA, CsgC, CsgE, CsgF, and CsgG (top, left), and adapted pathway for the secretion of collagen, where CsgB and CsgA are removed (top, right). CsgE and CsgG are necessary for both pathways. (B) Distribution of collagen in the bacterial culture after separation of the pellet and supernatant. Detection of His-tagged collagen in each fraction via Western Blot (right) and its representative stained SDS-PAGE gel (left). 1: bacterial culture, 2: supernatant, 3: pellet. (C) The modified secretion pathway where CsgB, CsgA, CsgC, and CsgF components are removed, and the corresponding gene arrangement. CsgA, CsgB, CsgC, and CsgF are only necessary when secreting curli fibers. (D) The extracellular secretion of collagen in the bacterial culture through the modified pathway shown by SDS-PAGE. Distribution of the collagen in the bacterial collagen after separation of the pellet and supernatant related to the different modified vectors, 1: pET21d-v'cl-csgCEFG, 2: pET21d-v'cl-csgEFG, 3: pET21d-v'cl-csgEG. (E) SEM images of bacterial cultures expressing collagen, showing extracellular fibrillar structures. (F, G) Observation of secreted triple helical structures from collagen-secreting PQN4 cells. Images of Sirius Red stained cultures are taken both under the light microscope (F) and polarized light microscope (G). The triple helical structure of the collagen appears red under the polarized light, compared with the untransformed PQN4 cells, indicating the collagen secreted extracellularly was able to form a stable triple helix. Scale bars: 20 µm.

Additionally, we confirmed the presence of assembled collagen in bacterial cultures after expression using SEM. Figure 4. 1E shows extracellularly secreted collagen (alongside an *E. coli* cell) and its fibrillar morphology, after self-associating into fiber meshwork in the bacterial culture. The presence of these self-assembled collagen fibers and aggregates directly in the bacterial culture suggests that collagen molecules begin forming fibrils and bundle into networks immediately after expression and secretion.

To further visualize the secretion of triple helical structures into the extracellular medium, we stained the supernatant of cultures expressing collagen using Sirius Red and Masson's trichrome dyes and compared them with cultures prepared with untransformed PQN4 cells (Figure 4. 1F, G). Fibrillar collagen is highly anisotropic and forms a complex with Sirius Red that enhances the birefringence observed with polarized light microscopy, which can allow distinguishing collagen

from non-collagenous proteins.[125] Moreover, the presence of basic amino acids in collagen makes the interaction with the dye stronger.[79] Under unpolarized light, stained fibrillar collagen is expected to appear red. Light microscopy of Sirius Red-stained samples revealed that untransformed PQN4 culture appeared orange, while the supernatant collected from collagen-secreting culture appeared pink-red (Figure 4. 1E). Under polarized light, fibrillar collagen stained with Sirius Red typically exhibits strong birefringence in a range of colors, from yellowish-orange to orange-red. Here, we observed these colors for the collagen-secreting culture only, and not for untransformed PQN4 cells, indicating the presence of extracellular collagen-like structures in PQN4 cells transformed with the pET21d-*v'cl-csgCEFG* (Figure 4. 1F). The area with the bright yellow/orange color indicates larger and denser aligned collagen fibers (Figure 4. 1F, top). In addition, we stained the supernatant of cultures expressing collagen corresponding to pET21d-*v'cl-csgEFG* and pET21d-*v'cl-csgEG* using Sirius Red (Figure S4. 2). The stained samples appeared red in light microscopy indicating positive staining for collagen and showed birefringence in polarized light microscopy indicating alignment of the collagen molecules. Staining the samples with Masson's trichrome dye also revealed positive staining for collagen. With this method, collagen is expected to produce a blue color while other non-collagen components usually appear in red, pink, brown, and black. [20] The supernatant of the culture expressing collagen appeared intense blue after staining, compared with untransformed PQN4 cells, which appeared pink (Figure S4. 3). Together, these observations consistently indicate the presence of collagen in the extracellular medium of transformed cells.

Isolation of secreted collagen and its process-dependent morphology

Since collagen is secreted into the extracellular medium, its isolation does not require cell lysis and collagen can be directly purified from the supernatant. After collecting the supernatant, we

isolated collagen using three primary methods: 1) affinity chromatography with Ni-NTA, along with two scalable methods, 2) size-based separation via cross-flow filtration, and 3) collagen precipitation with phosphotungstic acid (PTA). These scalable methods can be preceded by a pepsin digestion step to digest protease-sensitive proteins in the supernatant (except the collagen, which is resistant to pepsin digestion) and facilitate subsequent purification steps. They are then performed in a fairly quick manner, using simple size-based separation techniques (filtration and centrifugation). One liter of pepsin-digested supernatant could be purified in a 2-hour purification process with these methods. Notably, purification via precipitation also allows for considerably reducing the sample volume at an early stage in the process, from a large bacterial culture down to a few milliliters of product which can easily be lyophilized. Compared with the time that Ni-NTA purification takes (~ 1 hour to purify 10 mL supernatant), this high productivity is an advantage for scalable manufacturing of biomaterials.

We aimed at comparing the purity and structure of the collagen products isolated from scalable methods with those of collagen obtained from well-established Ni-NTA purification. After purification by the three introduced methods (Figure 4. 2A), we verified the purity of the products using SDS-PAGE (Figure 4. 2B). We compared the purity of the collagen samples obtained from pepsin digestion followed by precipitation (D-P) and from pepsin digestion followed by cross-flow filtration (D-CF) with the collagen obtained from Ni-NTA chromatography (V'CL/Ni). SDS-PAGE of the collected crude supernatant (without digestion or purification) showed a strong band for collagen with an initial approximate purity of 45%-50%. This relatively high initial purity in the crude supernatant is because no cell lysis is needed for the extraction of collagen, preventing the release of intracellular proteins. We have made this observation for both collagens expressed in PQN4 cells and BL21 cells (Figure 4. 2B, lanes 1 & 2, respectively). In all of the digested

samples, we observed a band corresponding to the helical domain of bacterial collagen (CL domain) at around 23 kDa (Figure 4. 2B, lanes 3,4,6,8,9). During the digestion step, the non-helical portions of the collagen construct, which are susceptible to protease digestion, were cleaved, while the helical domain (CL) remained intact with no cleavage or digestion during the purification process. After the pepsin digestion, the bands corresponding to impurities at higher and lower molecular weight than CL domain (23 kDa) were diminished and an intense band at around 12 kDa was appeared, showing the digested impurities (Figure 4. 2B, lane 3). The purity of the collagen obtained from Ni-NTA (Figure 4. 2B, lane 5) was relatively higher than the two other purification methods (Figure 4. 2B, lanes 4, 6-9) and showed no non-specifically bound impurities to the Ni-NTA column. To remove low molecular weight proteins after purification, we employed centrifugal filters with 10 kDa or 30 kDa MWCO. When a 10 kDa centrifugal filter was used, we still observed a band corresponding to the ~12 kDa V' fragment comprising N22, the non-helical domain, and the His-tag (Figure 4. 2B, lanes 4, 6). This band disappeared when a 30 kDa centrifugal filter was used (Figure 4. 2B, lanes 8, 9). We also tested the purity of crude culture supernatant that was not exposed to pepsin digestion but only filtered with 50 kDa and 30 kDa MWCO centrifugal filter (V'CL/CF, Figure 4. 2B, lane 7). In the first step, impurities with a size greater than 50 kDa were trapped in the filter, and in the second step, impurities with a size smaller than 30 kDa passed through the filter while the product was retained. Since the impurities were not digested, the purity of the V'CL/CF (~70%) was lower than other samples purified by other purification methods. In this sample, the purity improved in comparison with the crude supernatant (Figure 4. 2B, lanes 1 & 2), which means that by simply filtering the supernatant an adequate purity may be obtained for the collagen depending on the application.

We then compared and quantified the purity of the collagen products obtained with each method. Ni-NTA yielded a collagen product with almost 100% purity, without any protein impurities visible on SDS-PAGE (Figure 4. 2B, lane 5), and with a ~ 0.5 g/L yield. Indeed, this highly selectively Ni-NTA column enabled retention of only the His-tagged proteins (Figure S4. 2). In comparison, we obtained purity of ~ 90% for CL/D-CF samples when washed with 30 kDa filters (Figure 4. 2B, lane 7), with a yield of ~ 0.4 g/L. While the yield for collagen purified via cross-flow filtration is comparable and even slightly lower than chromatography purification, cross-flow filtration is a technique that is more suitable for scale-up, could easily be adapted to isolate collagen for large culture volumes and could be used in a continuous process. Finally, the purity of the CL/D-P sample was ~ 60% and ~80%, when washed with 10 kDa and 30 kDa filters, respectively (Figure 4. 2B, lanes 4, 8). We observed a lower yield for the latter (60 mg/L) compared with the filtration method. This can be explained by the fact that acid precipitation does not result in the precipitation of all protein content in the supernatant, thus yielding less product. Although fewer protein impurities appeared in the collagen/Ni sample, it is a tedious and time-consuming process, in which both the high cost and trace of Ni ions in the final purified product has been an enormous concern in other collagen-based biomaterials.[126]

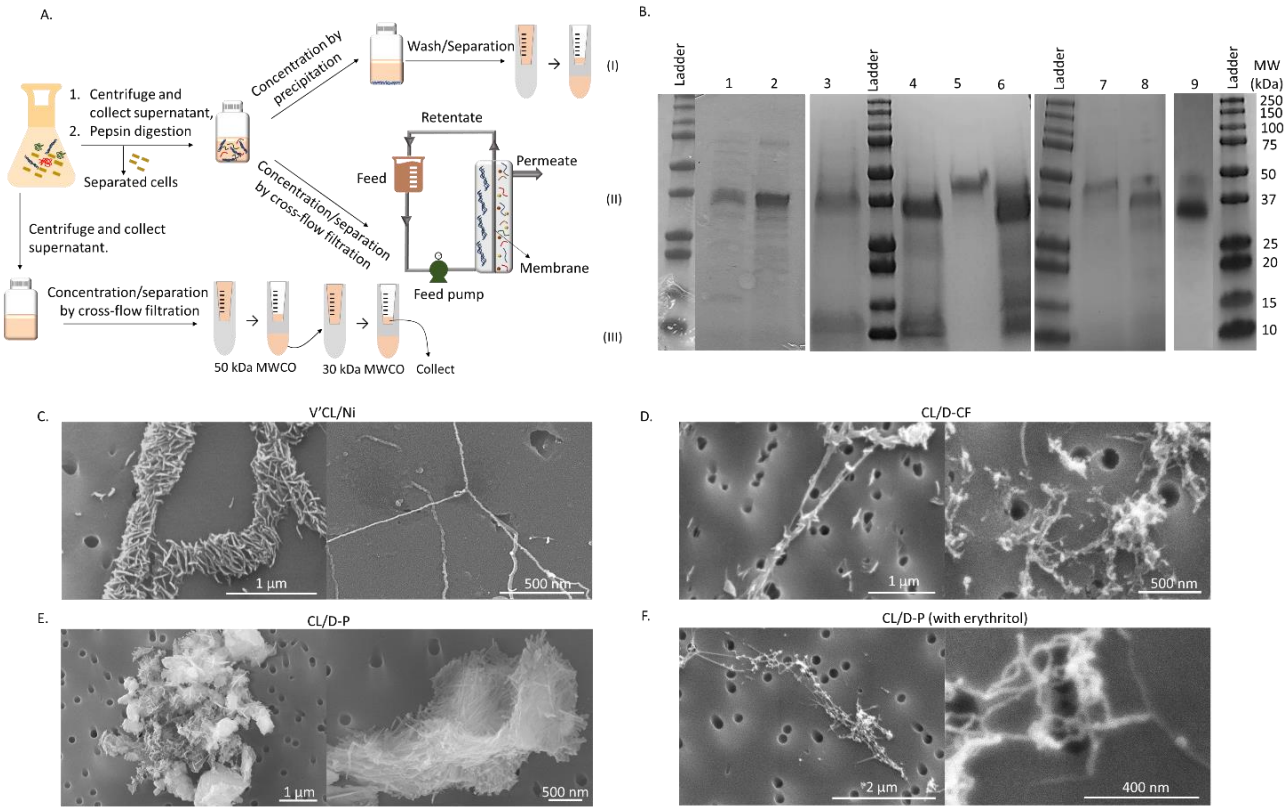

Figure 4. 2. Purification of extracellular collagen using scalable methods. (A) Scheme of two scalable purification methods: digestion/precipitation or (D-P, top) and digestion/cross-flow filtration (D-CF, bottom). After the filtration, the collagen domain (CL) will be trapped in the retentate and the digested variable domain (V') and other small digested proteins will be removed through permeate. The supernatant is first separated from bacterial cells via centrifugation and digested with pepsin. It is then subjected to separation via precipitation or filtration. (B) SDS-PAGE analysis of the purified collagen samples showed comparable purity with collagen/Ni and no fragmentation during the purification; supernatant of the bacterial culture expressed in PQN4 and BL21d (1 and 2), pepsin digested supernatant (3) CL/D-P (4), V'CL/Ni (5), CL/D-CF (6), V'CL/CF (7) CL/D-P and CL/D-CF and (washed with 30 kDa centrifugal filters to remove the remaining impurities) (8 and 9). (C-F) Morphology of the purified proteins observed by SEM; (C) Purified collagen by chromatography (V'CL/Ni) showing the nano/micro-sized fibers, (D) CL/D-CF kept its integrity and fibrillar structure after purification, (E) The aggregated structure of the collagen obtained from D-P method, (F) the collagen obtained from D-P method and protected by erythritol, showing an intact fibrillar structure comparable with V'CL/Ni.

Lastly, we compared the morphology of collagen isolated with the three purification methods via SEM (Figure 4. 2 (C-F)). V'CL/Ni samples showed nano-sized and micro-sized assembled fibrils (Figure 4. 2C). In some sections of the sample, we could also recognize collagen molecules that

formed highly ordered networks with pore structures. For samples obtained via cross-flow filtration, we could still distinguish fibrillar structures and a meshwork of fibers (Figure 4. 2D). However, when using the precipitation method, the fibrillar structure of the collagen appeared to have been affected by the acid treatment (Figure 4. 2E). It has been found that the ideal pH value for the formation of native type fibrils is in the pH range of 5.0 to 8.5. The interaction of PTA with collagen molecules can rupture hydrogen bonds and electrostatic interactions throughout the collagen fibrils, therefore disordering its fibrillar structure. [127] However, when adding erythritol as protecting agent during precipitation, the collagen structure was preserved by erythritol against low pH (Figure 4. 2F). Indeed, the presence of polyols can preserve the electrostatic interactions that are important for the fibrillogenesis of the collagen. Polyols strengthen the bridge interactions between polypeptide chains and replace the water molecules, thereby preserving hydrogen bonds in the backbone of the collagen. [128] The preservation of the highly ordered fibrillar structure of collagen after purification is crucial in employing the final bacterial collagen product to design functional biomaterials. The biomimetic triple helical fiber meshwork with porous structure obtained from isolated bacterial collagen makes this material a proper candidate for restorative biomaterials and tissue engineering applications, where cell integration and diffusion of nutrients are key parameters.[129]

Structural organization of bacterial collagen proteins

Bacterial collagen triple helix formation and stability are mainly dependent on the electrostatic interactions between the charged amino acids, interactions of the polar residues between several GQN repeats, and the ordered hydration network involved in the numerous polar and charged residues in this domain.[15] In bacterial collagen, 30% of the amino acids in the collagen domain are charged residues, which is 2-times more than the content of charged residues in type I animal

collagen. Near the C-terminal end of bacterial collagen, a domain contains three full repeats of sequence GKD-GKD-GQN-GKD-GLP and several partial repeats of this sequence (Figure 4. 3A, red portion).[15] The effect of charged residues, such as lysine (K) and aspartate (D), on the formation and stabilization of triple helix has been previously studied in collagen-like peptides. [116, 130, 131] Due to the formation of salt-bridged hydrogen bonds by K-D charge-pairs, these residues are sufficient to form a stable triple helix. [116] In addition to the remarkable role of K-D charge-pairs at the C-terminal, there is a noticeable number of glutamate (E) and arginine (R) residues at the N-terminal of the collagen domain (Figure 4. 3A, blue portion). Investigations in synthetic peptides have demonstrated that relatively stable triple helixes can be produced when these residues are found in the X and Y positions of the triplet, respectively.[78] Therefore, the R-E pairs at the N-terminal of the collagen can favorably interact via electrostatic attractions and strengthen the triple helix formation throughout the collagen molecules. In a model suggested by Sarkar et al., [130] it has been shown that a stable triple helix can be formed by the K-D charge-pairs when the positively charged residue (K) at position X of the leading strand is paired with the negatively charged residue (D) at position Y of the middle strand, one triplet displaced toward the C-terminus. Similarly, the middle strand can interact with the lagging strand and the lagging strand can couple with the leading strand. Figure 3B (top) shows the final assembled triple helix directed by K-D and R-E that forms a "blunt-end" triple helix. [130, 132]

Another possible interaction that could result in a different arrangement between the collagen molecules is the interaction between K and R (N-terminal end of one molecule with C-terminal end of another molecule). Hulgan et al.,[133] reported a faster formation of an isopeptide bond between K and E compared with K-D pairs during self-assembly of the collagen mimetic peptides. Therefore, this potential electrostatic interaction can also direct the triple helix self-assembly, and

eventually result in a “sticky-end” arrangement, another model suggested by Leary et al, (Figure 4. 3B, bottom). [130, 132] The possible sticky-end model in triple helix formation of the collagen can result in the creation of overhangs that extend the length of the triple helix. Theoretically, a single molecule of bacterial collagen is around 60 nm in length, which is 5 times shorter than type I animal collagen. The suggested sticky-end arrangement for the bacterial collagen can result in indefinite triple helical elongation.

We verified this hypothesis using AFM and observed that the length of collagen can attain a wide range of values from 100 nm to 500 nm that appeared to be around 45 nm thick, possibly as a result of triple helical elongation as well as lateral packing of the collagen molecules Figure 4. 3C). However, a range of longer fibrils that bundled together also appeared on the SEM images. Furthermore, the extension can drive the fiber growth more extensively and form long uniform fibers, as we observed by staining purified collagen fibers with Sirius Red (Figure 3D). Upon Sirius Red staining, the bacterial collagen samples (V’CL/Ni, V’CL/CF, CL/D-CF, CL/D-P (erythritol)) appeared orange-red under the polarized light, similar to animal collagen, indicating the presence of triple helical structure. The presence of a stained collagen bundle of 80 µm in length and 3 µm in width confirms that the collagen molecules are capable of elongating and bundling into a population of nanofibers with triple helical packing similar to that of type I animal collagen. As expected, animal collagen appeared as larger bundles compared with bacterial collagen, which is likely due to the larger size of the animal collagen molecule (~ 1000 amino acids) compared with bacterial collagen (~200 amino acids). Consistent with the SEM images, integrated fiber-like structures were observed for the purified collagen samples. The collagen samples purified with the filtration method (V’CL/CF and CL/D-CF) both showed fine aligned fibers bound with Sirius Red, which indicated no adverse effect of pepsin digestion on the integrity

of the collagen (Figure 4. 3D). However, acid-precipitated collagen (CL/D-P) showed no birefringence under the polarized light, likely due to the denaturation of the collagen structure during acid treatment. However, upon protection by erythritol, the collagen apparently preserved its fibrillar structure and we observed red bundles indicating the presence of triple helix.

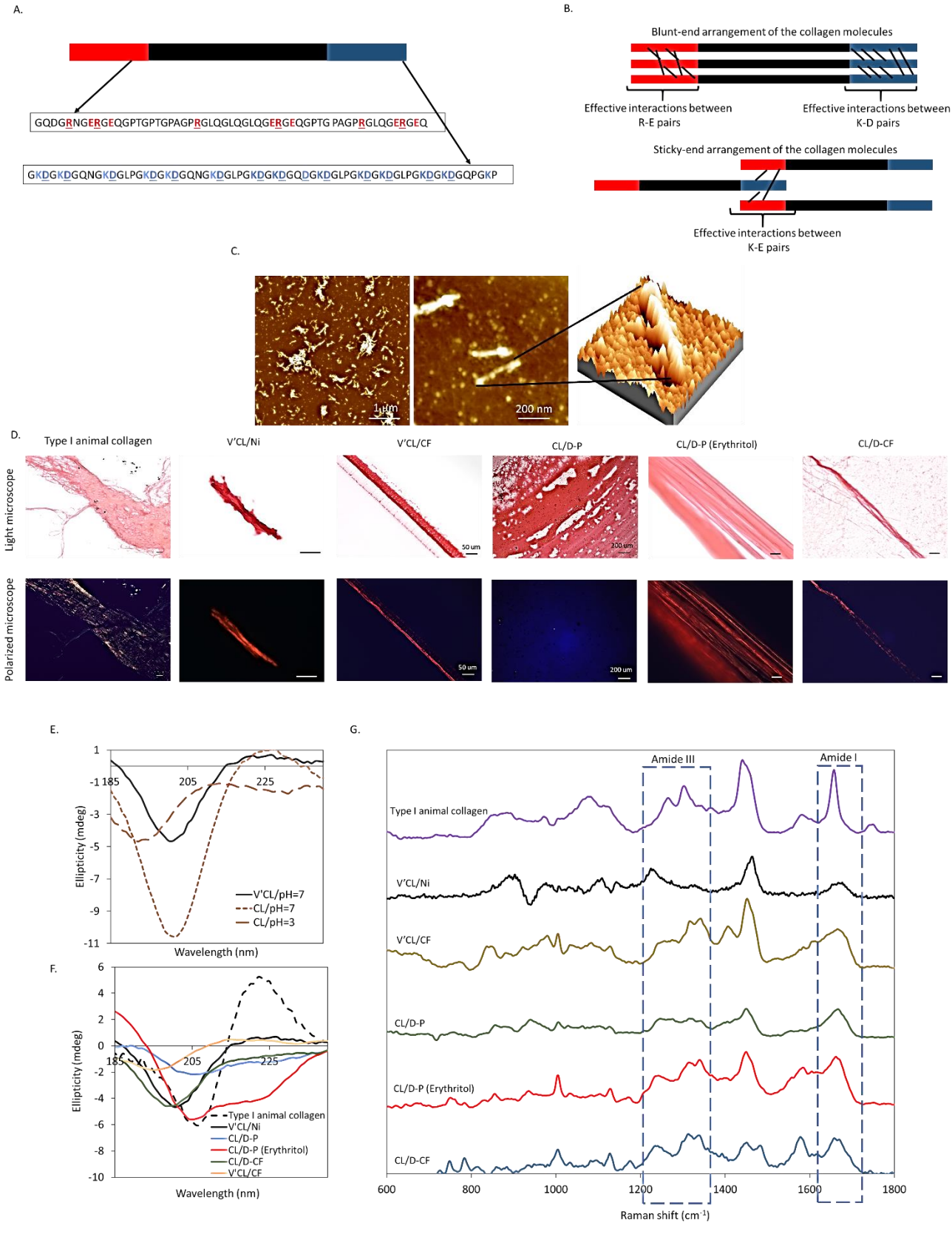
A.
GQDGRNGERGEQGPTGPTGPAGPRGLQGLQGLQGERGEQGPTG PAGPRGLQGERGEQ
GKDGKDGQNGKDGLPGKDGKDGQNGKDGLPGKDGKDGQDGKDGLPGKDGKDGLPGKDGKDGQPGKP
B.
Blunt-end arrangement of the collagen molecules
Effective interactions between R-E pairs
Effective interactions between K-D pairs
Sticky-end arrangement of the collagen molecules
Effective interactions between K-E pairs
C.
1 μm
200 nm
D.
Type I animal collagen
V'CL/Ni
V'CL/CF
CL/D-P
CL/D-P (Erythritol)
CL/D-CF
Light microscope
Polarized microscope
50 um
200 um
E.
Ellipticity (mdeg)
Wavelength (nm)
V'CL/pH=7
CL/pH=7
CL/pH=3
F.
Ellipticity (mdeg)
Wavelength (nm)
Type I animal collagen
V'CL/Ni
CL/D-P
CL/D-P (Erythritol)
CL/D-CF
V'CL/CF
G.
Amide III
Amide I
Type I animal collagen
V'CL/Ni
V'CL/CF
CL/D-P
CL/D-P (Erythritol)
CL/D-CF
Raman shift (cm-1)

Figure 4. 3. Structure and triple helix formation of bacterial collagen. (A) Scheme showing the collagen domain containing many charged residues such as E-R and K-D at the N- and C-terminal ends, respectively. (B) Schemes showing the blunt-end (top) and sticky-end (bottom) arrangement of the collagen molecules as a result of interactions between the charged amino acid. (C) The individual extended collagen fibers were observed with AFM. One side of the square is 400 nm long. (D) The purified collagen samples and type I animal collagen strongly bound with Sirius-Red and appeared red under the polarized light, indicating the formation of the triple helix (Unlabeled scale bars: 20 µm). (E) The low pH decreased the ellipticity value at 220 nm, and therefore affected the stability of the collagen domain. (F) CD spectra was used to study the secondary structure of the bacterial collagen purified with different methods. (G) Raman spectra of the purified collagen highlighting the amide I and amide III bands.

In addition to Sirius Red staining, we studied the formation of triple helical protein secondary structures in bacterial collagen after expression and purification using circular dichroism (CD) spectroscopy (Figure 4. 3E, F). The CD spectra of the V'CL/Ni at pH=7 showed a maximum value near 220 nm and a minimum near 200 nm (Figure 4. 3E). The positions of the maximum and minimum peaks demonstrate the characteristic spectrum of triple helical collagen similar to type I animal collagen, but with lower peak magnitudes. We also note that the CD spectrum of the V'CL showed a lower ellipticity at 220 compared with the isolated collagenous domain (CL), due to the presence of the helical non-collagenous domain (V') in the V'CL sample (Figure 4. 3E).[15]

We also evaluated the secondary structure of the collagen samples purified from scalable methods (Figure 4. 3F). The most similar spectrum to V'CL/Ni was the spectrum of the V'CL/CF, the sample purified by cross-flow filtration (50 kDa and 30 kDa) of the supernatant, without any treatment. V'CL/CF showed a positive ellipticity value at around 220 nm and a negative value at around 190 nm. Lower ellipticity value in this sample compared with V'CL/Ni was probably due to the presence of the impurities (purity 70% according to the SDS-PAGE result (Figure 4. 2B). The shape of the spectrum for CL/D-CF was similar to V'CL/Ni, but with a lower ellipticity value

at 220 nm, which could be due to a slight dissociation of the collagen molecules, potentially caused by the low pH necessary for the activity of the pepsin enzyme used in the digestion step (which precedes cross-flow filtration and precipitation purification, but not chromatography purification). We observed more pronounced differences in the CL/D-P spectrum. The positions and magnitude of the maximum and minimum peaks in the CL/D-P differed from V'CL/Ni. The pepsin and acid treatment likely caused the loss of triple helix structure and the emergence of a random coil (denatured) structure.[134] Also, since the V domain in these samples is susceptible to digestion, they are more prone to incomplete folding, as the V domain helps with self-association and folding of the CL domain.[135] However, protecting the collagen with erythritol resulted in a less pronounced collagen denaturation, but strikingly, in an increase in its alpha helical content based on distinct minima at around 205 and 220 nm.[136] These results are in accordance with the SEM images of the protected and non-protected CL/D-P collagen, which showed fibril-like structures for protected collagen. It is possible that the presence of erythritol molecules affected the assembly of the helical strands, and modified the collagen structure, from a triple helix dominated structure to an alpha-helical one; however, this requires further investigation.

To further investigate the role of the charged amino acid in the triple helix formation, we obtained the CD spectrum of the CL domain at pH=3 (Figure 4. 3E). To do so, we first isolated the CL domain via trypsin digestion. The ellipticity value significantly dropped at 220 nm when the resulting CL domain was exposed to acidic pH compared with pH=7. This reduction indicated that basic amino acids (aspartate and glutamate) play a significant role in triple helix formation for bacterial collagen and that their electrostatic interactions can be disrupted in acidic pH. We also studied the thermal unfolding curves of the purified samples at 198 nm between 5 °C and 50 °C (Figure S4. 5). As the temperature increased, type I animal collagen showed a significant change

in the ellipticity value, indicating the transition from triple helix at lower temperatures to random coil at higher temperatures (Figure S4. 5, A). The observed transition temperature (33 °C) was close to the previously reported melting temperature of type I animal collagen. [137] We also observed a similar transition in the V'CL/Ni sample. According to the thermal unfolding curve, the V'CL/Ni sample started unfolding at around 25 °C (Figure S4. 5, B). The lower transition temperature can be explained by the smaller size of bacterial collagen compared with animal collagen and by the presence of the non-collagenous domains (N22, TEE, His-tag, V domain). Similarly, the V'CL/CF showed a slight change in ellipticity value as temperature increased, and started unfolding at around 25 °C. However, the purified samples that were exposed to the pepsin digestion and acid treatment (CL/D-P, CL/DP (erythritol), CL/D-CF) showed no clear thermal transition, which is likely due to the partial denaturation and unfolding of these collagen samples during the purification processes (Figure S4. 5, C).

To further investigate chemical and conformational changes of the collagen samples after the purification processes, we obtained the Raman spectra of the collagen samples. Figure 4. 3G shows the Raman spectra of the purified collagen molecules in the range of 1800–600 cm^{-1}, along with some relevant biomarkers and characteristic bands for type I collagen. In all bacterial collagen samples, we observed a broad amide I band with a center typically around ~1670 cm^{-1}. The amide I band is largely influenced by the vibrations of the backbone carbonyls, and its position can provide information about the specific conformation of the proteins in the sample. In this case, the position at 1670 cm^{-1} is consistent with an extended conformation, such as would be observed in a triple helix, beta-turn, beta-sheet, or extended coil. [138, 139] The vibrations at around 920 and 855 cm^{-1} likely arise from vibrations in the proline ring, reflecting the high proline content in bacterial collagen.[140-142] The amide III Raman band for proteins is located between 1200 to 1350 cm^{-1} and

the positions of the maxima are also influenced by the specific protein's conformations present in the sample. For example, the amide III bands of collagen typically consist of two major maxima at 1271 cm^{-1} (assigned to nonpolar fragments with high proline content that form a typical collagen triple helix) and 1244 cm^{-1} (assigned to polar fragments of collagen characterized by low proline content) with lower intensity at wavenumbers above 1300 cm^{-1}.[84] In the V'CL/Ni sample, two peaks of the amide III region appeared at 1230 and 1270 cm^{-1}, as expected.[141] However, in most of the other samples, the amide III bands exhibited two maxima at around 1310 and 1340 cm^{-1}, which is typically associated with alpha helical structure.[143] On the other hand, the amide I band position at ~1670 cm^{-1} is inconsistent with alpha helical secondary structure, which is typically in the range of 1650-1655 cm^{-1}. [144] Thus, we are currently cautious not to overinterpret these spectra, with the implication that there may be a mixture of secondary structures in these particular samples, possibly owing to their different processing and purification methods utilized.

In summary, from the CD and Raman investigations, we conclude that the collagen obtained from Ni-NTA chromatography forms ordered triple helical structures and that the collagen purified via cross-flow filtration or acid precipitation is slightly more disordered, and in some cases may even contain alpha helical structure. The acidic processing steps (starting with pepsin digestion) may disrupt some of the interactions between collagen chains. It may be possible, however, to modify the purification processes to avoid compromising triple helix formation, by omitting the pepsin digestion step, and by protecting collagen against acids with erythritol.

Processing bacterial collagen

Finally, we wished to demonstrate that the secreted and purified collagen could be used to fabricate materials. To study the processability of the collagen samples, we formulated them into thin films and crosslinked hydrogels. First, freeze-dried collagen samples showed a sponge-like fibrous

structure that could mimic the fibrous structure of type I collagen (Figure 4. 4A). Next, we prepared free-standing thin films of ~0.2 mm thickness, by casting the collagen solution into the silicon molds (Figure 4. 4B). Such films could be potentially be applied to wound healing and tissue engineering problems.[145] Since collagen possesses high biodegradability and morphological plasticity, it is capable of rebuilding the microenvironment of the wounded tissues and achieving infiltration of a variety of cells, neovascularization, and extracellular matrix deposition. [146]

Although collagen holds valued biochemical properties such as resistance to protease degradation, it requires physical or chemical modifications to improve its stability especially for in vivo applications. Therefore, we then used genipin to crosslink the collagen samples. Genipin can react with the primary amine groups of the collagen and form the cyclic structures that act as fluorophores. To confirm the successful genipin crosslinking reaction, we measured the absorbance and fluorescence of the crosslinked collagen materials. In the presence of oxygen, genipin-bound amines turn blue, and their absorbance at ~ 590 nm increases (Figure S4. 3A). The genipin-modified collagen fluoresces at ~ 640 nm (Figure S4. 3). We observed increased absorbance and fluorescence intensities with increasing genipin to collagen ratio, also yielding more crosslink points. To further induce the gelation of the collagen, we used SDS, a low-molecular-weight surfactant. The rapid SDS-induced gelation of silk and curli proteins has been reported previously.[147, 148] Indeed, the presence of the SDS can provide hydrophobic interactions and intensify the electrostatic interactions between the charged residues of the collagen molecules and their negative charge.

To investigate the effect of the genipin crosslinking and SDS gelation on collagen viscosity, we measured the viscosity of the genipin and SDS treated samples under different shear rates (Figure 4. 4 C). Upon crosslinking, although strong chemical bonds between collagen molecules can be

formed, which strengthens the intramolecular and intermolecular interactions between collagen fibers, the viscosity of the sample did not change significantly. An important factor for injectability is to determine whether the hydrogel is shear-thinning. Shear-thinning hydrogels experience decreases in viscosity upon application of shear stress, which we observed in the SDS-induced gelated collagen (Figure 4. 4C). We also illustrate collagen gelation by presenting snapshots of manual injections of ginipin and SDS-treated collagen solutions into water (Figure 4. 4D). The genipin-treated collagen showed rapid dispersion immediately after injection, while the SDS-gelated collagen maintained its material integrity after injection.

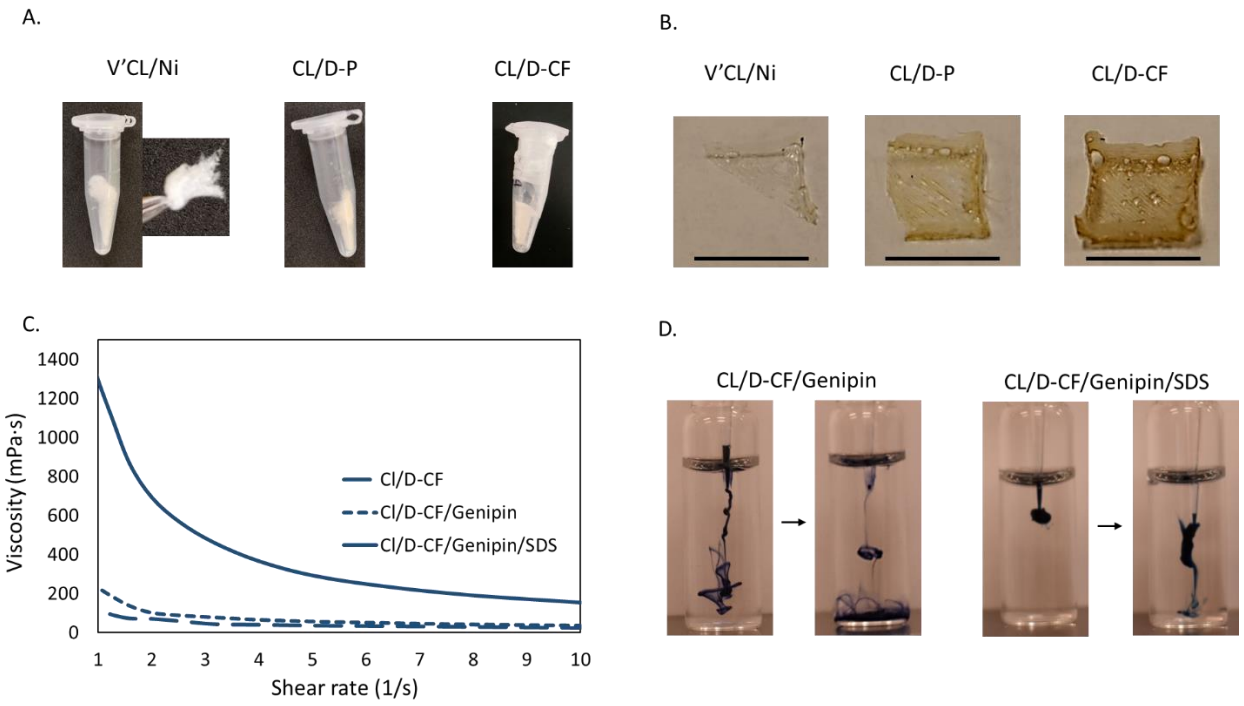

Figure 4. 4. Bacterial collagen processed in different forms. (A) Dried collagen samples after purification with different methods and lyophilization, (B) The thin free-standing collagen films. Scale bar: 1 cm. (C) viscosity of the genipin (5 mM) and SDS-treated collagen samples upon different shear rates indicating shear thinning behavior of the collagen gels. (D) Snapshots of manual injections of collagen cross-linked with genipin and gelated with SDS into water.

4.6. Conclusion

Depending on the purification and processing, recombinantly produced bacterial collagen can possess structural stability and conformation features (e.g., triple helix) comparable to type I animal collagen with emerging uses as biomaterials for a broad range of applications. Herein, inspiration from the extracellular secretion system for curli fibers allows us to engineer a simple secretion pathway for bacterial collagen in *E. coli* cells. Most importantly, the extracellular secretion prevented the need for cell rupture, and therefore, simplified the isolation of bacterial collagen. After simply centrifuging the bacterial culture, the crude supernatant itself exhibited a close to 50% collagen content. Then, using cost-effective and simple purification methods, we obtained more than 90% purity and around 0.4 g/L purification yield, in a fast and easy manner.

Analysis of the morphology and secondary structure of the collagen products indicated that the secreted and purified bacterial collagen formed fibrillar structures similar to type I animal collagen. While the structure of bacterial collagen differs slightly from type I collagen, as it is held together by pairs of charged residues, they share many structural and physicochemical characteristics. Under the right conditions, secreted bacterial collagen was able to form elongated triple helical structures of hundreds of nanometers in length, held together by electrostatic interactions. We also demonstrated that bacterial collagen can be processed as dried proteins, films, and cross-linked hydrogels, all of which can enable the utilization of collagen as the main component of functional biomaterials.

4.7. Supporting Information

Table S4. 1. The protein sequence of the bacterial collagen and DNA sequences of the genes involved for extracellular secretion of bacterial collagen.

The protein sequence of the variable domain (V)	DEQEEKAKVRTEFIQELAQGLGGIEKKNFPTLGDEDLDHTYMTKL LTYLQEREQAENSWRKRLLKGIQDHALDLVPRGSP
The protein sequence of bacterial collagen (CL)	GQDGRNGERGEQGPTGPTGPAGPRGLQGLQGLQGERGEQGPTGP AGPRGLQGERGEQGPTGLAGKAGEAGAKGETGPAGPQGPRGEQG PQGLPGKDGEAGAQGPAGPMGPAGERGEKGEPGTQGAKGDRGE TGPVGPRGERGEAGPAGKDGERGPVGPAGKDGQNGQDGLPGKD GKDGQNGKDGLPGKDGKDGQNGKDGLPGKDGKDGQDGKDGLP GKDGKDGLPGKDGKDGQPGKP
Forward primer (to remove *csgA*)	TCTGAGCTGAACATTTACCAGTACGG
Reverse primer (to remove *csgA*)	ATTTGGGCCGCTATTATTACCGCC
Forward primer (to remove *csgC*)	AATCTTCACGCCGTTGAGGTAGAA
Reverse primer (to remove c*sgC*)	GCGCCCTGTTTCTGTAATACAAA
Forward primer (to remove *csgF*)	CGTGCTCAGAGCTACAAAGATTTGACCC

Reverse primer (to remove *csgF*)	TGCAGCCTCCGAACAATTTTTTATTTAG
SEC	ATGAAACTTTTAAAAGTAGCAGCAATTGCAGCAATCGTATTCT CCGGTAGCGCTCTGGCA
N22	GGTGTTGTTCCTCAGTACGGCGGCGGCGGTAACCACGGTGGTG GCGGTAATAATAGCGGCCCAAAT
Translational enhancing element (TEE)	ATGAACCATAAGGTTCAC
csgC	ATGAATACGTTATTACTCCTTGCGGCACTTTCCAGTCAGATAAC CTTTAATACGACCCAGCAAGGGGATGTGTATACCATTATTCCTG AAGTCACTCTTACTCAATCTTGTCTGTGCAGAGTACAAATATTG TCCCTGCGCGAAGGCAGTTCAGGGCAAAGTCAGACGAAGCAA GAAAAGACCCTTTCATTGCCTGCTAATCAACCCATTGCTTTGAC GAAGTTGAGTTTAAATATTTCCCCGGACGATCGGGTGAAAATA GTTGTTACTGTTTCTGATGGACAGTCACTTCATTTATCACAACA ATGGCCGCCCTCTTCAGAAAAGTCTTAA
csgE	ATGAAACGTTAtttACGCTGGATTGTGGCGGCAGAATTTCTGTTC GCCGCAGGGAATCTTCACGCCGTTGAGGTAGAAGTCCCGGGAT TGCTAACTGACCATACTGTTTCATCTATTGGCCATGATTTTTAC CGAGCCTTTAGTGATAAATGGGAAAGTGACTATACGGGTAACT TAACGATTAATGAAAGGCCCAGTGCACGATGGGGAAGCTGGAT CACTATAACGGTCAATCAGGACGTTATTTTCCAGACTTTTTTAT

	TTCCGTTGAAAAGAGACTTCGAGAAAACTGTCGTCTTTGCACT GATTCAAACTGAAGAAGCACTAAATCGTCGCCAGATAAATCAG GCGTTATTAAGTACGGGCGATTTGGCGCATGATGAATTCTAA
csgF	ATGCGTGTCAAACATGCAGTAGTTCTACTCATGCTTATTTCGCC ATTAAGTTGGGCTGGAACCATGACTTTCCAGTTCCGTAATCCAA ACTTTGGTGGTAACCCAAATAATGGCGCTTTTTTATTAAATAGC GCTCAGGCCCAAAACTCTTATAAAGATCCGAGCTATAACGATG ACTTTGGTATTGAAACACCCTCAGCGTTAGATAACTTTACTCAG GCCATCCAGTCACAAATTTTAGGTGGGCTACTGTCGAATATTA ATACCGGTAAACCGGGCCGCATGGTGACCAACGATTATATTGT CGATATTGCCAACCGCGATGGTCAATTGCAGTTGAACGTGACA GATCGTAAAACCGGACAAACCTCGACCAtCCAGGTTTCGGGTTT ACAAAATAACTCAACCGATTTTTAA
csgG	ATGCAGCGCTTATTTCTTTTGGTTGCCGTCATGTTACTGAGCGG ATGCTTAACCGCCCCGCCTAAAGAAGCCGCCAGACCGACATTA ATGCCTCGTGCTCAGAGCTACAAAGATTTGACCCATCTGCCAG CGCCGACGGGTAAAATCTTTGTTTCGGTATACAACATTCAGGA CGAAACCGGGCAATTTAAACCCTACCCGGCAAGTAACTTCTCC ACTGCTGTTCCGCAAAGCGCCACGGCAATGCTGGTCACGGCAC TGAAAGATTCTCGCTGGTTTATACCGCTGGAGCGCCAGGGCTT ACAAAACCTGCTTAACGAGCGCAAGATTATTCGTGCGGCACAA GAAAACGGCACGGTTGCCATTAATAACCGAATCCCGCTGCAAT CTTTAACGGCGGCAAATATCATGGTTGAAGGTTCGATTATCGG

	TTATGAAAGCAACGTCAAATCTGGCGGGGTTGGGGCAAGATAT TTTGGCATCGGTGCCGACACGCAATACCAGCTCGATCAGATTG CCGTGAACCTGCGCGTCGTCAATGTGAGTACCGGCGAGATCCT TTCTTCGGTGAACACCAGTAAGACGATACTTTCCTATGAAGTTC AGGCCGGGGTTTTCCGCTTTATTGACTACCAGCGCTTGCTTGAA GGGGAAGTGGGTTACACCTCGAACGAACCTGTTATGCTGTGCC TGATGTCGGCTATCGAAACAGGGGTCATTTTCCTGATTAATGAT GGTATCGACCGTGGTCTGTGGGATTTGCAAAATAAAGCAGAAC GGCAGAATGACATTCTGGTGAAATACCGCCATATGTCGGTTCC ACCGGAATCCTGA

Table S4. 2. Abbreviation table.

CL	Collagen-like domain
V	Variable (non-helical) domain
V’	Variable domain + N22 + His-tag + translation enhancing element
V’CL/Ni	Collagen obtained from Ni-NTA
V’CL/CF	Collagen was obtained from filtration with 50 kDa and 30 kDa MWCO centrifugal filter.
CL/D-CF	Collagen obtained from pepsin digestion of supernatant followed by filtration with 30 kDa MWCO centrifugal filter.

CL/D-P	Collagen obtained from pepsin digestion of supernatant followed by acid precipitation.

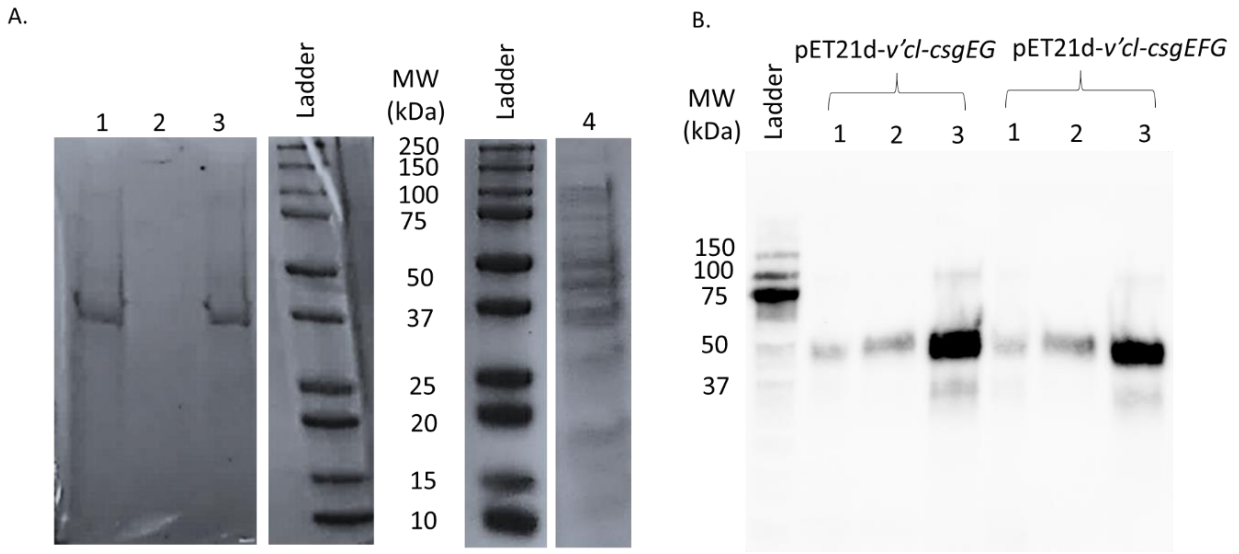

Figure S4. 1. (A) Distribution of proteins in culture (1), supernatant (2), and pellets (3) collected secreted by PQN4 transformed cells from pET21d-MBP vector and the culture collected from untransformed PQN4 cells (4). (B) Distribution of collagen in the pellet (lane 1), supernatant (lane 2), and bacterial culture (lane 3) corresponds to the modified vectors (pET21d-v'cl-csgEG and pET21d-v'cl-csgEFG).

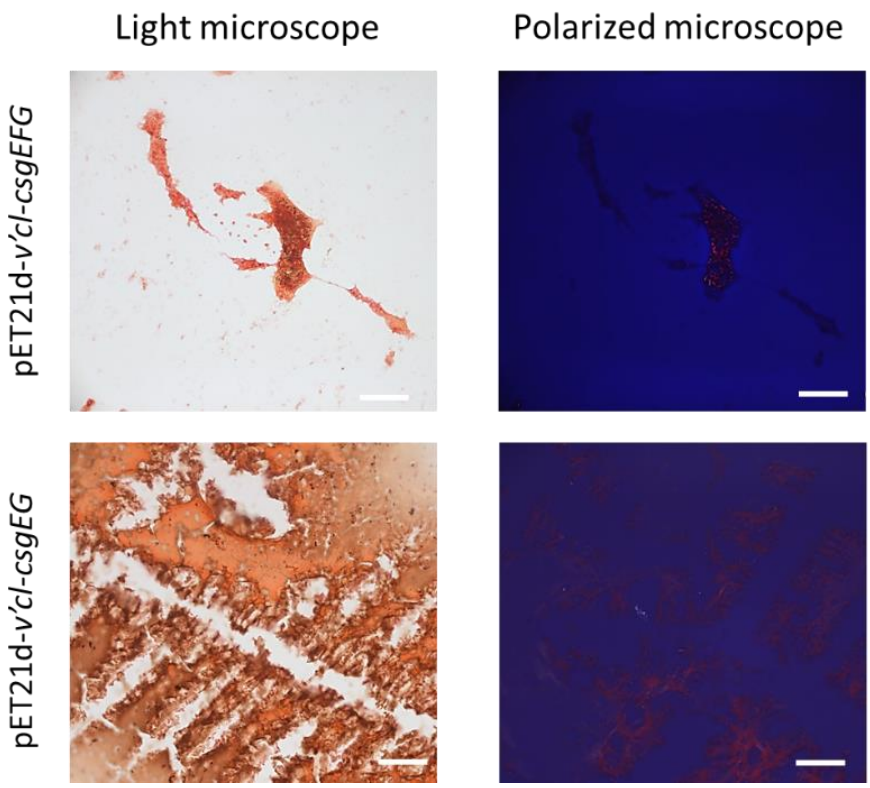

Figure S4. 2. Observation of secreted collagen using the modified vectors (pET21d-v'cl-csgEFG and pET21d-v'cl-csgEG.) Images of Sirius Red stained cultures are taken under a light microscope (left) and a polarized light microscope (right). Scale bars: 100 um.

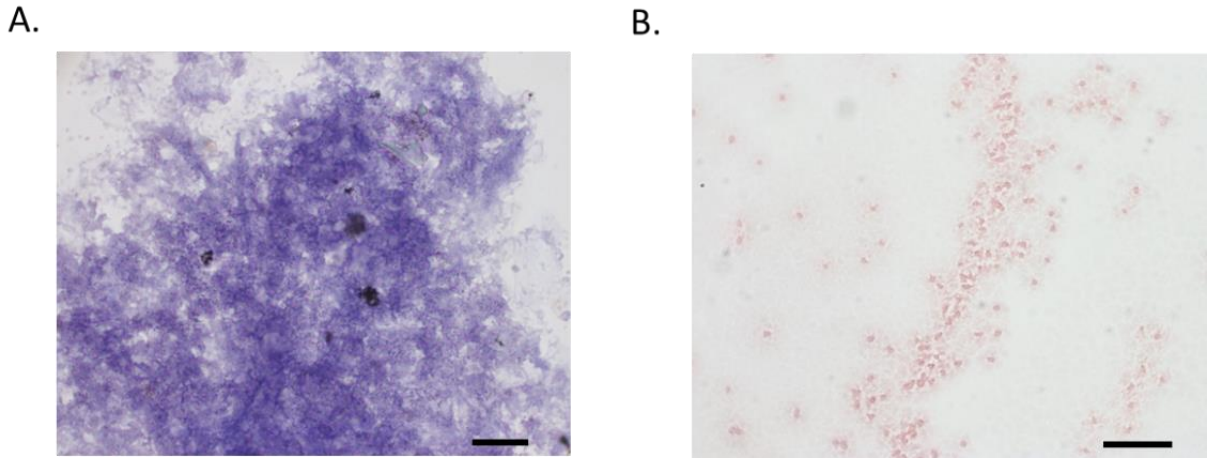

Figure S4. 3. Triple-helical structure of secreted collagen confirmed via Masson trichrome staining. Supernatant collected from collagen-secreting culture appeared blue (A) compared with untransformed PQN4 cell culture (B). Scale bars: 20 µm.

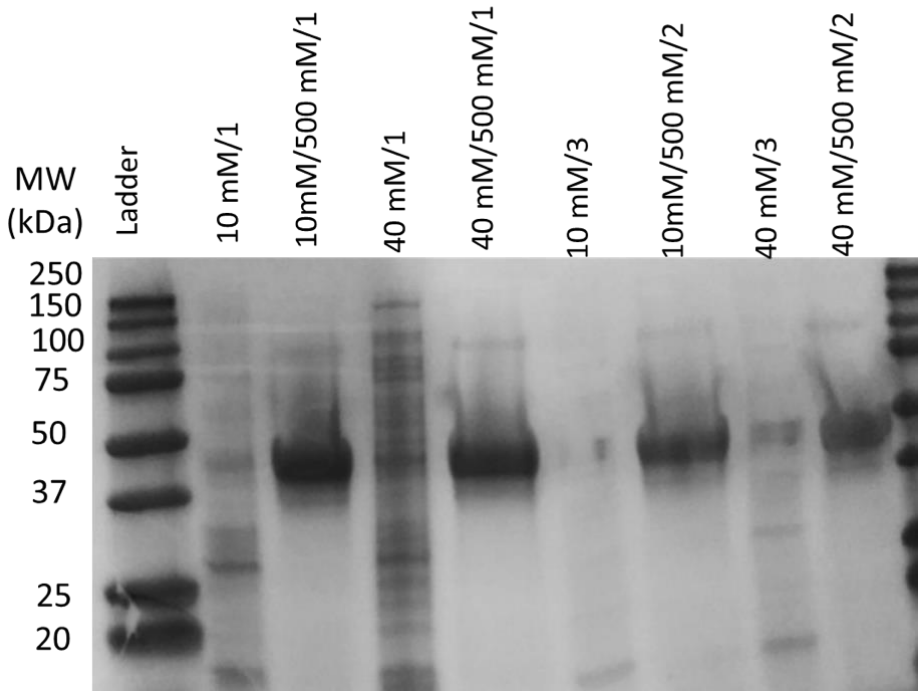

Figure S4. 4. Optimization of the Ni-NTA purification using 10 mM and 40 mM imidazole solutions for washing the non-specifically bound proteins and 500 mM imidazole for the elution step. The numbers stand for the number of the collected fractions.

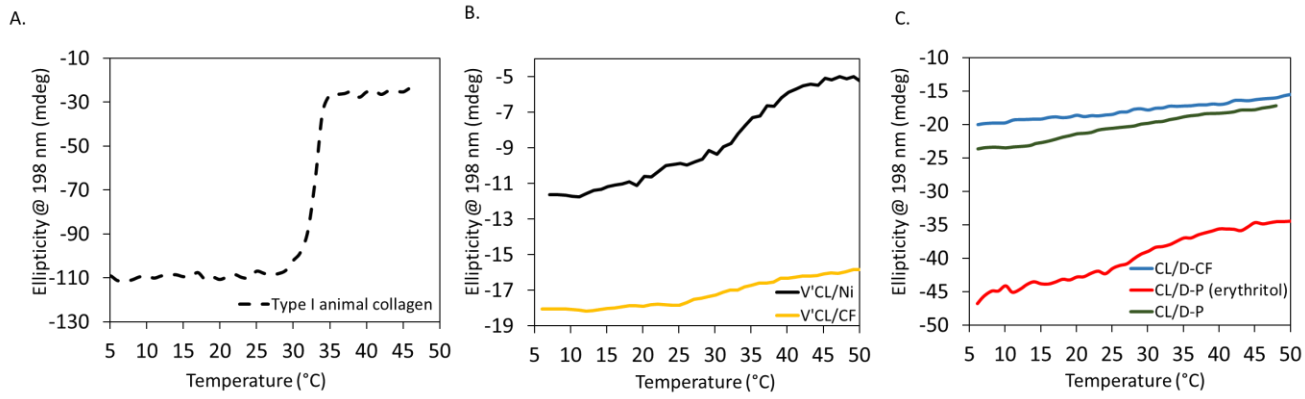

Figure S4. 5. (A-C) CD thermal transitions of the different purified collagen samples at 198 nm. Without pepsin digestion and acid treatment, collagen was able to fold properly, and show a transition during the thermal transition (B), however, it remained unfolded during these treatments (C).

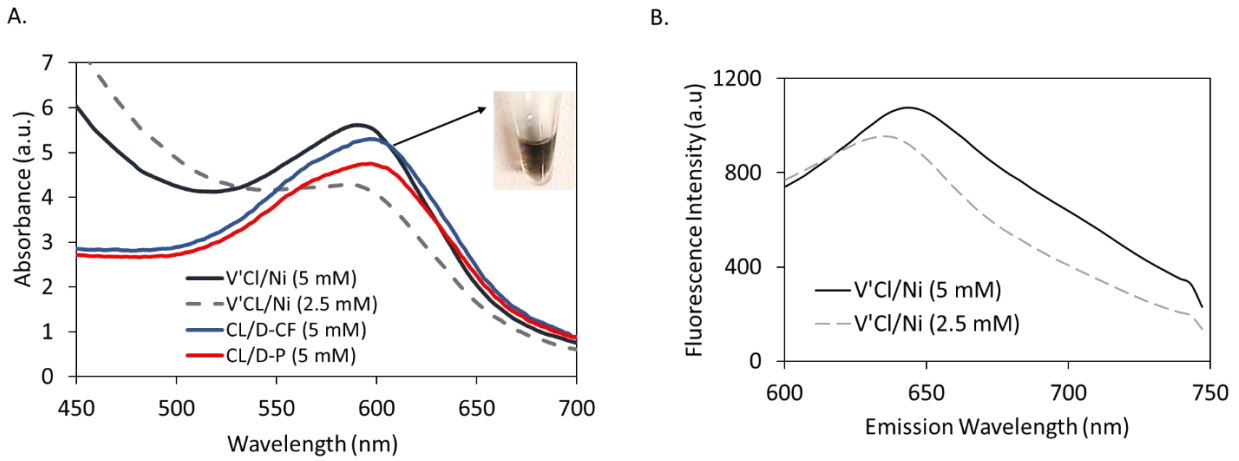

Figure S4. 6. (A) Purified collagen sample cross-linked with genipin with two concentrations (2.5 mM and 5 mM) showed absorbance at 600 nm. (B) Upon the excitation at 590 nm light, an emission maximum is at around 640 nm was observed.

4.8. Acknowledgment and funding sources

The authors thank the Facility for Electron Microscopy and Research (FEMR) at McGill for assistance with SEM, the McGill Chemistry Microscopy and Imaging Lab (MIlab) for providing AFM facility, Dr. Jason Young's lab at McGill (Department of Biochemistry) and Dr. Hanadi Sleiman at McGill (Department of Chemistry) for the use of their circular dichroism spectrometers. This research was funded, in part, by the Natural Sciences and Engineering Research Council of Canada (NSERC) through a Discovery grant (NSERC RGPIN-2017-04598), by the Fonds de Recherche du Québec - Nature et Technologies (FRQNT), and it was undertaken, thanks to the support by the Canadian Foundation for Innovation (project #37524). Z.A. is grateful for financial support via a McGill Engineering Doctoral Award (MEDA) and an FRQNT Doctoral Research Scholarship.

Chapter 5. Bacterial Collagen-Templated Synthesis and Assembly of Inorganic Particles

5.1. Rationale for Chapter 5

Collagen has been widely used as a scaffold to mineralize different inorganic particles. Using a biocompatible source of collagen which is easy to extract and be processed can affect the scalable manufacturing of biomaterials. Recombinant Streptococcal bacterial collagen has been used as an alternative for type I animal collagen, with no concern about their immunogenicity and biocompatibility. However, bacterial collagen molecule is smaller than animal collagen, thus has less tendency to self-associate. Therefore, bacterial collagen needs further modifications (physical/chemical/genetic) to modulate its processability (gelation, film formation, spinnability, etc.). This chapter highlights the use of bacterial collagen as a scaffold for nucleation of three different inorganic materials: hydroxyapatite crystals, silver nanoparticles, and silica particles. Abundance of charged residues in bacterial collagen is a key driving force to initiate the nucleation and growth of the inorganic particles. At the same time, by combining the inorganic particles with bacterial collagen, it can be formed in macroscopic hydrogel form (by silica gelation), which can broaden the applicability of bacterial collagen. New functionality such as antibacterial properties and improved mechanical properties were also introduced to bacterial collagen after mineralization, which provide more potential in the field of biomaterial and tissue engineering, especially bone regenerative scaffold.

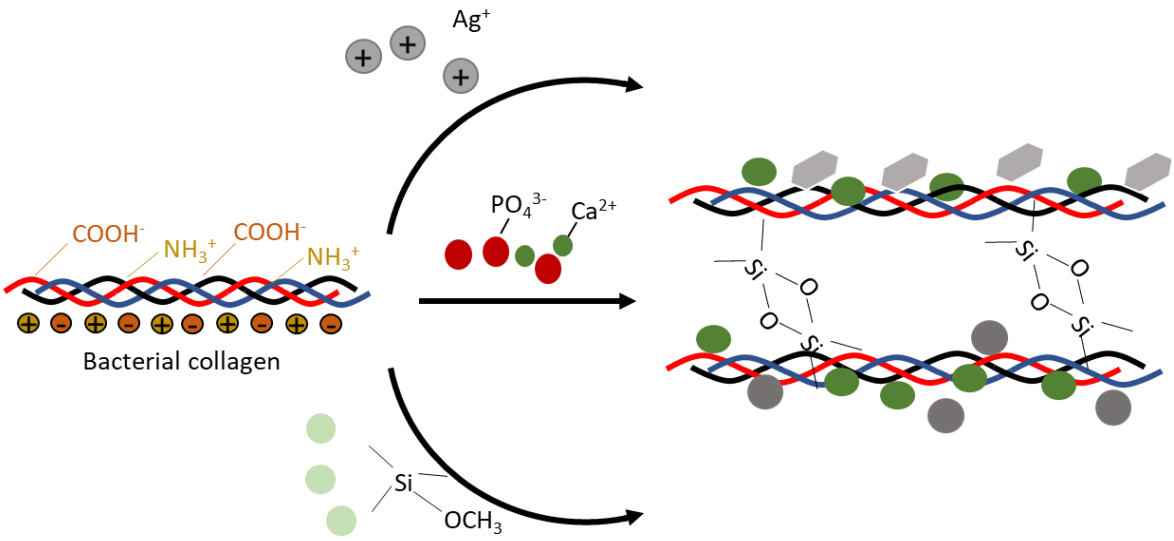

Chapter 5 is based on a manuscript in preparation, entitled "Bacterial Collagen-Templated Synthesis and Assembly of Inorganic Particles*"* and co-authored with Masoud Aminzare, Amy Chow, Noémie-Manuelle Dorval Courchesne.

5.2. Abstract

Collagen has been used as a common template for mineralization and assembly of inorganic particles, because of the special arrangement of its fibrils and the presence of charged residues. Streptococcal bacterial collagen, which is inherently secreted on the surface of *Streptococcus pyogenes*, has been progressively used as an alternative for type I animal collagen. Bacterial collagen is rich in charged amino acids, which can act as a substrate for the nucleation and growth of inorganic particles. Here, we show that bacterial collagen can be used to nucleate three different inorganic materials: hydroxyapatite crystals, silver nanoparticles, and silica particles. Collagen/mineral composites show an even distribution of inorganic particles along the collagen fibers, and the particles have a more homogenous size compared with minerals that are formed in

the absence of the collagen scaffold. Furthermore, the gelation of silica occurring during mineralization represents a means to produce processable self-standing collagen composites, which is challenging to achieve with bacterial collagen alone. Overall, we highlight the advantage of simply combining bacterial collagen with minerals to expand their applications in the fields of biomaterials and tissue engineering, especially for bone regenerative scaffolds.

Keywords: Bacterial collagen, mineralization, silver nanoparticle, hydroxyapatite, silica

5.3. Introduction

Collagen is an abundant protein with a variety of applications in the fields of biomaterials, tissue engineering, and drug delivery, due to its fascinating characteristics such as being biocompatible.[149] As a protein template, it has been combined with natural, synthetic, or inorganic materials to enhance its properties for tissue engineering, orthopedic, and dental applications.[150, 151] More specifically, type I collagen is known as the universal template for bio-inspired mineralization of the inorganic particles, such as hydroxyapatite, [152] calcium carbonate,[153] silica, [154] and metal nanoparticles. [155, 156]

To synthesize inorganic minerals, the use of proteins, particularly collagen, can help with nucleation, the orientation of mineral ions, growth and stabilization of the materials, as well as providing a structural framework for mechanical support.[56] The special arrangement of collagen fibrils and a high content of carboxylic groups make them proper templates for nucleation and growth of minerals such as hydroxyapatite. [64] They assemble in a parallel arrangement, in such a way to form a repeated 40 nm gap, called the “hole zone”, which is known to be a critical site for minerals nucleation. [64] In addition, the presence of the charged residues in the collagen can enhance

the colloidal stability of nanoparticles, such as silver, during the nucleation and growth stages. [49, 67]

The broad application of animal collagen in the field of biomaterials and tissues engineering has motivated investigations for alternative sources of collagen with lower immunogenicity and inflammatory response compared to animal sources, [113] such as recombinant collagen-like proteins. [22, 157] For instance, bacterial collagen-like proteins such as *Scl2,* inherently are expressed on the surface of *Streptococcus pyogenes,* have been recombinantly produced in *Escherichia coli (E. coli)*. These proteins are non-cytotoxic and non-immunogenic. They have a stable triple helical structure, with mechanical and thermal stability similar to type I animal collagen,[22, 158] with the exception that they lack hydroxyproline, the main amino acid contributing to the stabilization of the triple helix in animal collagen. Instead, the stability of bacterial collagen is a result of its high content of proline and charged amino acids, which participate in electrostatic interactions and support interchain hydrogen bonding. [158, 159]

Previously, we reported the extracellular secretion of bacterial collagen through a modified curli secretion pathway in *E. coli* and we simplified the purification methods for scalable isolation of bacterial collagen and subsequent fabrication of recombinant collagen-based biomaterials. [160] Although bacterial collagen is structurally similar to animal collagen, it still requires further treatments, such as physical/chemical crosslinking [26] or genetic modification, [161] to modulate its mechanical properties and processability (e.g., spinnability, gelation, and injectability). [162] Alternatively, mineralization is an easy approach to improving the structural and mechanical properties of collagen scaffolds. [163] Since bacterial collagen contains several positively (lysine and arginine) and negatively (glutamate and aspartate) charged amino acids, we hypothesized that they could serve as a template for mineralization, by stabilizing precursor ions and providing nucleation

and growth sites. Therefore, in this study, we used this feature to nucleate three different inorganic components - silver nanoparticles, hydroxyapatite crystals, and silica particles - on a bacterial collagen substrate, and we characterized their structures and physicochemical properties. Due to their antibacterial properties, silver nanoparticles have been applied for biotechnology applications such as biomaterials coatings, [164] wound dressing, [165] and bone and dental composites. [166] The size and distribution of silver nanoparticles can affect their release profile and antibacterial properties, which can be controlled by their nucleation rate. Hydroxyapatite and silica are also minerals with unique properties, such as their biocompatibility, biodegradability, and mechanical strength, and have been combined with the proteins such as collagen. The use of collagen with these minerals has previously shown a synergistic osteoconductive effect. [152] The mineralization mechanisms of these three minerals proceed via different steps, and we show that collagen is a suitable substrate for all three of them. We believe that the mineralization of bacterial collagen is a new route toward its application in the fields of biomaterials and tissue engineering by improving its processability and mechanical properties.

5.4. Materials and Methods

Expression and purification of bacterial collagen. Previously, we reported an adapted secretion pathway, used natively by *E. coli* to secrete curli fibers, for extracellular secretion of bacterial collagen (V'CL), which consists of the N-terminal variable domain plus N22, secretion signal peptide, (V'), and a collagen domain (CL). [160] We transformed the engineered plasmid (pET21d-*v'cl-csgCEFG*), containing the genes coding for V'Cl, CsgC, CsgE, CsgF, and CsgG, into *E. coli* PQN4 (a curli operon deletion mutant strain) for expression of bacterial collagen as the sole extracellular product. We then used a filtration-based purification method to isolate the extracellularly secreted collagen, as previously described. [160] Briefly, we digested the non-collagen

impurities in the supernatant of the bacterial culture using pepsin and concentrated and isolated the bacterial collagen using the crossflow filtration.

Synthesis and characterization of collagen-templated silver nanoparticles (CL/AgNp). We added 100 uL of bacterial collagen solution (at different concentrations: 0 mg/ml (No CL/AgNp), 0.5 mg/ml (CL0.5X/AgNp), 1 mg/ml (CL1X/AgNp), and 4 mg/ml (CL4X/AgNp) in water) to 100 uL of 30 mM $AgNO_3$ (BioShop Life Science Products) and agitated at 500 rpm at room temperature for 10 min. We added sodium citrate (BioShop Life Science Products) as a reducing agent, and coumalic acid (Sigma-Aldrich) as a capping agent, [167] to the collagen/$AgNO_3$ mixture, with final concentrations of 27.6 mg/ml and 2.18 mg/ml, respectively. The mixtures were agitated at 37°C and 60 °C for 4 hours. To remove excess salts and reagents, we centrifuged samples for 2 min at 13,000 rpm and washed them with water (3 times). We obtained the UV spectra of the prepared samples in the range of 350 – 650 nm by ultraviolet-visible (UV-Vis) absorption using a NanoDrop™ One Microvolume Spectrophotometer.

Using scanning electron microscopy (SEM), we studied the morphology and size of the particles and their interaction with the collagen fibers. We prepared the samples by depositing 50 µl of the CL/AgNp solution on 0.2 µm polycarbonate filter membranes (Whatman ® Nuclepore from Millipore Sigma). We washed the membranes with 0.1 M sodium cacodylate buffer (Electron Microscopy Sciences), fixed with 2% (v/v) glutaraldehyde (BioBasic) and 2% (v/v) paraformaldehyde (Electron Microscopy Sciences) for 2 h at room temperature, solvent-exchanged sequentially in 0%, 25%, 50%, 75% and 100% (v/v) ethanol (for 15 min in each solvent), and dried the membranes in a critical point dryer (CPD). We sputtered until they were coated with a 5 nm layer of Pt. We performed the imaging using FEI Quanta 450 ESEM at 5 kV equipped with an EDS detector.

We examined the antibacterial properties of the CL/AgNps mixture against *Escherichia coli* K12 ER2738 (Gram-negative) by monitoring the optical density of the bacteria at 600 nm (OD_{600}). To evaluate the effect of the CL/AgNp on the optical density of *E. coli*, we prepared exponentially growing bacterial suspensions by inoculating a single colony in 5 mL lysogeny broth (LB), growing overnight, diluting 1:250 in LB, and incubating at 37 °C to reach OD_{600} of 0.6. We treated 1 mL of the *E. coli* suspension with 10 µL of the CL/AgNp solutions, incubated at 37 °C, and measured the OD_{600} after 1h, 2h, and 18h. We defined 100% viability for bacteria grown in the absence of CL/AgNp samples. In addition, using the colony counting method, we examined the antibacterial properties of the CL/AgNp samples. To do so, we prepared the bacterial logarithmic-phase culture by suspending a single colony in 5 mL LB and incubating at 37 °C to reach OD_{600} of 0.6, then diluting 100 times (1 x 10^6 cfu/mL) and resuspending 15 µl of the diluted suspension into 45 mL LB. After overnight incubation at 37 °C, the concentration of bacteria went up to 10^8 CFU/mL and we diluted it to a working concentration of 10^6 CFU/mL. We added 10 µl of CL/AgNp solutions to 1 mL of the inoculum and incubated for 20, 40, and 60 min, 120 min at 37 °C. At the predetermined contact times, we removed 90 µl of the suspension, diluted it serially with PBS (10^1, 10^2, 10^3, 10^4, 10^5, and 10^6), and spread 5 µl of each of the diluted suspension onto four zones of an LB agar plate and incubated at 37 °C for 18 h. We used a collagen solution (4 mg/mL) and a bacterial suspension only as controls.

Synthesis and characterization of collagen-templated hydroxyapatite nanoparticles (CL/HAP). To mineralize the collagen with hydroxyapatite (HAP), we dissolved lyophilized collagen (with a final concentration of 0 mg/mL (HAP only) 1 mg/mL (CL1X/HAP), and 4 mg/mL (CL1X/HAP) in the mixture of 100 µL of 100 mM $CaCl_2$ and 100 µL of 50 mM Na_2HPO_4 and incubated the mixtures overnight at 37 °C. We removed the excess salts by washing the samples

with water and centrifuging for 2 min at 13,000 rpm (3 times). After fixing and drying using the same protocols used for CL/AgNp samples we studied the morphology of the CL/HAP samples by SEM coupled with an EDS detector. We sputtered the samples until they were coated with a 5 nm layer of carbon. We also carried out X-ray diffraction (XRD) using Cu K_α radiation ($\lambda = 1.5418$ Å) on a diffractometer (Bruker D8 Discovery) and recorded the pattern from 20° to 60° with a step size of 0.02°.

Synthesis and characterization of collagen-templated silica (CL/Silica). To synthesize the collagen-templated silica nanoparticles, we carried out the reaction by hydrolyzing 100 µL TMOS (Sigma-Aldrich) containing 1 mL of a collagen solution (at 0 mg/mL (Silica only), 1 mg/mL (CL1X/Silica), and 4 mg/mL (CL4X/Silica) with 100 µL 50 mM Tris–HCl buffer, pH 6.8, while placed on ice, vortexed for 1 min, and then incubated the mixture at room temperature for 1 h. We rinsed the resulting gels by soaking them in ethanol 99% (5 min, 3 times) followed by a 5 min rinse in water.

We conducted characterization of the CL/Silica samples by SEM observation along with elemental analysis by EDS. To better observe the interaction of the collagen and silica particles through SEM, we dissolved 0.5 mg of the formed hydrogels in 100 µL water to obtain a less entangled network. FT-IR spectra of the lyophilized samples were collected in a transmission mode on an FTIR spectrometer (Spectrum II from Perkin Elmer) from 400 to 4000 cm^{-1} at a resolution of 2 cm^{-1}. We measured the water absorption of the samples by soaking the dried samples in water for 12 hours and measured the weight difference before and after absorbing water.

The hardness and elastic modulus of the composites was assessed using a Nanovea nanoindenter at room temperature. We cold-mounted the samples in epoxy resin and polished by a high-speed rotary polisher (Dremel tool) them before testing to decrease surface heterogeneity. A Berkovich

diamond indenter with an approach speed of 2.5 μm/min, contact load of 0.3 mN, maximum load of 3 mN, and a 10 s hold time at maximum load (to minimize thermal drift and creep effects) was used for all the measurements.

Synthesis and characterization of collagen/HAP/AgNp/silica composite. To fabricate the four-component composite based on bacterial collagen, we added 100 uL of TMOS to 1 mL of collagen solution (4 mg/mL) and thoroughly mixed it for about 2 min. Then, we added the 4 mg of the synthesized CL4X/AgNp composite (washed and dried) and 4 mg of the CL4X/HAP composite (washed and dried) to the collagen/TMOS mixture and vigorously stirred using a vortex mixer for about 2 min. We added 100 μL of 50 mM Tris–HCl buffer, pH 6.8 dropwise to the mixture while stirring.

We conducted characterization of the CL/HAP/AgNp/silica sample by elemental analysis using energy-dispersive X-ray spectroscopy (EDS). We sputtered the samples until they were coated with a 5 nm layer of carbon. We assessed the hardness and elastic modulus of the composites using a Nanovea nanoindenter at room temperature. We also examined the antibacterial properties of the CL/Silica/HAP/AgNp sample against *E. coli* K12 ER2738 using the zone of inhibition test. We spread the bacterial suspension (10^6 CFU/mL) over an agar plate using a sterile swab and incubated it overnight at 37°C in the presence of the CL/HAP/AgNp/silica sample and CL/HAP/silica as a control.

Statistical analysis. Statistical analyses were performed via IMB SPSS Statistics program. Comparison of obtained data for different samples was performed with One-Way ANOVA with Tukey posthoc test. The significance level was set at $p < 0.05$.

5.5. Results and Discussion

Mineralization of bacterial collagen with silver nanoparticles (AgNps)

We first used bacterial collagen as a template to synthesize silver nanoparticles, with a combination of a chemical reductant and temperature to drive the synthesis of the nanoparticles. To confirm the reduction of silver ions, we first obtained the UV–visible spectrum of the samples. A typical silver surface plasmon resonance at a wavelength of around 400 nm, due to the oscillations of free electrons on the AgNps surface AgNps, [168] confirmed the formation of AgNps (Figure 3. Bacterial collagen as a template for the synthesis of AgNps. (A) The scheme shows the interactions between the functional groups of the collagen and the silver ions as the driving force for the nucleation of silver nanoparticles. (B) UV-Visible spectra of the composites with different concentrations of collagen. Higher collagen content increased the reduction of silver ions and the formation of AgNps. (C) UV-Visible spectra of the composites at different temperatures. At higher reaction temperatures, the reduction rate of silver ions increases. (D) SEM images of composites in the presence and absence of collagen at different temperatures. In the absence of collagen AgNps, tended to aggregate and form larger particles. At both temperatures AgNps were uniformly distributed along the fibers, confirming the effect of collagen in controlling the reduction reaction. The scale bar is 500 nm. (E, F) EDS map and elemental analysis of silver and nitrogen. The CL4X/AgNp showed a strong elemental signal of silver and its uniform distribution throughout the composite. The scale bar is 500 nm. (G) OD600 of the E. coli in the presence of different formulations of composites. CL/AgNp samples showed slower bacterial reduction compared with the sample without collagen (ns: not statistically significant).

B, C). In this synthesis, sodium citrate serves both as a reducing agent and as a stabilizer for the colloidal particles. It was found that the reducing reaction with only sodium citrate at low temperature (room temperature and lower) takes a long (~1 week) and shows a wide size distribution of silver nanoparticles. [169] Thus, sodium citrate, as a reducing agent, is often used in a boiling solution or combined with other capping agents (such as coumalic acid in the present case). In the presence of sodium citrate and coumalic acid along with the temperature, we observed the reduction of $AgNO_3$ to Ag.

At pH values higher than the isoelectric point of bacterial collagen (~5.5), negatively charged residues serve as stabilizing substrates to cap the silver ions. We studied the effect of collagen concentration on the synthesis of AgNps. At higher concentrations of collagen, the intensity of the absorbance peak increased at both 37°C and 60°C (Figure 3. Bacterial collagen as a template for the synthesis of AgNps. (A) The scheme shows the interactions between the functional groups of the collagen and the silver ions as the driving force for the nucleation of silver nanoparticles. (B) UV-Visible spectra of the composites with different concentrations of collagen. Higher collagen content increased the reduction of silver ions and the formation of AgNps. (C) UV-Visible spectra of the composites at different temperatures. At higher reaction temperatures, the reduction rate of silver ions increases. (D) SEM images of composites in the presence and absence of collagen at different temperatures. In the absence of collagen AgNps, tended to aggregate and form larger particles. At both temperatures AgNps were uniformly distributed along the fibers, confirming the effect of collagen in controlling the reduction reaction. The scale bar is 500 nm. (E, F) EDS map and elemental analysis of silver and nitrogen. The CL4X/AgNp showed a strong elemental signal of silver and its uniform distribution throughout the composite. The scale bar is 500 nm. (G) OD600 of the E. coli in the presence of

different formulations of composites. CL/AgNp samples showed slower bacterial reduction compared with the sample without collagen (ns: not statistically significant).

B). The specific interactions between the functional groups of the collagen template and the silver ions could thus promote the formation of the nanoparticles (Figure 3. Bacterial collagen as a template for the synthesis of AgNps. (A) The scheme shows the interactions between the functional groups of the collagen and the silver ions as the driving force for the nucleation of silver nanoparticles. (B) UV-Visible spectra of the composites with different concentrations of collagen. Higher collagen content increased the reduction of silver ions and the formation of AgNps. (C) UV-Visible spectra of the composites at different temperatures. At higher reaction temperatures, the reduction rate of silver ions increases. (D) SEM images of composites in the presence and absence of collagen at different temperatures. In the absence of collagen AgNps, tended to aggregate and form larger particles. At both temperatures AgNps were uniformly distributed along the fibers, confirming the effect of collagen in controlling the reduction reaction. The scale bar is 500 nm. (E, F) EDS map and elemental analysis of silver and nitrogen. The CL4X/AgNp showed a strong elemental signal of silver and its uniform distribution throughout the composite. The scale bar is 500 nm. (G) OD600 of the E. coli in the presence of different formulations of composites. CL/AgNp samples showed slower bacterial reduction compared with the sample without collagen (ns: not statistically significant).

A).[170] The higher intensity of the absorption peak of the samples containing collagen compared with the No CL/AgNp sample indicates that the bacterial collagen has a synergic effect with sodium citrate on the reduction of the silver ions and formation of the AgNps (Figure 3. Bacterial collagen as a template for the synthesis of AgNps. (A) The scheme shows the interactions between the functional groups of the collagen and the silver ions as the driving force for the

nucleation of silver nanoparticles. (B) UV-Visible spectra of the composites with different concentrations of collagen. Higher collagen content increased the reduction of silver ions and the formation of AgNps. (C) UV-Visible spectra of the composites at different temperatures. At higher reaction temperatures, the reduction rate of silver ions increases. (D) SEM images of composites in the presence and absence of collagen at different temperatures. In the absence of collagen AgNps, tended to aggregate and form larger particles. At both temperatures AgNps were uniformly distributed along the fibers, confirming the effect of collagen in controlling the reduction reaction. The scale bar is 500 nm. (E, F) EDS map and elemental analysis of silver and nitrogen. The CL4X/AgNp showed a strong elemental signal of silver and its uniform distribution throughout the composite. The scale bar is 500 nm. (G) OD600 of the E. coli in the presence of different formulations of composites. CL/AgNp samples showed slower bacterial reduction compared with the sample without collagen (ns: not statistically significant).

B). In particular, due to the nanoscale dimensions of the collagen fibers, they can adjust the size of the inorganic particles during nucleation and they possess abundant binding sites which bind to metal ions. [171] As stated previously, bacterial collagen contains negatively charged moieties (aspartic acid and glutamic acid) which serve as capturing and nucleating sites for the silver ions before the reduction step.

We also studied the effect of the temperature on the formation of AgNps (Figure 3. Bacterial collagen as a template for the synthesis of AgNps. (A) The scheme shows the interactions between the functional groups of the collagen and the silver ions as the driving force for the nucleation of silver nanoparticles. (B) UV-Visible spectra of the composites with different concentrations of collagen. Higher collagen content increased the reduction of silver ions and the formation of AgNps. (C) UV-Visible spectra of the composites at different temperatures. At

higher reaction temperatures, the reduction rate of silver ions increases. (D) SEM images of composites in the presence and absence of collagen at different temperatures. In the absence of collagen AgNps, tended to aggregate and form larger particles. At both temperatures AgNps were uniformly distributed along the fibers, confirming the effect of collagen in controlling the reduction reaction. The scale bar is 500 nm. (E, F) EDS map and elemental analysis of silver and nitrogen. The CL4X/AgNp showed a strong elemental signal of silver and its uniform distribution throughout the composite. The scale bar is 500 nm. (G) OD600 of the E. coli in the presence of different formulations of composites. CL/AgNp samples showed slower bacterial reduction compared with the sample without collagen (ns: not statistically significant).

C). We obtained the UV- visible absorbance spectra of the samples after 4 hours of incubation at 37 °C and 60 °C. The AgNps prepared at 37 °C without collagen substrate showed a single peak at around 410 nm and the ones prepared at 60 °C showed a wider peak at around 425 nm with higher intensity (Figure 3. Bacterial collagen as a template for the synthesis of AgNps. (A) The scheme shows the interactions between the functional groups of the collagen and the silver ions as the driving force for the nucleation of silver nanoparticles. (B) UV-Visible spectra of the composites with different concentrations of collagen. Higher collagen content increased the reduction of silver ions and the formation of AgNps. (C) UV-Visible spectra of the composites at different temperatures. At higher reaction temperatures, the reduction rate of silver ions increases. (D) SEM images of composites in the presence and absence of collagen at different temperatures. In the absence of collagen AgNps, tended to aggregate and form larger particles. At both temperatures AgNps were uniformly distributed along the fibers, confirming the effect of collagen in controlling the reduction reaction. The scale bar is 500 nm. (E, F) EDS map and elemental analysis of silver and nitrogen. The CL4X/AgNp showed a strong elemental signal of

silver and its uniform distribution throughout the composite. The scale bar is 500 nm. (G) OD600 of the E. coli in the presence of different formulations of composites. CL/AgNp samples showed slower bacterial reduction compared with the sample without collagen (ns: not statistically significant).

C). At higher temperatures, the reducing activity of the sodium citrate acid increases and result in more nucleation sites for the formation of the AgNps, therefore, the peak corresponding to 60 °C showed higher intensity than 37 °C. In addition, Liu *et al*., [172] showed that, at sufficient concentrations of precursors, the growth rate of nanoparticles increases linearly with reaction temperature, thus, the particle size increases at higher temperatures. [169, 172, 173] The broader peaks corresponding to AgNps synthesized at 60 °C correlate with a large size of AgNps. The CL4X/AgNp sample also showed absorbance intensity at 60 °C compared with 37 °C. However, the width of the two peaks is comparable, with no distinct shift. Although the reaction at 60 °C is faster than 37 °C due to the higher activity of reducing agents (faster nucleation), the growth rate remains controlled by the presence of collagen.

We also studied the morphology of the silver-mineralized samples using SEM (Figure 3. Bacterial collagen as a template for the synthesis of AgNps. (A) The scheme shows the interactions between the functional groups of the collagen and the silver ions as the driving force for the nucleation of silver nanoparticles. (B) UV-Visible spectra of the composites with different concentrations of collagen. Higher collagen content increased the reduction of silver ions and the formation of AgNps. (C) UV-Visible spectra of the composites at different temperatures. At higher reaction temperatures, the reduction rate of silver ions increases. (D) SEM images of composites in the presence and absence of collagen at different temperatures. In the absence of collagen AgNps, tended to aggregate and form larger particles. At both

temperatures AgNps were uniformly distributed along the fibers, confirming the effect of collagen in controlling the reduction reaction. The scale bar is 500 nm. (E, F) EDS map and elemental analysis of silver and nitrogen. The CL4X/AgNp showed a strong elemental signal of silver and its uniform distribution throughout the composite. The scale bar is 500 nm. (G) OD600 of the E. coli in the presence of different formulations of composites. CL/AgNp samples showed slower bacterial reduction compared with the sample without collagen (ns: not statistically significant).

D). In the absence of the collagen, silver ions were reduced, but the reaction was less controlled and the obtained AgNps were more polydispersed, compared with the collagen-templated samples at both 37 °C and 60 °C. AgNps formed at 60 °C showed larger particle size (98 ± 30 nm) compared with the particles formed at 37 °C (45 ± 23 nm). The higher temperature increased the reaction rate and silver ions reduce faster with less control. In some areas, we observed aggregated silver structures after synthesis at 60 °C . However, the collagen templated AgNps showed uniformly distributed AgNps along the collagen fibers at both 37 °C and 60 °C. From the obtained SEM images, the particle size difference between these two samples is indistinguishable. This observation indicates that increasing the reaction temperature did not significantly affect the particle size, which can be due to the stabilizing effect of the collagen. At higher reaction temperatures, although the silver ions tend to reduce quickly, as we observed in UV-Visible absorbance spectra, the collagen molecules provide enough nucleating sites for them and consequently prevent aggregation and uncontrolled reduction. However, further investigation would be needed to study the average size and distribution of the nanoparticles. AgNp-based composites have been used for different applications from antibacterial to conductive biomaterials, which makes it useful to prepare them simply and effectively with controlled size and shape. [174]

The SEM results clearly showed the importance of collagen in modulating the morphology and size of the AgNps.

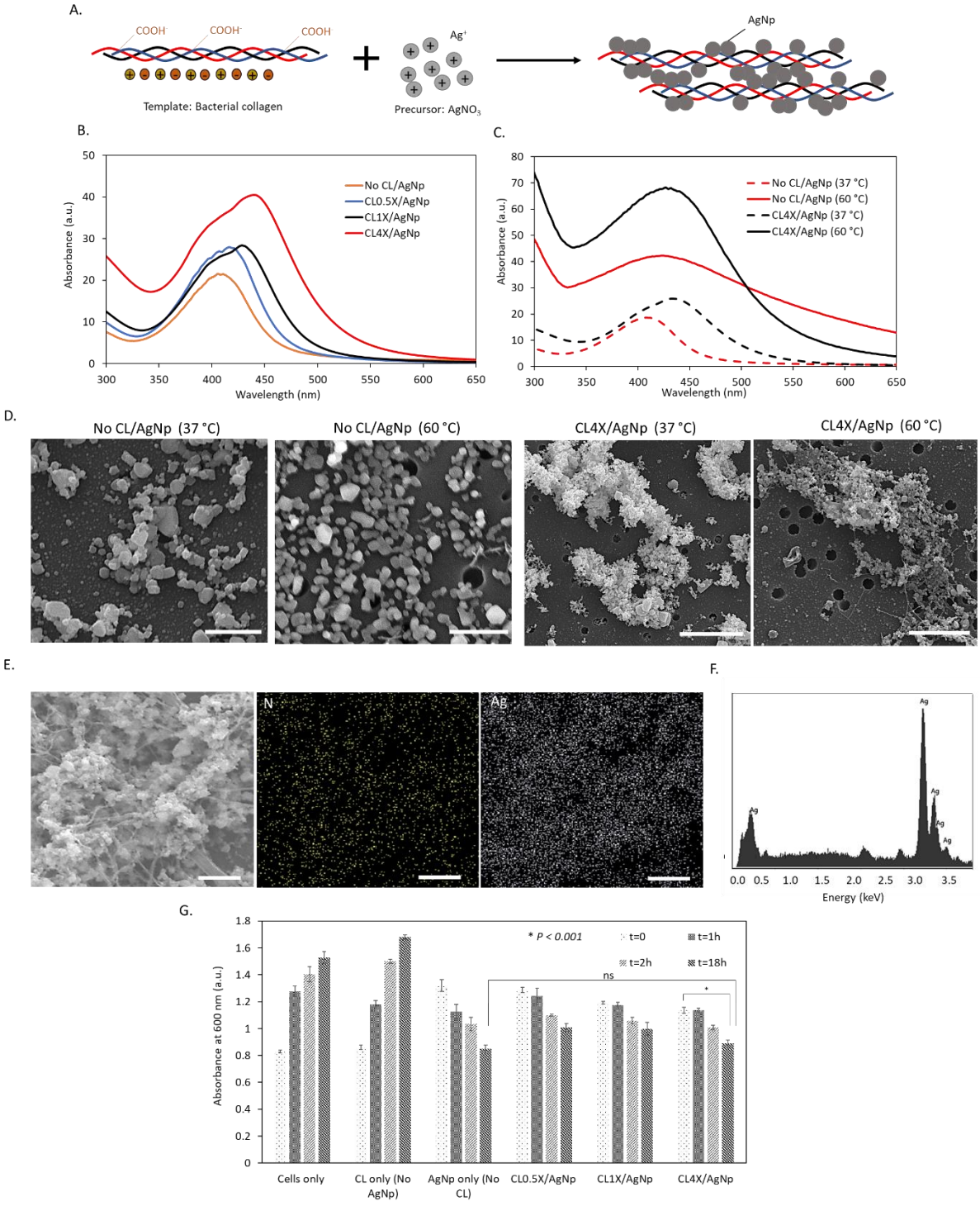

Figure 3. Bacterial collagen as a template for the synthesis of AgNps. (A) The scheme shows the interactions between the functional groups of the collagen and the silver ions as the driving force for the nucleation of silver nanoparticles. (B) UV-Visible spectra of the composites with different concentrations of collagen. Higher collagen content increased the reduction of silver ions and the formation of AgNps. (C) UV-Visible spectra of the composites at different temperatures. At higher reaction temperatures, the reduction rate of silver ions increases. (D) SEM images of composites in the presence and absence of collagen at different temperatures. In the absence of collagen AgNps, tended to aggregate and form larger particles. At both temperatures AgNps were uniformly distributed along the fibers, confirming the effect of collagen in controlling the reduction reaction. The scale bar is 500 nm. (E, F) EDS map and elemental analysis of silver and nitrogen. The CL4X/AgNp showed a strong elemental signal of silver and its uniform distribution throughout the composite. The scale bar is 500 nm. (G) OD600 of the E. coli in the presence of different formulations of composites. CL/AgNp samples showed slower bacterial reduction compared with the sample without collagen (ns: not statistically significant).

Among the silver mineralized samples, we chose the CL4/AgNp (37 °C) to study the distribution of the elements using EDS elemental analysis (Figure 3. Bacterial collagen as a template for the synthesis of AgNps. (A) The scheme shows the interactions between the functional groups of the collagen and the silver ions as the driving force for the nucleation of silver nanoparticles. (B) UV-Visible spectra of the composites with different concentrations of collagen. Higher collagen content increased the reduction of silver ions and the formation of AgNps. (C) UV-Visible spectra of the composites at different temperatures. At higher reaction temperatures, the reduction rate of silver ions increases. (D) SEM images of composites in the presence and absence of collagen at different temperatures. In the absence of collagen AgNps, tended to aggregate and form larger particles. At both temperatures AgNps were uniformly distributed along the fibers, confirming the effect of collagen in controlling the reduction reaction. The scale bar is 500 nm. (E, F) EDS map and elemental analysis of silver and nitrogen. The CL4X/AgNp showed a strong elemental signal of silver and its uniform distribution throughout the composite. The scale bar is 500 nm. (G) OD600 of the E. coli in the presence of different formulations of

composites. CL/AgNp samples showed slower bacterial reduction compared with the sample without collagen (ns: not statistically significant).

E, F). AgNps are known to display the binding energies of Ag between the ranges of 2.5-3.5 KeV which is due to their surface plasmon resonance.[175] We confirmed the presence of AgNps which displayed a strong signal of elemental silver around 3 keV with additional energy peaks in this range (Figure 3. Bacterial collagen as a template for the synthesis of AgNps. (A) The scheme shows the interactions between the functional groups of the collagen and the silver ions as the driving force for the nucleation of silver nanoparticles. (B) UV-Visible spectra of the composites with different concentrations of collagen. Higher collagen content increased the reduction of silver ions and the formation of AgNps. (C) UV-Visible spectra of the composites at different temperatures. At higher reaction temperatures, the reduction rate of silver ions increases. (D) SEM images of composites in the presence and absence of collagen at different temperatures. In the absence of collagen AgNps, tended to aggregate and form larger particles. At both temperatures AgNps were uniformly distributed along the fibers, confirming the effect of collagen in controlling the reduction reaction. The scale bar is 500 nm. (E, F) EDS map and elemental analysis of silver and nitrogen. The CL4X/AgNp showed a strong elemental signal of silver and its uniform distribution throughout the composite. The scale bar is 500 nm. (G) OD600 of the E. coli in the presence of different formulations of composites. CL/AgNp samples showed slower bacterial reduction compared with the sample without collagen (ns: not statistically significant).

F).[176, 177] The EDS elemental map obtained for the CL4X/AgNp (37 °C) sample showed the uniform distribution of the silver atoms consistent with the distribution of the nitrogen atoms throughout the composite (Figure 3. Bacterial collagen as a template for the synthesis of AgNps.

(A) The scheme shows the interactions between the functional groups of the collagen and the silver ions as the driving force for the nucleation of silver nanoparticles. (B) UV-Visible spectra of the composites with different concentrations of collagen. Higher collagen content increased the reduction of silver ions and the formation of AgNps. (C) UV-Visible spectra of the composites at different temperatures. At higher reaction temperatures, the reduction rate of silver ions increases. (D) SEM images of composites in the presence and absence of collagen at different temperatures. In the absence of collagen AgNps, tended to aggregate and form larger particles. At both temperatures AgNps were uniformly distributed along the fibers, confirming the effect of collagen in controlling the reduction reaction. The scale bar is 500 nm. (E, F) EDS map and elemental analysis of silver and nitrogen. The CL4X/AgNp showed a strong elemental signal of silver and its uniform distribution throughout the composite. The scale bar is 500 nm. (G) OD600 of the E. coli in the presence of different formulations of composites. CL/AgNp samples showed slower bacterial reduction compared with the sample without collagen (ns: not statistically significant).

F).

To assess the potency of the collagen-AgNp composites in bacterial growth inhibition, we measured the optical density of *E. coli*, when growing in the presence of the composites (Figure 3. Bacterial collagen as a template for the synthesis of AgNps. (A) The scheme shows the interactions between the functional groups of the collagen and the silver ions as the driving force for the nucleation of silver nanoparticles. (B) UV-Visible spectra of the composites with different concentrations of collagen. Higher collagen content increased the reduction of silver ions and the formation of AgNps. (C) UV-Visible spectra of the composites at different temperatures. At higher reaction temperatures, the reduction rate of silver ions increases. (D)

SEM images of composites in the presence and absence of collagen at different temperatures. In the absence of collagen AgNps, tended to aggregate and form larger particles. At both temperatures AgNps were uniformly distributed along the fibers, confirming the effect of collagen in controlling the reduction reaction. The scale bar is 500 nm. (E, F) EDS map and elemental analysis of silver and nitrogen. The CL4X/AgNp showed a strong elemental signal of silver and its uniform distribution throughout the composite. The scale bar is 500 nm. (G) OD600 of the E. coli in the presence of different formulations of composites. CL/AgNp samples showed slower bacterial reduction compared with the sample without collagen (ns: not statistically significant).

G). We started the measurement at OD_{600}= 0.83 (t=0). At t=0, all the samples with CL/AgNp showed a higher OD_{600} compared with the control (cells only), which was because of the partial absorbance of AgNp at 600 nm (OD_{600} of a control sample containing LB and 100 uL of only AgNp at t=0 was 0.2). By increasing the incubation time, the OD_{600} of both controls increased (cells and collagen only), which indicated that the presence of collagen did not impede cell growth. However, the OD_{600} for all of the AgNp-containing samples decreased, starting at t=1 h, which indicated both growth inhibition of the cells and oxidation of the AgNp to the Ag^{+} form, the active form for antibacterial activity of the AgNps. Silver nanoparticles can continually release silver ions and due to the electrostatic interaction with the bacterial membrane, they can adhere to the cytoplasmic membrane, therefore, enhancing the permeability of the cytoplasmic membrane and disrupting the bacterial envelope. [178] This interaction can prevent further cells growth. It is worth noticing that the bacterial inhibition of the collagen-containing samples was slower than the sample without. For example, the bacterial reduction of the CL4X/AgNp sample was two times less than the AgNp sample after 18 hours. This slow release may be due to the stabilization of the AgNps

by bacterial collagen that prevents burst release. The controlled and sustained release of an antibacterial agent can potentially lead to a prolonged antimicrobial efficacy and be beneficial for wounds that would require a longer healing process, such as chronic diabetic wounds and bone defects. [179-181] In addition, we assessed the antibacterial activity of the AgNp composites by colony counting methods (Figure S5. 1), which revealed that all the AgNp-containing samples inhibited the growth of *E. coli* within 60 minutes.

Mineralization of bacterial collagen with hydroxyapatite (HAP). We also used bacterial collagen to mineralize HAP crystals using $CaCl_2$ and Na_2HPO_4 solutions containing Ca^{2+} and PO_4^{3-} precursors. In the formation of natural bone, collagen and non-collagenous component are known to play a critical role in directing the growth of hydroxyapatite minerals. [182] Non-collagenous proteins, such as bone sialoprotein, osteonectin, and osteopontin often consist of a high content of negatively charged residues, such as aspartic acid (Asp, D) and glutamic acid (Glu, E), with a high affinity for calcium ions. [49, 64] While bacterial collagen lacks the periodicity and the hole zone feature that is specific for type I collagen, we postulated that the presence of charged and polar residues could make it a proper scaffold for the formation of the HAP minerals. After the negatively charged amino acids (D and E), with a total content of ~17% in bacterial collagen, glutamine (Gln) has the highest affinity constant for HAP crystal. [49] Glutamine is the most abundant uncharged polar amino acid in the structure of bacterial collagen (~8%) and can make a huge impact on the mineralization potential of bacterial collagen.

A.

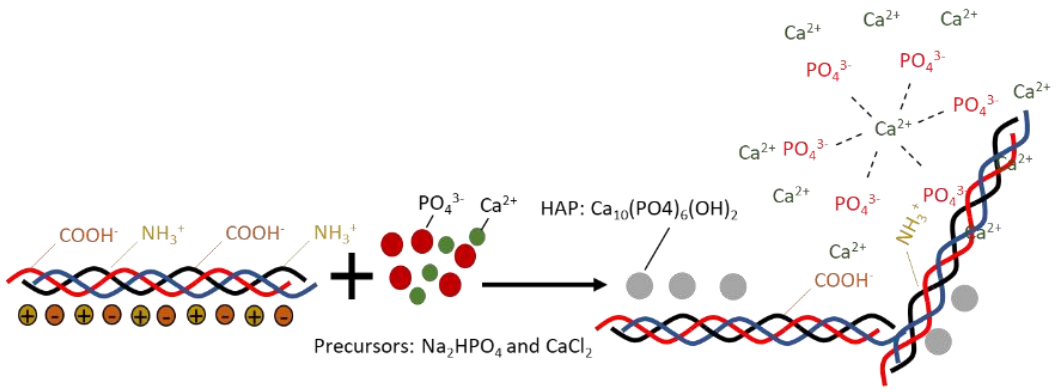
COOH-
NH3+
COOH-
NH3+
PO4 3-
Ca2+
HAP: Ca10(PO4)6(OH)2
Precursors: Na2HPO4 and CaCl2
Ca2+
PO4 3-
COOH-
NH3+

B.

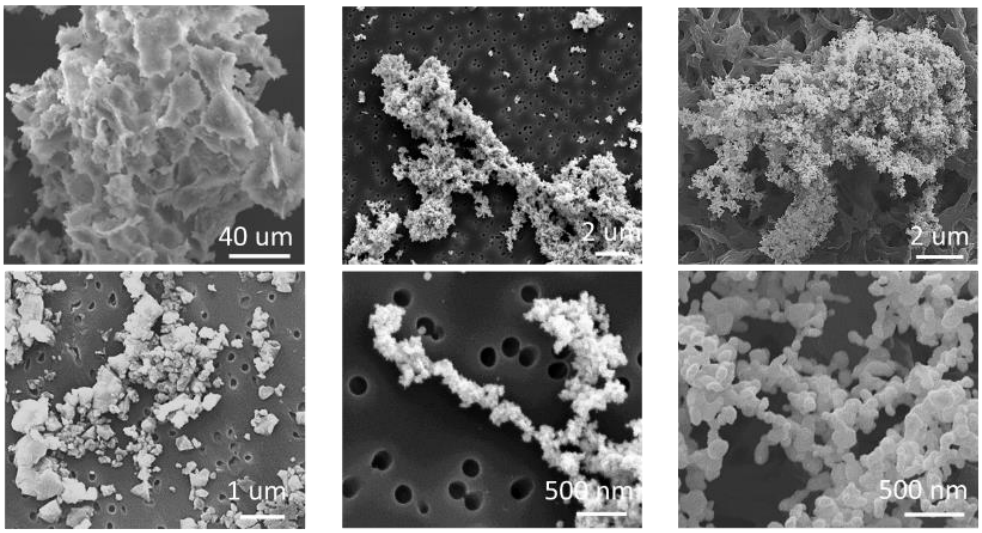
HAP only (No CL)
CL1X/HAP
CL4X/HAP
40 um
2 um
2 um
1 um
500 nm
500 nm

C.

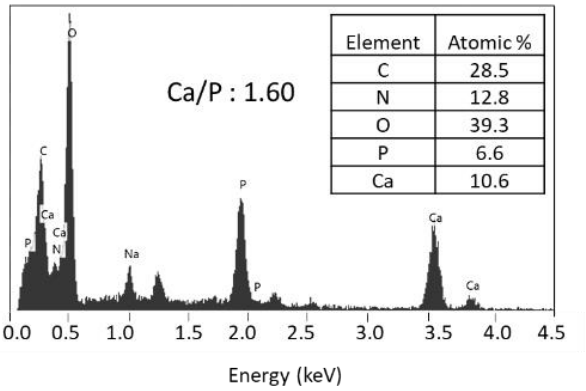
Ca/P : 1.60
Element | Atomic %
C | 28.5
N | 12.8
O | 39.3
P | 6.6
Ca | 10.6
Energy (keV)

D.

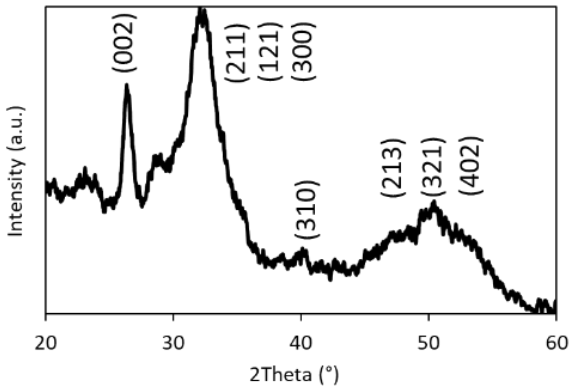
(002)
(211)
(121)
(300)
(310)
(213)
(321)
(402)
Intensity (a.u.)
2Theta (°)

E.

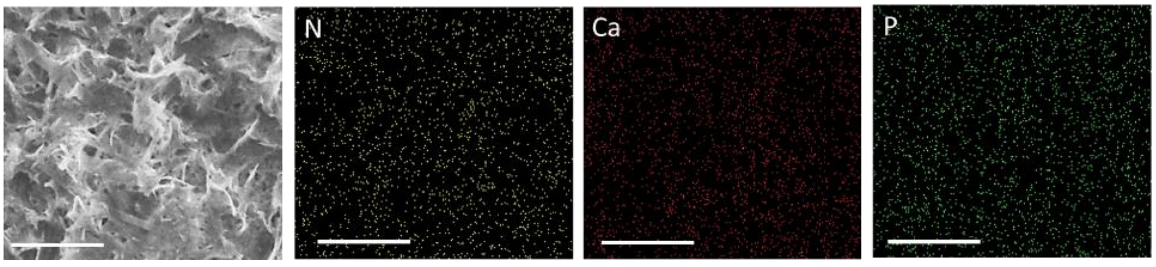
N
Ca
P

Figure 5. 1. Bacterial collagen as a template for synthesis of hydroxyapatite. (A) The scheme shows the initiation of HAP nucleation by positively and negatively charged groups on the collagen. (B) SEM images of the different formulations of the HAP composites. In the presence of collagen smaller crystals were formed with a more uniform distribution compared with the sample with no collagen. (C) Elemental analysis using EDS confirmed the formation of hydroxyapatite. (D) XRD identified the main characteristic peaks for crystalline HAP. (E) EDS map showed that collagen prevents the local aggregation of the HAP crystals (scale bar is 2 µm).

To analyze the formation of the HAP minerals we used SEM to observe the mineralized scaffolds. (Figure 5. 1B). The formation of HAP without the collagen substrate resulted in the formation of the large particles (up to 1 µm) with random shapes, due to the fast and uncontrolled reaction between the ion precursors (Ca^{2+} and PO_4^{3-}). However, the presence of the collagen as a template directed the formation of HAP crystals with uniform shape and size (less than 200 nm). After the mineralization, collagen retained its fibrillar and highly entangled micro-strand structure, which is key for supporting the cell seeding and *in vitro* growth of bone tissue in tissue engineering applications. [183, 184] Both mineralized collagen samples (CL1X/HAP and CL4X/HAP) showed dense nucleation of HAP along the fibers with platelet morphology, which is the dominant morphology for the HAP crystals. [64] The EDS results demonstrated that Ca and P element peaks in addition to N and O peaks were detected within the CL4X/HAP composite scaffold. The Ca/P ratio of the deposited particles was 1.6, very close to the theoretical ratio in HAP ($(Ca_{10}(PO4)_6(OH)_2)$: 1.67) (Figure 5. 1C). [120, 185] Moreover, the XRD spectrum of the CL4X/HAP sample indicated the main characteristic peaks for crystalline HAP at around 32°, 26°, and 40° 2θ, corresponding to the (211), (002), and (310) diffraction planes of crystalline HAP (Figure 5. 1D). [185] Two broad peaks at 32° and 50° are respectively corresponding to the crystallographic planes (211), (121), (300) and (213), (321), (402) combined into the broad peaks, indicating a relatively low degree of crystallinity and nanosized dimensions. [186, 187]

EDS elemental map of the CL4X/HAP further indicated that the distribution of Ca and P (from HAP) was homogenous and consistent with the distribution of the N (from proteins), indicating a uniform interaction of the ion precursors (Ca^{2+} and PO_4^{3-}) with the charged residues in the collagen backbone (Figure 5. 1E).

Mineralization of bacterial collagen with silica. To fabricate a collagen/silica composite we used TMOS as a precursor and Tris-HCl as a hydrolyzing agent. After 10 to 15 minutes of TMOS treatment, the composites started gelating and forming aggregates. Immediately after the treatment, we cast the solutions in a silicone mold and let them solidify (Figure 5. 2B). When the TMOS (the source of alkoxide) is mixed with Tris-HCl, the hydrolysis takes place followed by the condensation reaction of silanol groups that produce oligomers. [188] The gelation of the silica is pH-dependent. The pH of the reaction mixture was 6.8, higher than the isoelectric point of silicic acid (pH=2), therefore, gelation can be catalyzed by the anionic form of the silicic acid. [189] This mechanism supports the fact that the processability of bacterial collagen, such as hydrogel formation, can be improved by silica-induced gelation. Also, gelation of this composite at around pH=7 (close to the physiological pH) can be beneficial to activate *in situ* gelations of hydrogels after injection to the bone defects. To further study the microstructure of the collagen/silica composites we first used SEM (Figure 5. 2B). Starting with the pure silica gel, in addition to the aggregation of the silica particles, the SEM images showed relatively smooth topography of the surface with no porosity and an interconnected network. The presence of fibrillar collagen significantly changed the structure of the hydrogels. The collagen retained its 3D porous and fibrillar structure after silicification. Besides, silica particles formed along the collagen fibers. The surface of silica contains a high density of silanol groups, thus, electrostatic interactions between

the negatively charged silanol groups and positively charged groups present on collagen, such as the amine groups, enhance the interactions between the SiO_2 particles and the collagen matrix. [69]

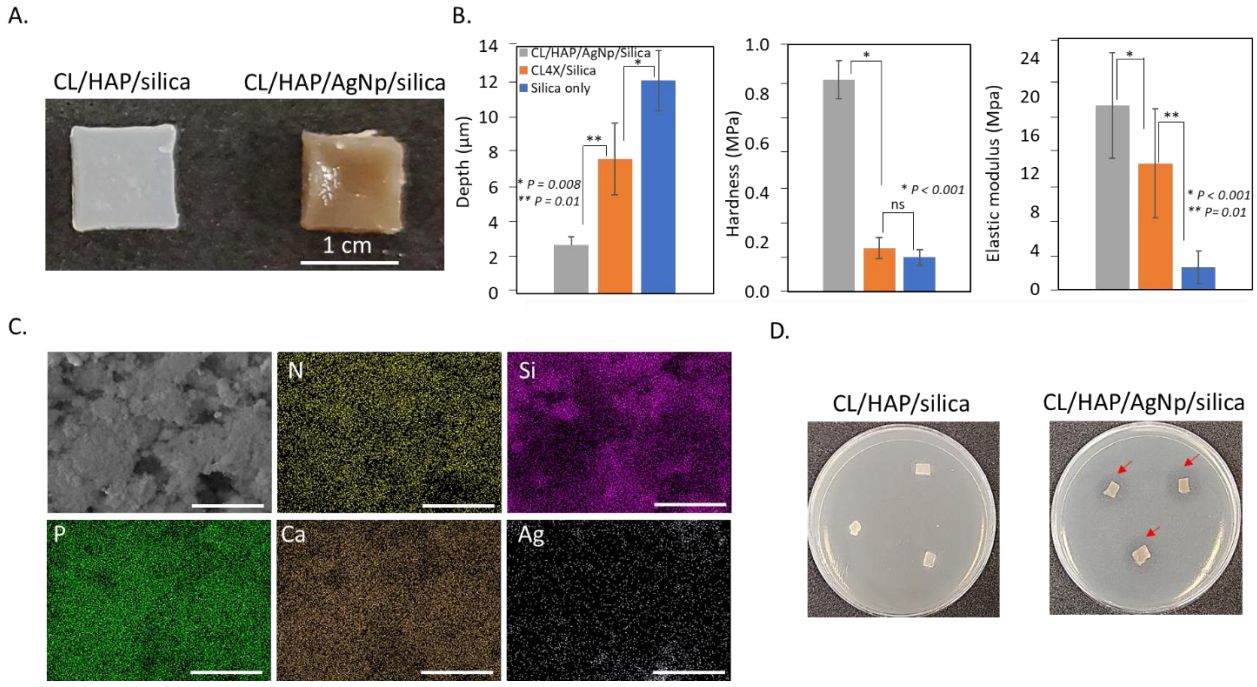

Figure 5. 2. Collagen as a template to nucleate three inorganic particles (HAP, AgNp, and silica). (A) Optical images of the collagen composites, which were formed into the shape of the molds. (B) Maximum depth, hardness, and elastic modulus of different formulations obtained by indentation test. The four-component composite showed superior mechanical properties compared with silica only and collagen/silica samples (ns: not statistically significant). (C) Distribution map of the main elements from the inorganic particles and collagen obtained by EDS shows the uniform throughout the composite. The scale bar is 10 µm. (D) Zone of Inhibition Test. Silver nanoparticles inhibited the growth of bacteria and provided antibacterial properties for the four-component composite.

We also observed a higher water absorption for the CL4X/Silica hydrogel (100. 9% ± 22.4%) compared with silica hydrogel (6.1% ± 2.6%). This difference was likely due to the 3D porous structure of the collagen and its higher hydrophilicity compared with silica. High porosity and water absorption are beneficial for cell growth and allow adhesion and proliferation of the cells when using the composite as a regenerative scaffold. [190] Collagen also affected the hardness and

elastic modulus of the silica composite. Figure 5. 2C presents the relationship between the load and the maximum indention depth for the silica samples with and without collagen. After adding collagen to the silica, the maximum indention depth under the same load decreased, indicating that the hardness and elastic modulus increased. Collagen can penetrate the submicron features of the silica hydrogel and through interaction with its charged residues, it can organize the silica particles in a more controlled and organized manner to strengthen the surface.

In the FTIR analysis (Figure 5. 2D), the collagen sample exhibited characteristic IR bands at 1650 cm^{-1} attributed to amide I C=O stretching and 1550 cm^{-1} to amide II N-H bending. [191] The silica sample showed the characteristic absorptions at 795 cm^{-1} arising from the bending motion of Si–O–Si bridges, 1020 cm^{-1} assigned to Si–O–Si stretching with a shoulder at around 910 cm^{-1} attributed to the stretching vibration of Si-OH groups, and 3200 cm^{-1} related to the stretching vibration of the silanol groups (Si-OH). [192, 193] In the collagen/silica samples (CL1X/Silica and CL4X/Silica) the peak at 795 cm^{-1} corresponding to Si–O–Si bridges appeared, confirming the silicification. The band shift from 1650 cm^{-1} to 1635 cm^{-1} of amide groups in both CL1X/Silica and CL4X/Silica samples was indicative of the interactions between hydroxyl groups on the surface of silica and amide groups in the side chains of collagen.

Further, after fabrication of the CL4X/Silica composite and adequate washing to remove the unreacted TMOS and remaining Tris-HCl buffer, we analyzed it by EDS for the detection and distribution of silicon. The EDS profile illustrated the strong silicon peak at approximately 2 keV after TMOS treatment (Figure 5. 2E). [194] To further elucidate the effect of the collagen on the distribution of the silanol group throughout the composite, we obtained the nitrogen and silicon elemental map by EDS. N (from collagen) and Si (from silica) are generally uniformly dispersed throughout the collagen/silica and their signals overlap, because of the uniform distribution of the

silanol groups long the collagen fibers. In some areas, the intensities of elemental signals vary, due to small thickness variations in the sample, as seen in the representative SEM image (Figure 5. 2F). Through silica mineralization, the bacterial collagen composite can be gelated and could have more potential for biomaterials applications. More specifically, the collagen-silica composite could be a potential injectable scaffold for bone tissue engineering. [195] The physiological pH is higher than the pI of silicic acid, therefore, the composite could undergo *in situ* gelations after injection.

Mineralization of bacterial collagen with silica, HAP, and AgNp. The healing process of the bone defects is extremely long and complicated and can pose a big risk of bacterial contamination. Therefore, the development of bone grafts that are capable of simultaneously controlling infections and promoting bone regeneration would be advantageous. [63, 196] As we showed in the previous sections, the three minerals are uniformly dispersed through the bacterial collagen network, and a combination of all three with bacterial collagen could result in a multifunctional composite. To fabricate a composite of collagen with HAP, silica, and AgNp, we used prefabricated collagen/HAP and collagen/AgNp composites that we then mixed with silica precursors (Figure 5. 3A). This strategy allowed to avoid the uncontrolled nucleation of the minerals, and to ensure that nucleation sites were available on the collagen template to mineralize each type of nanoparticle.

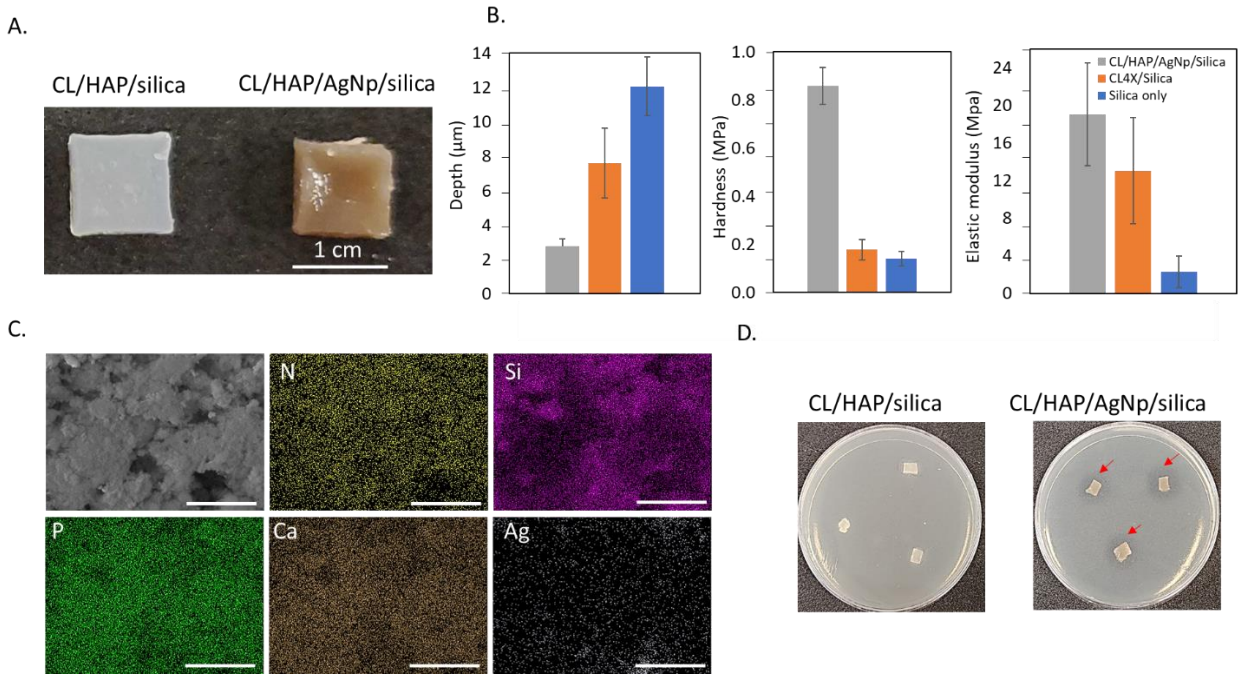

Figure 5. 3. Collagen as a template to nucleate three inorganic particles (HAP, AgNp, and silica). (A) Optical images of the collagen composites, which were formed into the shape of the molds. (B) Maximum depth, hardness, and elastic modulus of different formulations obtained by indentation test. The four-component composite showed superior mechanical properties compared with silica only and collagen/silica samples. (C) Distribution map of the main elements from the inorganic particles and collagen obtained by EDS showing the uniform throughout the composite. The scale is 10 µm. (D) Zone of Inhibition Test. Silver nanoparticles inhibited the growth of bacteria and provided antibacterial properties for the four-component composite.

Using indentation, we compared the hardness and elastic modulus of the CL/HAP/AgNp/silica composite with the CL/silica sample (Figure 5. 3B). After the addition of HAP and AgNp to the CL/silica composite, the hardness increased from 0.18 MPa to 0.86 MPa. This increment, in addition to the increase of elastic modulus, can be attributed to an increase in resistance against deformation in the presence of HAP crystals and silver nanoparticles, as the maximum depth also decreased from 7.62 µm to 2.76 µm.

In the composites consist of several minerals, the particles are often prone to aggregate, which makes it important to study the distribution of each element in the composite. Using EDS, we observed a uniform distribution of the characteristic elements (N, Si, Ag, Ca, and P) throughout the composite (Figure 5. 3C). There were areas where the population of Si is slightly higher than others, which can be because of the fast gelation reaction and can be controlled by the slower addition of Tris-HCl. The overall uniformity of the distribution comes from the controlled nucleation of the ions and their stabilization by the functional groups in bacterial collagen.

We further qualitatively tested the antibacterial efficacy of the CL/HAP/AgNp/silica composite (Figure 5. 3D). The release of AgNp from the composite into the agar exerts a bacterial growth-inhibiting effect and a clear zone of inhibition appeared around the sample, compared with the control (CL/HAP/silica) that showed no zone of inhibition.

Overall, combining the three minerals in a single composite brought together the advantageous properties of each mineral. The presence of the AgNps provided antibacterial properties and increased hardness along with HAP crystals. Silica, with its gelation, served as a useful component to broaden the processability and applicability of collagen mineral composites as biomaterials.

5.6. Conclusion

In a composite biomaterial consisting of nanoparticles, uniform interaction between substrate and particles and controlled particle size are key parameters. Bacterial collagen contains a high content of charged amino acids that can support the controlled nucleation and uniform distribution of the inorganic particles. In addition, the nano-sized collagen fibrils can direct the nucleation and growth of the particles, and its 3D structure provides a porous network structure of the protein/mineral

composite, with potential for bone tissue engineering. Collagen/AgNp composites exhibited slower bacterial inhibition compared with the sample without collagen, which indicated a sustained release of AgNps when using a scaffold. Collagen/HAP composites showed uniformly synthesized HAP platelets along the collagen fibers, compared with HAP crystals synthesized without collagen that formed aggregated structures. Silicification of the collagen resulted in a hydrogel with a porous network that could be easily molded into macroscopic self-standing structures and was more water-absorbent compared with silica-only gels. Overall, we showed that the three different minerals can provide bacterial collagen with new features, AgNps with antibacterial properties, HAP as the main bone mineral, and silica as both processable and bone cement component. All three were dispersed uniformly along the collagen fibers. Therefore, the combination of all three types of nanomaterials with bacterial collagen can pave the way for designing new bone regenerative scaffolds.

5.7. Supporting information

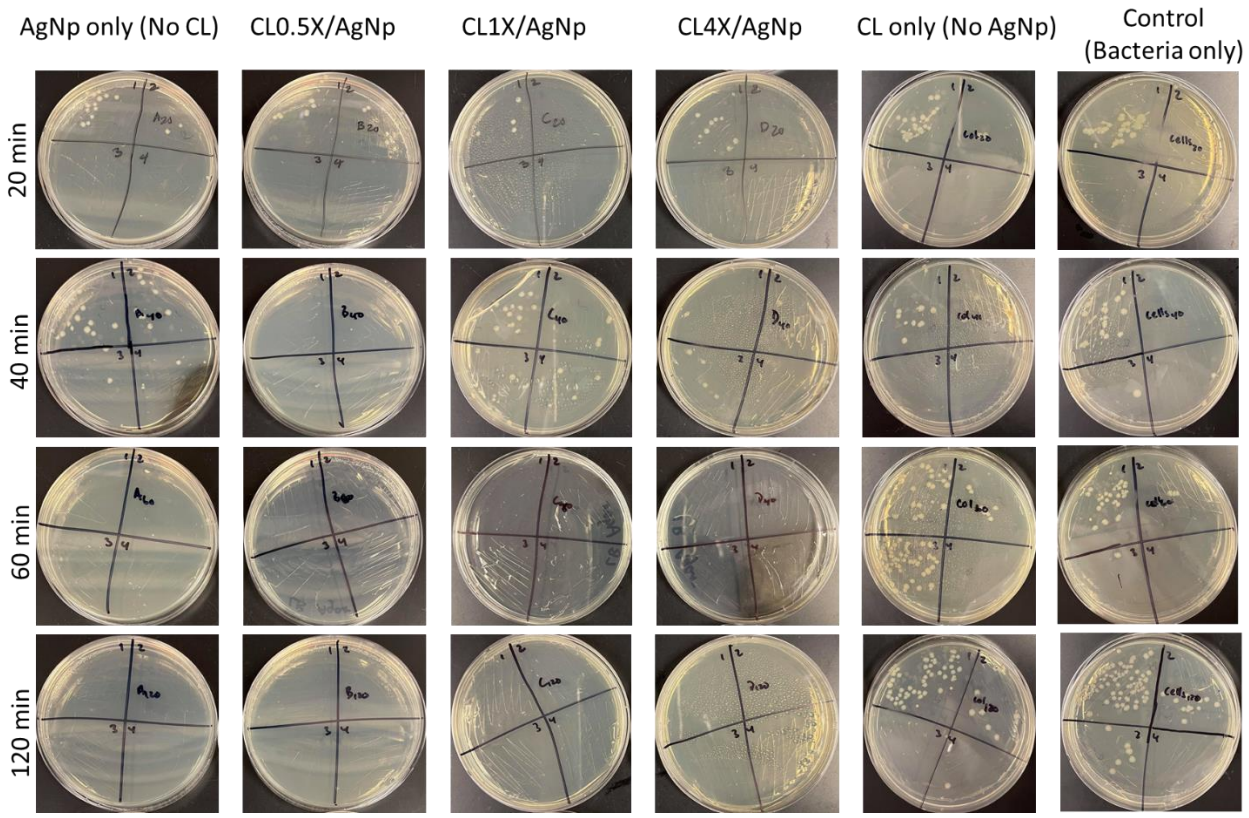

Figure S5. 1. Colony counting antibacterial test. After 60 minutes all the AgNp formulations inhibited the growth E. coli.

5.8. Acknowledgments and funding sources

The authors thank the Facility for Electron Microscopy and Research (FEMR) at McGill for assistance with SEM. This research was funded, in part, by the Natural Sciences and Engineering Research Council of Canada (NSERC) through a Discovery grant (NSERC RGPIN-2017-04598), by the Fonds de Recherche du Québec - Nature et Technologies (FRQNT), and it was undertaken, thanks to the funding from the Canada Research Chairs Program and the support by the Canadian

Foundation for Innovation (project #37524). Z.A. is grateful for financial support via a McGill Engineering Doctoral Award (MEDA) and an FRQNT Doctoral Research Scholarship.

Chapter 6. Discussion

Obtaining the collagen from a safe and scalable source has been a challenge for the fabrication of biomaterials. In this work, we used recombinant bacterial collagen as a promising alternative for overcoming the challenges of the use of animal sources and the fabrication of biomaterials.

To limit the problems associated with intracellular secretion production of recombinant proteins, we adapted the curli secretion pathway (one of the systems for extracellular secretion of CsgA protein in *E. coli)*, modified it, and introduced it for the extracellular secretion of bacterial collagen. We demonstrated that using this secretion pathway can simplify the downstream process, by preventing the proteins from accumulating inside the cells and avoiding the cell lysis process.

Relying on this extracellular secretion system, we also established a purification process that was simpler, less expensive, and more scalable than chromatography-based purification. Secretion of bacterial collagen directly into the extracellular media helped us to isolate it using the filtration method (with the steps of enzymatic digestion and acid precipitation), while the yield and purity were comparable to the affinity chromatography method. The isolated proteins retained their structural integrity and secondary structure after purification by the filtration method. However, the purified protein samples that were exposed to the enzymatic digestion and acid treatment showed some partial denaturation and unfolding, which possibly can be avoidable by omitting the pepsin digestion step and protecting collagen against acids.

Previously, the possible assembly mechanism of the bacterial was stated to be related to the high content of the charged residues, which is around 30% of bacterial collagen (2-times higher than fibrillar animal collagen). There are a lot of charge pairs of glutamate/arginine and lysine/aspartate in the N- and C- terminal of bacterial collagen, which can provide some effective interactions for

the collagen molecules to form into long fibers, as we confirmed by SEM and AFM images. Even though bacterial collagen can self-assemble into long fibers, its smaller size compared with animal collagen requires it to be modified for improved processability. Physical or chemical modifications have been used to improve the gelation and mechanical stability of bacterial collagen. Here, we were inspired by the enormous uses of animal collagen in biomineralization, to apply bacterial collagen in a composite system with inorganic particles, which consequently can provide bacterial collagen with new properties such as antibacterial properties and improved gelation.

Generally, self-associating proteins, such as bacterial collagen, with high content of charged residues and carboxylate groups, are a proper substrate for the bottom-up synthesis of inorganic particles. They can provide nucleation sites and direct the controlled growth of the particles. Therefore, we first explored this topic by biomineralization of CsgA proteins, as a simple and well-understood assembling protein. We modified CsgA by truncating it and fusing it with a short peptide that has a specific affinity to hydroxyapatite (HAP). The modified CsgA monomer was secreted extracellularly, self-assembled, and aggregated into the large fibrillar structure, as we verified by SEM and AFM images. In addition, the presence of HAP-binding peptide provided more nucleation sites for the mineralization of HAP compared with the wild-type CsgA. However, to better elucidate the advantage of having the HAP-binding peptide in this system, studying the stability of the interaction between the HAP crystals and the protein substrate would be beneficial. In addition, studying the HAP mineralization in different concentrations and forms of the ion precursors would be beneficial to obtaining an optimum mineralization protocol with less surface mineralization. Also, a more thorough crystallinity study, using XRD and TEM on the samples with and without HAP-binding peptide, will be needed to clarify the difference between these samples. In previous studies, when a CsgA hybrid protein was used as a coating for dental

nanomaterials, high biocompatibility (without triggering immune responses in animal experiments) was observed. Nevertheless, since CsgA is a type of amyloid protein, associated with some concerns about stimulating an immune response, its immunogenicity would need to be studied by detecting inflammatory markers *in vivo*. Overall, we showed that the CsgA system can be used as a tool to self-assemble a free peptide and gives it the potential to be applied as a more macroscopic form in biomaterials design.

We then studied the mineralization of the three inorganic particles on the collagen substrate: silica (for improving the gelation and processability of collagen), silver nanoparticles (AgNp, for antibacterial properties), and hydroxyapatite (as a potential bone substitute). We addressed the processability issue of bacterial collagen by silica gelation, which formed the collagen into a handleable hydrogel, with the potential to be applied as an injectable hydrogel *in vivo*. In addition, in both HAP and AgNps mineralization, collagen controlled the nucleation and interaction of the ions with the substrates. In addition, in all the mineralization reactions, the high content of charged residues in bacterial collagen played a key role in the growth of the particles, and their distribution, confirmed by EDS elemental maps. Finally, we fabricated a multi-functional collagen-based composite with these three inorganic particles. Our results demonstrated an increased hardness (around 5 times) after adding the HAP and AgNp to the collagen-silica composite. We wish that this multi-component collagen composite can be potentially used to repair bone defects, which usually have a long healing process and can pose a big risk of bacterial contamination.

Overall, we were able to improve the mechanical integrity of bacterial collagen by applying it to a composite system. However, to improve the gelation of the bacterial collagen itself, when it is used as a pure material, further engineering could be performed – for instance, we could duplicate the

length of bacterial collagen or insert functional peptides that can increase its self-assembly, and consequently its gelation.

Lastly, the model that we introduced needs further characterizations to validate whether it is a proper candidate for bone graft applications. For example, using a compression test, the mechanical properties of the composites with different ratios of inorganic particles could be evaluated to obtain a formulation with stiffness comparable to human bone. In addition, an ideal tissue-engineered graft needs to be biodegradable over the desired healing period. Thus, the biodegradation of the composites would need to be assessed to ensure their mechanical integrity in physiological conditions. Lastly, the grafts need to be biocompatible and non-immunogenic for human cells. We would need to assess the biocompatibility of the composites in two ways: 1) growth behavior (adhesion/spreading) of human osteoblast and fibroblast cells and studying their morphology using optical and electron microscopes, 2) differentiation of osteoprogenitor cells while cultured on the bone grafts.

Chapter 7. Conclusions and future works

7.1. Conclusions

This thesis describes the recombinant production of two self-associating bacterial proteins and their use for bio-inspired mineralization.

Chapter 3 explores the use of the curli assembly mechanism for the self-assembly of short functional peptides that can be used as macroscopic hydrogel biomaterials for mineralization. Chapter 4 investigates the use of the curli secretion pathway for the extracellular secretion of bacterial collagen and describes the easy and scalable protocols for the purification of bacterial collagen. Finally, chapter 5 explores the use of bacterial collagen for the mineralization of three different inorganic particles, silver nanoparticles, hydroxyapatite crystals, and silica particles.

A few important conclusions were driven from these chapters. Chapter 3 demonstrated that the minimized CsgA protein (which consists of only R1 and R5) can serve as a tool for the assembly of the free peptides, such as a hydroxyapatite-binding peptide. The final truncated and modified CsgA-like peptide was able to self-assemble into fiber-like structures and form a macroscopic hydrogel with the potential for hydroxyapatite mineralization. Chapter 4 showed that the curli secretion system, and its minimized pathway, can be used for extracellular secretion of the non-CsgA proteins, such as bacterial collagen. The extracellular secretion approach simplified the isolation of bacterial collagen by eliminating the need for cell lysis and interference of other host proteins, which is an important factor for the scalability of the recombinant proteins and their massive production for different biotechnology applications. This chapter further demonstrated how using non-chromatography methods we can isolate and purify bacterial collagen, and any

collagen-like protein, in a fast, easy, and scalable way. Finally, chapter 5, demonstrated the potential of bacterial collagen for use as a substrate for the mineralization of different inorganic particles, with different mechanisms. Combining collagen with minerals has some benefits for both components. Collagen rendered a uniform distribution and controlled particle size to the inorganic particles. In addition, using silica, bacterial collagen was able to be processed in the form of a handable hydrogel, while it cannot form a thick hydrogel when it is being used alone.

Overall, the findings presented in this thesis highlights the versatility of the curli system through observations done in chapter 3 and 4 together (minimizing CsgA and secreting non-CsgA proteins through a minimized operon) and the potential uses of collagen-like proteins based on Chapter 4 and 5 together (secretion, processing, mineralization), which both have significant implications for the use of recombinant proteins in the field of biomaterials

7.2. **Suggestions for future works**

Suggestions for future works include:

- Use of minimized CsgA protein for assembly of functional peptides, such as silver-binding peptides and silica-binding peptides. This approach will eliminate the need for physical or chemical conjugation of these peptides with the scaffold and provides a stable interaction between the scaffolds and particles.
- Study the potential of the curli secretion pathway for other proteins, different from the structure and size of bacterial collagen, to elucidate the compatibility of the curli pathway, especially the CsgG proteins, with different proteins. This approach will broaden the use curli pathway for other non-CsgA proteins and simplify their purification and mass production.

- Genetically modifying the bacterial collagen with the peptides that specifically bind with the silver nanoparticles, hydroxyapatite, and silica and comparing the level of mineralization, distribution of the particles, and stability and release of minerals between the physically and genetically modified scaffolds.

- A comprehensive study on the mechanical properties of the four-component collagen composite and exploring the ways for improving them to be comparable with the mechanical properties of human bone. Since the final goal is to use these scaffolds for bone regeneration, *In vivo* studies in this regard will be valuable.

- Genetically modifying bacterial collagen, so that it can be assembled and formed longer fibers compared with the wild-type bacterial collagen. Bacterial collagen has lower mechanical stability and gelation properties compared with animal collagen, and this modification can improve the thermal and mechanical stability and processability of bacterial collagen.

- Fusion of bacterial collagen with antibacterial peptides and antiaging peptides, to broaden the use of bacterial collagen in the skincare market and be used as “vegan” material.

- Conjugating bacterial collagen with truncated CsgA and studying the potential of vacuum filtration for isolation of this fusion. Using this modification, CsgA will form large aggregates and protect bacterial collagen against harsh conditions, which makes it compatible with vacuum filtration, a scalable purification method.

- Fusion of bacterial collagen with a cell anchoring protein, so that it can be anchored to the bacterial after secretion and can be used as a living biofilm. This modification can make a system with the ability to self-power, self-heal, and respond to biosignals.

References

1. Parenteau-Bareil, R.; Gauvin, R.; Berthod, F., Collagen-Based Biomaterials for Tissue Engineering Applications. *Materials* **2010,** *3* (3), 1863.
2. Egli, J.; Schnitzer, T.; Dietschreit, J. C. B.; Ochsenfeld, C.; Wennemers, H., Why Proline? Influence of Ring-Size on the Collagen Triple Helix. *Org Lett* **2020,** *22* (2), 348-351.
3. Albaugh, V. L.; Mukherjee, K.; Barbul, A., Proline Precursors and Collagen Synthesis: Biochemical Challenges of Nutrient Supplementation and Wound Healing. *J Nutr* **2017,** *147* (11), 2011-2017.
4. Sipila, K. H.; Drushinin, K.; Rappu, P.; Jokinen, J.; Salminen, T. A.; Salo, A. M.; Kapyla, J.; Myllyharju, J.; Heino, J., Proline hydroxylation in collagen supports integrin binding by two distinct mechanisms. *J Biol Chem* **2018,** *293* (20), 7645-7658.
5. Berillis, P., *Marine Collagen: Extraction and Applications*. SM Group: Dover, DE, USA: 2015.
6. *Collagen Market Size, Share & Trends Analysis Report, 2021 - 2028*; Grand View Research, 2021.
7. Leon-Lopez, A.; Morales-Penaloza, A.; Martinez-Juarez, V. M.; Vargas-Torres, A.; Zeugolis, D. I.; Aguirre-Alvarez, G., Hydrolyzed Collagen-Sources and Applications. *Molecules* **2019,** *24* (22).
8. Gopal, G. J.; Kumar, A., Strategies for the production of recombinant protein in Escherichia coli. *Protein J* **2013,** *32* (6), 419-25.
9. M Metsäranta 1, S. G., C Smith, K Niederreither, B de Crombrugghe, E Vuorio, Developmental Expression of a Type I1 Collagen/P-GalactosidaseFusion Gene in Transgenic Mice. *Developmental Dynamics* **1995,** *204*, 202-210.
10. Tatemastu, K., Utilization of Transgenic Silkworms for Recombinant Protein Production. *Journal of Biotechnology & Biomaterials* **2012,** *s9* (01).
11. Brodsky, B.; Kaplan, D. L., Shining light on collagen: expressing collagen in plants. *Tissue Eng Part A* **2013,** *19* (13-14), 1499-501.
12. Xiao X. Ma, D. D. F., Chen H. Zhu, Zi F. Shang and Yu Mi, Optimization of fermentation medium for collagen production of recombinant Pichia pastoris during induction phase. *Journal of Chemical and Pharmaceutical Research* **2014,** *6* (7), 1802-1809.
13. Yong Y Peng, L. H., Violet Stoichevska, Jerome A Werkmeister, Geoff J Dumsday and John A M Ramsha, Towards scalable production of a collagen-like protein from Streptococcus pyogenes for biomedical applications. *Microbial Cell Factories 2012* **2012,** *11* (146).
14. Ghosh, N.; McKillop, T. J.; Jowitt, T. A.; Howard, M.; Davies, H.; Holmes, D. F.; Roberts, I. S.; Bella, J., Collagen-like proteins in pathogenic E. coli strains. *PLoS One* **2012,** *7* (6), e37872.
15. Mohs, A.; Silva, T.; Yoshida, T.; Amin, R.; Lukomski, S.; Inouye, M.; Brodsky, B., Mechanism of stabilization of a bacterial collagen triple helix in the absence of hydroxyproline. *J Biol Chem* **2007,** *282* (41), 29757.
16. Dinjaski, N.; Kaplan, D. L., Recombinant protein blends: silk beyond natural design. *Curr Opin Biotechnol* **2016,** *39*, 1-7.

17. Ramshaw, J. A., Biomedical applications of collagens. *J Biomed Mater Res B Appl Biomater* **2016,** *104* (4), 665-75.
18. Seo, N.; Russell, B. H.; Rivera, J. J.; Liang, X.; Xu, X.; Afshar-Kharghan, V.; Hook, M., An engineered alpha1 integrin-binding collagenous sequence. *J Biol Chem* **2010,** *285* (40), 31046.
19. Wlodarczyk-Biegun, M. K.; Werten, M. W.; de Wolf, F. A.; van den Beucken, J. J.; Leeuwenburgh, S. C.; Kamperman, M.; Cohen Stuart, M. A., Genetically engineered silk-collagen-like copolymer for biomedical applications: production, characterization and evaluation of cellular response. *Acta Biomater* **2014,** *10* (8), 3620-9.
20. Lee, H. J.; Lee, J. S.; Chansakul, T.; Yu, C.; Elisseeff, J. H.; Yu, S. M., Collagen mimetic peptide-conjugated photopolymerizable PEG hydrogel. *Biomaterials* **2006,** *27* (30), 5268.
21. Bronk, J. K.; Russell, B. H.; Rivera, J. J.; Pasqualini, R.; Arap, W.; Hook, M.; Barbu, E. M., A multifunctional streptococcal collagen-mimetic protein coating prevents bacterial adhesion and promotes osteoid formation on titanium. *Acta Biomater* **2014,** *10* (7), 3354-62.
22. An, B.; Kaplan, D. L.; Brodsky, B., Engineered recombinant bacterial collagen as an alternative collagen-based biomaterial for tissue engineering. *Frontiers in Chemistry* **2014,** *2*.
23. An, B.; Abbonante, V.; Yigit, S.; Balduini, A.; Kaplan, D. L.; Brodsky, B., Definition of the native and denatured type II collagen binding site for fibronectin using a recombinant collagen system. *J Biol Chem* **2014,** *289* (8), 4941-51.
24. An, B.; DesRochers, T. M.; Qin, G.; Xia, X.; Thiagarajan, G.; Brodsky, B.; Kaplan, D. L., The influence of specific binding of collagen-silk chimeras to silk biomaterials on hMSC behavior. *Biomaterials* **2013,** *34* (2), 402.
25. Peng, Y. Y.; Stoichevska, V.; Madsen, S.; Howell, L.; Dumsday, G. J.; Werkmeister, J. A.; Ramshaw, J. A., A simple cost-effective methodology for large-scale purification of recombinant non-animal collagens. *Appl Microbiol Biotechnol* **2014,** *98* (4), 1807.
26. Merrett, K.; Wan, F.; Lee, C. J.; Harden, J. L., Enhanced Collagen-like Protein for Facile Biomaterial Fabrication. *ACS Biomater Sci Eng* **2021,** *7* (4), 1414.
27. Choi, J. H.; Lee, S. Y., Secretory and extracellular production of recombinant proteins using Escherichia coli. *Appl Microbiol Biotechnol* **2004,** *64* (5), 625.
28. Kleiner-Grote, G. R. M.; Risse, J. M.; Friehs, K., Secretion of recombinant proteins from E. coli. *Eng Life Sci* **2018,** *18* (8), 532-550.
29. Su, L.; Xu, C.; Woodard, R. W.; Chen, J.; Wu, J., A novel strategy for enhancing extracellular secretion of recombinant proteins in Escherichia coli. *Appl Microbiol Biotechnol* **2013,** *97* (15), 6705.
30. Yan, Z.; Yin, M.; Chen, J.; Li, X., Assembly and substrate recognition of curli biogenesis system. *Nat Commun* **2020,** *11* (1), 241.
31. Barnhart, M. M.; Chapman, M. R., Curli biogenesis and function. *Annu Rev Microbiol* **2006,** *60*, 131.
32. Blanco, L. P.; Evans, M. L.; Smith, D. R.; Badtke, M. P.; Chapman, M. R., Diversity, biogenesis and function of microbial amyloids. *Trends Microbiol* **2012,** *20* (2), 66.
33. Dorval Courchesne, N. M.; Duraj-Thatte, A.; Tay, P. K. R.; Nguyen, P. Q.; Joshi, N. S., Scalable Production of Genetically Engineered Nanofibrous Macroscopic Materials via Filtration. *ACS Biomater Sci Eng* **2017,** *3* (5), 733.
34. Van Gerven, N.; Goyal, P.; Vandenbussche, G.; De Kerpel, M.; Jonckheere, W.; De Greve, H.; Remaut, H., Secretion and functional display of fusion proteins through the curli biogenesis pathway. *Mol Microbiol* **2014,** *91* (5), 1022.

35. Evans, M. L.; Chapman, M. R., Curli biogenesis: order out of disorder. *Biochim Biophys Acta* **2014,** *1843* (8), 1551-8.
36. Christensen, L. F. B.; Schafer, N.; Wolf-Perez, A.; Madsen, D. J.; Otzen, D. E., Bacterial Amyloids: Biogenesis and Biomaterials. *Adv Exp Med Biol* **2019,** *1174*, 113-159.
37. Cao, B.; Zhao, Y.; Kou, Y.; Ni, D.; Zhang, X. C.; Huang, Y., Structure of the nonameric bacterial amyloid secretion channel. *Proc Natl Acad Sci U S A* **2014,** *111* (50), E5439-44.
38. Goyal, P.; Krasteva, P. V.; Van Gerven, N.; Gubellini, F.; Van den Broeck, I.; Troupiotis-Tsailaki, A.; Jonckheere, W.; Pehau-Arnaudet, G.; Pinkner, J. S.; Chapman, M. R.; Hultgren, S. J.; Howorka, S.; Fronzes, R.; Remaut, H., Structural and mechanistic insights into the bacterial amyloid secretion channel CsgG. *Nature* **2014,** *516* (7530), 250.
39. Klein, R. D.; Shu, Q.; Cusumano, Z. T.; Nagamatsu, K.; Gualberto, N. C.; Lynch, A. J. L.; Wu, C.; Wang, W.; Jain, N.; Pinkner, J. S.; Amarasinghe, G. K.; Hultgren, S. J.; Frieden, C.; Chapman, M. R., Structure-Function Analysis of the Curli Accessory Protein CsgE Defines Surfaces Essential for Coordinating Amyloid Fiber Formation. *mBio* **2018,** *9* (4).
40. Ashley A. Nenninger, L. S. R., and Scott J. Hultgren, Localized and efficient curli nucleation requires the chaperone-like amyloid assembly protein CsgF. *PNAS* **2009,** *106* (3), 900.
41. Taylor, J. D.; Zhou, Y.; Salgado, P. S.; Patwardhan, A.; McGuffie, M.; Pape, T.; Grabe, G.; Ashman, E.; Constable, S. C.; Simpson, P. J.; Lee, W. C.; Cota, E.; Chapman, M. R.; Matthews, S. J., Atomic resolution insights into curli fiber biogenesis. *Structure* **2011,** *19* (9), 1307.
42. Saldanha, D. J.; Abdali, Z.; Modafferi, D.; Janfeshan, B.; Dorval Courchesne, N. M., Fabrication of fluorescent pH-responsive protein-textile composites. *Sci Rep* **2020,** *10* (1), 13052.
43. Shehadul Islam, M.; Aryasomayajula, A.; Selvaganapathy, P., A Review on Macroscale and Microscale Cell Lysis Methods. *Micromachines* **2017,** *8* (3).
44. Mills, C. E.; Ding, E.; Olsen, B., Protein Purification by Ethanol-Induced Phase Transitions of the Elastin-like Polypeptide (ELP). *Industrial & Engineering Chemistry Research* **2019,** *58* (27), 11698-11709.
45. Chilkoti, D. E. M. a. A., Purification of recombinant proteins by fusion with thermally-responsive polypeptides. *Nature Biotechnology* **1999,** *17*.
46. Dorval Courchesne, N. M.; Duraj-Thatte, A.; Tay, P. K. R.; Nguyen, P. Q.; Joshi, N. S., Scalable Production of Genetically Engineered Nanofibrous Macroscopic Materials via Filtration. *ACS Biomater. Sci. Eng.* **2016,** *3* (5), 733-741.
47. Beniash, E., Biominerals--hierarchical nanocomposites: the example of bone. *Wiley Interdiscip Rev Nanomed Nanobiotechnol* **2011,** *3* (1), 47-69.
48. Xu, A.-W.; Ma, Y.; Cölfen, H., Biomimetic mineralization. *J. Mater. Chem.* **2007,** *17* (5), 415-449.
49. Tavafoghi, M.; Cerruti, M., The role of amino acids in hydroxyapatite mineralization. *Journal of The Royal Society Interface* **2016,** *13* (123), 20160462.
50. Li, Y.; Chiu, C.-Y.; Huang, Y., Biomimetic synthesis of inorganic materials and their applications. *Pure and Applied Chemistry* **2010,** *83* (1), 111-125.
51. Chen, Z.; Li, Z.; Lin, Y.; Yin, M.; Ren, J.; Qu, X., Biomineralization inspired surface engineering of nanocarriers for pH-responsive, targeted drug delivery. *Biomaterials* **2013,** *34* (4), 1364-71.
52. Xue, Z.-H.; Hu, B.-B.; Jia, X.-L.; Wang, H.-W.; Du, Z.-L., Effect of the interaction between bovine serum albumin Langmuir monolayer and calcite on the crystallization of CaCO3 nanoparticles. *Materials Chemistry and Physics* **2009,** *114* (1), 47-52.

53. Hazel-Ann Hosein, D. R. S., Mark Allen, and Trevor Douglas, Iron and Cobalt Oxide and Metallic Nanoparticles Prepared from Ferritin. *Langmuir* **2004,** *20*, 10283-1028.
54. Qin, D.; Yang, G.; Wang, Y.; Zhou, Y.; Zhang, L., Green synthesis of biocompatible trypsin-conjugated Ag nanocomposite with antibacterial activity. *Applied Surface Science* **2019,** *469*, 528-536.
55. Luckarift, H. R.; Dickerson, M. B.; Sandhage, K. H.; Spain, J. C., Rapid, room-temperature synthesis of antibacterial bionanocomposites of lysozyme with amorphous silica or titania. *Small* **2006,** *2* (5), 640-3.
56. De Stasio, G., Spectromicroscopy at the organic-inorganic interface in biominerals. *American Journal of Science* **2005,** *305* (6-8), 673-686.
57. Yu, L.; Martin, I. J.; Kasi, R. M.; Wei, M., Enhanced Intrafibrillar Mineralization of Collagen Fibrils Induced by Brushlike Polymers. *ACS Appl Mater Interfaces* **2018,** *10* (34), 28440-28449.
58. Ping, H.; Xie, H.; Wan, Y.; Zhang, Z.; Zhang, J.; Xiang, M.; Xie, J.; Wang, H.; Wang, W.; Fu, Z., Confinement controlled mineralization of calcium carbonate within collagen fibrils. *J Mater Chem B* **2016,** *4* (5), 880-886.
59. Mebert, A. M.; Alvarez, G. S.; Peroni, R.; Illoul, C.; Helary, C.; Coradin, T.; Desimone, M. F., Collagen-silica nanocomposites as dermal dressings preventing infection in vivo. *Mater Sci Eng C Mater Biol Appl* **2018,** *93*, 170-177.
60. Aime, C.; Mosser, G.; Pembouong, G.; Bouteiller, L.; Coradin, T., Controlling the nano-bio interface to build collagen-silica self-assembled networks. *Nanoscale* **2012,** *4* (22), 7127-34.
61. Ye, X.; Zhou, Y.; Chen, J.; Sun, Y., Synthesis and infrared emissivity study of collagen-g-PMMA/Ag@TiO2 composite. *Materials Chemistry and Physics* **2007,** *106* (2-3), 447-451.
62. Hosoyama, K.; Ahumada, M.; McTiernan, C. D.; Davis, D. R.; Variola, F.; Ruel, M.; Liang, W.; Suuronen, E. J.; Alarcon, E. I., Nanoengineered Electroconductive Collagen-Based Cardiac Patch for Infarcted Myocardium Repair. *ACS Appl Mater Interfaces* **2018,** *10* (51), 44668-44677.
63. Chen, P.; Wu, Z.; Leung, A.; Chen, X.; Landao-Bassonga, E.; Gao, J.; Chen, L.; Zheng, M.; Yao, F.; Yang, H.; Lidgren, L.; Allan, B.; Liu, Y.; Wang, T.; Zheng, M., Fabrication of a silver nanoparticle-coated collagen membrane with anti-bacterial and anti-inflammatory activities for guided bone regeneration. *Biomed Mater* **2018,** *13* (6), 065014.
64. Liam C. Palmer, C. J. N., Stuart R. Kaltz, Erik D. Spoerke, and Samuel I. Stupp, Biomimetic Systems for Hydroxyapatite Mineralization Inspired By Bone and Enamel. *Chem. Rev.* **2008,** *108*, 4754–4783.
65. Kim, D.; Lee, B.; Thomopoulos, S.; Jun, Y. S., The role of confined collagen geometry in decreasing nucleation energy barriers to intrafibrillar mineralization. *Nat Commun* **2018,** *9* (1), 962.
66. I, N. A.; Mohd Razip Wee, M. F.; Tabata, Y.; Bt Hj Idrus, R.; Nordin, A.; Fauzi, M. B., Antibacterial-Integrated Collagen Wound Dressing for Diabetes-Related Foot Ulcers: An Evidence-Based Review of Clinical Studies. *Polymers (Basel)* **2020,** *12* (9).
67. Alarcon, E. I.; Udekwu, K.; Skog, M.; Pacioni, N. L.; Stamplecoskie, K. G.; González-Béjar, M.; Polisetti, N.; Wickham, A.; Richter-Dahlfors, A.; Griffith, M.; Scaiano, J. C., The biocompatibility and antibacterial properties of collagen-stabilized, photochemically prepared silver nanoparticles. *Biomaterials* **2012,** *33* (19), 4947-56.
68. Anamaria Orza, O. S., Liliana Olenic, Mircea Diudea, Adrian Florea, Dan Rus Ciuca, Carmen Mihu, Daniel Casciano, and Alexandru S. Biris, Electrically Conductive Gold-Coated

Collagen Nanofibers for PlacentalDerived Mesenchymal Stem Cells Enhanced Differentiation and Proliferation. *ACS Nano* **2011,** *5* (5), 4490–4503.
69. Sarker, B.; Lyer, S.; Arkudas, A.; Boccaccini, A. R., Collagen/silica nanocomposites and hybrids for bone tissue engineering. *Nanotechnology Reviews* **2013,** *2* (4), 427-447.
70. Nguyen, P. Q.; Botyanszki, Z.; Tay, P. K.; Joshi, N. S., Programmable biofilm-based materials from engineered curli nanofibres. *Nat Commun* **2014,** *5*, 4945-4955.
71. Seker, U. O.; Chen, A. Y.; Citorik, R. J.; Lu, T. K., Synthetic Biogenesis of Bacterial Amyloid Nanomaterials with Tunable Inorganic-Organic Interfaces and Electrical Conductivity. *ACS Synth Biol* **2017,** *6* (2), 266-275.
72. Barnhart, M. M.; Chapman, M. R., Curli biogenesis and function. *Annu Rev Microbiol.* **2006,** *60*, 131-47.
73. Blanco, L. P.; Evans, M. L.; Smith, D. R.; Badtke, M. P.; Chapman, M. R., Diversity, biogenesis and function of microbial amyloids. *Trends Microbiol.* **2012,** *20* (2), 66-73.
74. Dorval Courchesne, N. M.; DeBenedictis, E. P.; Tresback, J.; Kim, J. J.; Duraj-Thatte, A.; Zanuy, D.; Keten, S.; Joshi, N. S., Biomimetic engineering of conductive curli protein films. *Nanotechnology*. **2018,** *29* (45), 454002-454013.
75. Praveschotinunt, P.; Dorval Courchesne, N. M.; den Hartog, I.; Lu, C.; Kim, J. J.; Nguyen, P. Q.; Joshi, N. S., Tracking of Engineered Bacteria In Vivo Using Nonstandard Amino Acid Incorporation. *ACS Synth Biol.* **2018,** *7* (6), 1640-1650.
76. Duraj-Thatte, A. M.; Courchesne, N. D.; Praveschotinunt, P.; Rutledge, J.; Lee, Y.; Karp, J. M.; Joshi, N. S., Genetically Programmable Self-Regenerating Bacterial Hydrogels. *Adv Mater.* **2019,** *31* (40), 1901826-1901835.
77. Nguyen, P. Q., Synthetic biology engineering of biofilms as nanomaterials factories *Biochem. Soc. Trans.* **2017,** *45*, 585–597
78. Wang, X.; Hammer, N. D.; Chapman, M. R., The molecular basis of functional bacterial amyloid polymerization and nucleation. *J Biol Chem.* **2008,** *283* (31), 21530-9.
79. Gilbert, C.; Ellis, T., Biological Engineered Living Materials: Growing Functional Materials with Genetically Programmable Properties. *ACS Synth Biol.* **2019,** *8* (1), 1-15.
80. Schmieden, D. T.; Basalo Vazquez, S. J.; Sanguesa, H.; van der Does, M.; Idema, T.; Meyer, A. S., Printing of Patterned, Engineered E. coli Biofilms with a Low-Cost 3D Printer. *ACS Synth Biol.* **2018,** *7* (5), 1328-1337.
81. Cui, M.; Qi, Q.; Gurry, T.; Zhao, T.; An, B.; Pu, J.; Gui, X.; Cheng, A. A.; Zhang, S.; Xun, D.; Becce, M.; Briatico-Vangosa, F.; Liu, C.; Lu, T. K.; Zhong, C., Modular genetic design of multi-domain functional amyloids: insights into self-assembly and functional properties. *Chem Sci* **2019,** *10* (14), 4004-4014.
82. Chung, W. J.; Kwon, K. Y.; Song, J.; Lee, S. W., Evolutionary screening of collagen-like peptides that nucleate hydroxyapatite crystals. *Langmuir.* **2011,** *27* (12), 7620-8.
83. Xu, B.; Zheng, P.; Gao, F.; Wang, W.; Zhang, H.; Zhang, X.; Feng, X.; Liu, W., A Mineralized High Strength and Tough Hydrogel for Skull Bone Regeneration. *Adv. Funct. Mater.* **2017,** *27* (4), 1604327.
84. Fang, J.; Li, P.; Lu, X.; Fang, L.; Lu, X.; Ren, F., A strong, tough, and osteoconductive hydroxyapatite mineralized polyacrylamide/dextran hydrogel for bone tissue regeneration. *Acta Biomater.* **2019,** *88*, 503-513.
85. Li, C.; Born, A. K.; Schweizer, T.; Zenobi-Wong, M.; Cerruti, M.; Mezzenga, R., Amyloid-hydroxyapatite bone biomimetic composites. *Adv Mater* **2014,** *26* (20), 3207-12.

86. Liu, C.; Han, Z.; Czernuszka, J. T., Gradient collagen/nanohydroxyapatite composite scaffold: development and characterization. *Acta Biomater.* **2009,** *5* (2), 661-9.
87. Shao, C.; Zhao, R.; Jiang, S.; Yao, S.; Wu, Z.; Jin, B.; Yang, Y.; Pan, H.; Tang, R., Citrate Improves Collagen Mineralization via Interface Wetting: A Physicochemical Understanding of Biomineralization Control. *Adv Mater.* **2018,** *30* (8), 1704876.
88. Raymond, D. M.; Nilsson, B. L., Multicomponent peptide assemblies. *Chem Soc Rev.* **2018,** *47* (10), 3659-3720.
89. Jeffrey D. Hartgerink, E. B., Samue, Self-Assembly and Mineralization of Peptide-Amphiphile Nanofibers. *Science.* **2001,** *294*, 1684-1688.
90. Chen, J.; Zou, X., Self-assemble peptide biomaterials and their biomedical applications. *Bioact Mater* **2019,** *4*, 120-131.
91. Rivas, M.; Del Valle, L. J.; Aleman, C.; Puiggali, J., Peptide Self-Assembly into Hydrogels for Biomedical Applications Related to Hydroxyapatite. *Gels.* **2019,** *5* (1), 14-43.
92. Jin, H. E.; Jang, J.; Chung, J.; Lee, H. J.; Wang, E.; Lee, S. W.; Chung, W. J., Biomimetic Self-Templated Hierarchical Structures of Collagen-Like Peptide Amphiphiles. *Nano Lett.* **2015,** *15* (10), 7138-45.
93. DeBenedictis, E. P.; Ma, D.; Keten, S., Structural predictions for curli amyloid fibril subunits CsgA and CsgB. *RSC Adv.* **2017,** *7* (76), 48102-48112.
94. Eswar, N.; Webb, B.; Marti-Renom, M. A.; Madhusudhan, M. S.; Eramian, D.; Shen, M. Y.; Pieper, U.; Sali, A., Comparative protein structure modeling using Modeller. *Curr Protoc Bioinformatics.* **2006,** *47*, 5.6.1-32.
95. Dunbar, M.; DeBenedictis, E.; Keten, S., Dimerization energetics of curli fiber subunits CsgA and CsgB. *Npj Comput. Mater.* **2019,** *5* (1), 27-36.
96. James C. Phillips, R. B., Wei Wang, James Gumbart, Emad Tajkhorshid, Elizabeth Villa, Christophe Chipot, Robert D. Skeel, Laxmikant Kalé, and Klaus Schulten, Scalable Molecular Dynamics with NAMD. *J Comput Chem.* **2005,** *26* (16), 1781–1802.
97. A. D. MacKerell, J., D. Bashford, M. Bellott, R. L. Dunbrack, Jr., D. Evanseck, M. J. Field, S. Fischer, J. Gao, H. Guo, S. Ha, D. Joseph-McCarthy, L. Kuchnir, K. Kuczera, F. T. K. Lau, C. Mattos, S. Michnick, T. Ngo, D. T. Nguyen, B. Prodhom, W. E. Reiher, B. Roux, M. Schlenkrich, J. C. Smith, R. Stote, J. Straub, M. Watanabe, J. Wio´rkiewicz-Kuczera, D. Yin, and M. Karplus, All-Atom Empirical Potential for Molecular Modeling and Dynamics Studies of Proteins. *J. Phys. Chem. B.* **1998,** *102*, 3586-3616.
98. Best, R. B.; Zhu, X.; Shim, J.; Lopes, P. E.; Mittal, J.; Feig, M.; Mackerell, A. D., Jr., Optimization of the additive CHARMM all-atom protein force field targeting improved sampling of the backbone phi, psi and side-chain chi(1) and chi(2) dihedral angles. *J Chem Theory Comput.* **2012,** *8* (9), 3257-3273.
99. Alexander D. MacKerell, J., Michael Feig, and Charles L. Brooks, Improved Treatment of the Protein Backbone in Empirical Force Fields. *J. Am. Chem. Soc.* **2004,** *126*, 698-699.
100. Mahato, A.; Sandy, Z.; Bysakh, S.; Hupa, L.; Das, I.; Bhattacharjee, P.; Kundu, B.; De, G.; Nandi, S. K.; Vallittu, P.; Balla, V. K.; Bhattacharya, M., Development of nano-porous hydroxyapatite coated e-glass for potential bone-tissue engineering application: An in vitro approach. *Mater. Sci. Eng. C.* **2020,** *111*, 110764.
101. Calabro, E., Competition between hydrogen bonding and protein aggregation in neuronal-like cells under exposure to 50 Hz magnetic field. *Int J Radiat Biol.* **2016,** *92* (7), 395-403.

102. Dueholm, M. S.; Nielsen, S. B.; Hein, K. L.; Nissen, P.; Chapman, M.; Christiansen, G.; Nielsen, P. H.; Otzen, D. E., Fibrillation of the major curli subunit CsgA under a wide range of conditions implies a robust design of aggregation. *Biochemistry.* **2011,** *50* (39), 8281-90.
103. Tufail, S.; Sherwani, M. A.; Shoaib, S.; Azmi, S.; Owais, M.; Islam, N., Ovalbumin self-assembles into amyloid nanosheets that elicit immune responses and facilitate sustained drug release. *J Biol Chem* **2018,** *293* (29), 11310-11324.
104. Hammer, N. D.; McGuffie, B. A.; Zhou, Y.; Badtke, M. P.; Reinke, A. A.; Brannstrom, K.; Gestwicki, J. E.; Olofsson, A.; Almqvist, F.; Chapman, M. R., The C-terminal repeating units of CsgB direct bacterial functional amyloid nucleation. *J Mol Biol.* **2012,** *422* (3), 376-89.
105. Wang, X.; Zhou, Y.; Ren, J. J.; Hammer, N. D.; Chapman, M. R., Gatekeeper residues in the major curlin subunit modulate bacterial amyloid fiber biogenesis. *Proc Natl Acad Sci U S A.* **2010,** *107* (1), 163-8.
106. Qi, Q., Zhao, T. X., An, B. L., Liu, X.Y., Zhong, C, Self-assembly and morphological characterization of two-component functional amyloid proteins. *Chin. Chem. Lett.* **2017,** *28* (5), 1062-1068.
107. Brown, P. D., Structural Characterization. In *Springer Handbook of Electronic and Photonic Materials.*, S. Kasap, P. C., Ed. Springer, Cham: 2017; pp 385-412.
108. Poralan, G. M.; Gambe, J. E.; Alcantara, E. M.; Vequizo, R. M., X-ray diffraction and infrared spectroscopy analyses on the crystallinity of engineered biological hydroxyapatite for medical application. *IOP Conf Ser Mater Sci Eng.* **2015,** *79*, 012028.
109. Tavafoghi, M.; Cerruti, M., The role of amino acids in hydroxyapatite mineralization. *J R Soc Interface.* **2016,** *13* (123), 20160462.
110. Kalaiselvi, V.; Mathammal, R.; Vijayakumar, S.; Vaseeharan, B., Microwave assisted green synthesis of Hydroxyapatite nanorods using Moringa oleifera flower extract and its antimicrobial applications. *Int J Vet Sci Med.* **2018,** *6* (2), 286-295.
111. Song, F.; Zhang, H.; Wang, S.; Liu, L.; Tan, X.; Liu, S., Atomic-level design of CoOH(+)-hydroxyapatite@C catalysts for superfast degradation of organics via peroxymonosulfate activation. *Chem Commun (Camb).* **2018,** *54* (39), 4919-4922.
112. Wei, G.; Zhang, J.; Xie, L.; Jandt, K. D., Biomimetic growth of hydroxyapatite on super water-soluble carbon nanotube-protein hybrid nanofibers. *Carbon.* **2011,** *49* (7), 2216-2226.
113. Fertala, A., Three Decades of Research on Recombinant Collagens: Reinventing the Wheel or Developing New Biomedical Products? *Bioengineering (Basel)* **2020,** *7* (4), 155.
114. Lukomski, S.; Nakashima, K.; Abdi, I.; Cipriano, V. J.; Shelvin, B. J.; Graviss, E. A.; Musser, J. M., Identification and characterization of a second extracellular collagen-like protein made by group A Streptococcus: control of production at the level of translation. *Infect Immun* **2001,** *69* (3), 1729.
115. Xu, Y.; Keene, D. R.; Bujnicki, J. M.; Hook, M.; Lukomski, S., Streptococcal Scl1 and Scl2 proteins form collagen-like triple helices. *J Biol Chem* **2002,** *277* (30), 27312.
116. O'Leary, L. E.; Fallas, J. A.; Bakota, E. L.; Kang, M. K.; Hartgerink, J. D., Multi-hierarchical self-assembly of a collagen mimetic peptide from triple helix to nanofibre and hydrogel. *Nat Chem* **2011,** *3* (10), 821-8.
117. Fallas, J. A.; Dong, J.; Tao, Y. J.; Hartgerink, J. D., Structural insights into charge pair interactions in triple helical collagen-like proteins. *J Biol Chem* **2012,** *287* (11), 8039.
118. Nenninger, A. A.; Robinson, L. S.; Hammer, N. D.; Epstein, E. A.; Badtke, M. P.; Hultgren, S. J.; Chapman, M. R., CsgE is a curli secretion specificity factor that prevents amyloid fibre aggregation. *Mol Microbiol* **2011,** *81* (2), 486.

119. Cholas, R.; Kunjalukkal Padmanabhan, S.; Gervaso, F.; Udayan, G.; Monaco, G.; Sannino, A.; Licciulli, A., Scaffolds for bone regeneration made of hydroxyapatite microspheres in a collagen matrix. *Mater Sci Eng C Mater Biol Appl* **2016,** *63*, 499-505.
120. Abdali, Z.; Aminzare, M.; Zhu, X.; DeBenedictis, E.; Xie, O.; Keten, S.; Dorval Courchesne, N. M., Curli-Mediated Self-Assembly of a Fibrous Protein Scaffold for Hydroxyapatite Mineralization. *ACS Synth Biol* **2020,** *9* (12), 3334.
121. Delgado, L. M.; Shologu, N.; Fuller, K.; Zeugolis, D. I., Acetic acid and pepsin result in high yield, high purity and low macrophage response collagen for biomedical applications. *Biomed Mater* **2017,** *12* (6), 065009.
122. Qing, G.; Ma, L. C.; Khorchid, A.; Swapna, G. V.; Mal, T. K.; Takayama, M. M.; Xia, B.; Phadtare, S.; Ke, H.; Acton, T.; Montelione, G. T.; Ikura, M.; Inouye, M., Cold-shock induced high-yield protein production in Escherichia coli. *Nat Biotechnol* **2004,** *22* (7), 877.
123. Johnston, N.; Dettmar, P. W.; Bishwokarma, B.; Lively, M. O.; Koufman, J. A., Activity/stability of human pepsin: implications for reflux attributed laryngeal disease. *Laryngoscope* **2007,** *117* (6), 1036.
124. Meredith, S. C., The determination of molecular weight of proteins by gel permeation chromatography in organic solvents. *Journal of Biological Chemistry* **1984,** *259* (19), 11682.
125. Rittié, L., Method for Picrosirius Red-Polarization Detection of Collagen Fibers in Tissue Sections. *Methods Mol Biol* **2017,** *1627*, 395.
126. Ueda, E. K. M.; Gout, P. W.; Morganti, L., Current and prospective applications of metal ion–protein binding. *Journal of Chromatography A* **2003,** *988* (1), 1-23.
127. Li, Y.; Asadi, A.; Monroe, M. R.; Douglas, E. P., pH effects on collagen fibrillogenesis in vitro: Electrostatic interactions and phosphate binding. *Materials Science and Engineering: C* **2009,** *29* (5), 1643.
128. Usha, R.; Raman, S. S.; Subramanian, V.; Ramasami, T., Role of polyols (erythritol, xylitol and sorbitol) on the structural stabilization of collagen. *Chemical Physics Letters* **2006,** *430* (4-6), 391.
129. Li, F.; Ducker, M.; Sun, B.; Szele, F. G.; Czernuszka, J. T., Interpenetrating polymer networks of collagen, hyaluronic acid, and chondroitin sulfate as scaffolds for brain tissue engineering. *Acta Biomater* **2020,** *112*, 122.
130. Sarkar, B.; O'Leary, L. E.; Hartgerink, J. D., Self-assembly of fiber-forming collagen mimetic peptides controlled by triple-helical nucleation. *J Am Chem Soc* **2014,** *136* (41), 14417.
131. Kohler, M.; Marchand, A.; Hentzen, N. B.; Egli, J.; Begley, A. I.; Wennemers, H.; Zenobi, R., Temperature-controlled electrospray ionization mass spectrometry as a tool to study collagen homo- and heterotrimers. *Chem Sci* **2019,** *10* (42), 9829.
132. Tanrikulu, I. C.; Forticaux, A.; Jin, S.; Raines, R. T., Peptide tessellation yields micrometre-scale collagen triple helices. *Nat Chem* **2016,** *8* (11), 1008.
133. Hulgan, S. A. H.; Jalan, A. A.; Li, I. C.; Walker, D. R.; Miller, M. D.; Kosgei, A. J.; Xu, W.; Phillips, G. N., Jr.; Hartgerink, J. D., Covalent Capture of Collagen Triple Helices Using Lysine-Aspartate and Lysine-Glutamate Pairs. *Biomacromolecules* **2020,** *21* (9), 3772.
134. Drzewiecki, K. E.; Grisham, D. R.; Parmar, A. S.; Nanda, V.; Shreiber, D. I., Circular Dichroism Spectroscopy of Collagen Fibrillogenesis: A New Use for an Old Technique. *Biophys J* **2016,** *111* (11), 2377.
135. Xu, C.; Yu, Z.; Inouye, M.; Brodsky, B.; Mirochnitchenko, O., Expanding the family of collagen proteins: recombinant bacterial collagens of varying composition form triple-helices of similar stability. *Biomacromolecules* **2010,** *11* (2), 348-56.

136. Wei, Y.; Thyparambil, A. A.; Latour, R. A., Protein helical structure determination using CD spectroscopy for solutions with strong background absorbance from 190 to 230nm. *Biochim Biophys Acta* **2014,** *1844* (12), 2331.
137. E. Leikina, M. V. M., N. Kuznetsova, and S. Leikin, Type I collagen is thermally unstable at body temperature. *PNAS* **2002,** *99*, 1314–131.
138. Bruce G. Frushour, J. L. K., Raman Scattering of Collagen, Gelatin, and Elastin. *Biopolymers* **1975,** *14*, 379.
139. Lefevre, T.; Paquet-Mercier, F.; Rioux-Dube, J. F.; Pezolet, M., Review structure of silk by raman spectromicroscopy: from the spinning glands to the fibers. *Biopolymers* **2012,** *97* (6), 322.
140. Khalid, M.; Bora, T.; Ghaithi, A. A.; Thukral, S.; Dutta, J., Raman Spectroscopy detects changes in Bone Mineral Quality and Collagen Cross-linkage in Staphylococcus Infected Human Bone. *Sci Rep* **2018,** *8* (1), 9417.
141. Ikoma, T.; Kobayashi, H.; Tanaka, J.; Walsh, D.; Mann, S., Physical properties of type I collagen extracted from fish scales of Pagrus major and Oreochromis niloticas. *International Journal of Biological Macromolecules* **2003,** *32* (3-5), 199.
142. Olsztyńska-Janus, S.; Szymborska-Małek, K.; Gąsior-Głogowska, M.; Walski, T.; Komorowska, M.; Witkiewicz, W.; Pezowicz, C.; Kobielarz, M.; Szotek, S., Spectroscopic techniques in the study of human tissues and their components. Part II: Raman spectroscopy. *Acta of Bioengineering and Biomechanics* **2012,** *14* (4), 101.
143. Haase, H.; Jordan, L.; Keitel, L.; Keil, C.; Mahltig, B., Comparison of methods for determining the effectiveness of antibacterial functionalized textiles. *PLoS One* **2017,** *12* (11), e0188304.
144. Bandekar, J., Amide modes and protein conformation. *Biochimica et Biophsica Acta* **1992,** *1120*, 123.
145. Chattopadhyay, S.; Raines, R. T., Review collagen-based biomaterials for wound healing. *Biopolymers* **2014,** *101* (8), 821.
146. Long, G.; Liu, D.; He, X.; Shen, Y.; Zhao, Y.; Hou, X.; Chen, B.; OuYang, W.; Dai, J.; Li, X., A dual functional collagen scaffold coordinates angiogenesis and inflammation for diabetic wound healing. *Biomater Sci* **2020,** *8* (22), 6337.
147. Wu, X.; Hou, J.; Li, M.; Wang, J.; Kaplan, D. L.; Lu, S., Sodium dodecyl sulfate-induced rapid gelation of silk fibroin. *Acta Biomater* **2012,** *8* (6), 2185-92.
148. Duraj-Thatte, A. M.; Courchesne, N. D.; Praveschotinunt, P.; Rutledge, J.; Lee, Y.; Karp, J. M.; Joshi, N. S., Genetically Programmable Self-Regenerating Bacterial Hydrogels. *Adv Mater* **2019,** *31* (40), 1901826.
149. Lee, C. H.; Singla, A.; Lee, Y., Biomedical applications of collagen. *Int J Pharm* **2001,** *221* (1-2), 1-22.
150. Yu, L.; Wei, M., Biomineralization of Collagen-Based Materials for Hard Tissue Repair. *International Journal of Molecular Sciences* **2021,** *22* (2), 944.
151. Ehrlich, H., Chitin and collagen as universal and alternative templates in biomineralization. *International Geology Review* **2010,** *52* (7-8), 661-699.
152. Sobczak-Kupiec, A.; Drabczyk, A.; Florkiewicz, W.; Glab, M.; Kudlacik-Kramarczyk, S.; Slota, D.; Tomala, A.; Tyliszczak, B., Review of the Applications of Biomedical Compositions Containing Hydroxyapatite and Collagen Modified by Bioactive Components. *Materials (Basel)* **2021,** *14* (9).

153. Schneiders, W.; Reinstorf, A.; Pompe, W.; Grass, R.; Biewener, A.; Holch, M.; Zwipp, H.; Rammelt, S., Effect of modification of hydroxyapatite/collagen composites with sodium citrate, phosphoserine, phosphoserine/RGD-peptide and calcium carbonate on bone remodelling. *Bone* **2007,** *40* (4), 1048-59.
154. Fernandes, F. M.; Coradin, T.; Aime, C., Self-Assembly in Biosilicification and Biotemplated Silica Materials. *Nanomaterials (Basel)* **2014,** *4* (3), 792-812.
155. Yorseng, K.; Siengchin, S.; Ashok, B.; Rajulu, A. V., Nanocomposite egg shell powder with in situ generated silver nanoparticles using inherent collagen as reducing agent. *Journal of Bioresources and Bioproducts* **2020,** *5* (2), 101-107.
156. Aryal, S.; Bahadur K. C, R.; Bhattarai, S. R.; Prabu, P.; Kim, H. Y., Immobilization of collagen on gold nanoparticles: preparation, characterization, and hydroxyapatite growth. *Journal of Materials Chemistry* **2006,** *16* (48).
157. Qiu, Y.; Zhai, C.; Chen, L.; Liu, X.; Yeo, J., Current Insights on the Diverse Structures and Functions in Bacterial Collagen-like Proteins. *ACS Biomater Sci Eng* **2021**.
158. Yu, Z.; An, B.; Ramshaw, J. A. M.; Brodsky, B., Bacterial collagen-like proteins that form triple-helical structures. *Journal of Structural Biology* **2014,** *186* (3), 451-461.
159. Mohs, A.; Silva, T.; Yoshida, T.; Amin, R.; Lukomski, S.; Inouye, M.; Brodsky, B., Mechanism of Stabilization of a Bacterial Collagen Triple Helix in the Absence of Hydroxyproline. *Journal of Biological Chemistry* **2007,** *282* (41), 29757-29765.
160. Abdali, Z.; Renner-Rao, M.; Chow, A.; Cai, A.; Harrington, M. J.; Dorval Courchesne, N. M., Extracellular Secretion and Simple Purification of Bacterial Collagen from Escherichia coli. *Biomacromolecules* **2022,** *23* (4), 1557-1568.
161. Hu, J.; Wang, J.; Zhu, X.; Tu, R. S.; Nanda, V.; Xu, F., Design Strategies to Tune the Structural and Mechanical Properties of Synthetic Collagen Hydrogels. *Biomacromolecules* **2021,** *22* (8), 3440-3450.
162. Golser, A.; Scheibel, T., Routes towards Novel Collagen-Like Biomaterials. *Fibers* **2018,** *6* (2).
163. Oosterlaken, B. M.; Vena, M. P.; With, G., In Vitro Mineralization of Collagen. *Advanced Materials* **2021,** *33* (16), 2004418.
164. Fahmy, H. M.; Mosleh, A. M.; Elghany, A. A.; Shams-Eldin, E.; Abu Serea, E. S.; Ali, S. A.; Shalan, A. E., Coated silver nanoparticles: synthesis, cytotoxicity, and optical properties. *RSC Advances* **2019,** *9* (35), 20118-20136.
165. Abdali, Z.; Yeganeh, H.; Solouk, A.; Gharibi, R.; Sorayya, M., Thermoresponsive antimicrobial wound dressings via simultaneous thiol-ene polymerization and in situ generation of silver nanoparticles. *RSC Adv.* **2015,** *5* (81), 66024-66036.
166. Bapat, R. A.; Chaubal, T. V.; Joshi, C. P.; Bapat, P. R.; Choudhury, H.; Pandey, M.; Gorain, B.; Kesharwani, P., An overview of application of silver nanoparticles for biomaterials in dentistry. *Mater Sci Eng C Mater Biol Appl* **2018,** *91*, 881-898.
167. Dorval Courchesne, N.-M.; Klug, M. T.; Huang, K. J.; Weidman, M. C.; Cantú, V. J.; Chen, P.-Y.; Kooi, S. E.; Yun, D. S.; Tisdale, W. A.; Fang, N. X.; Belcher, A. M.; Hammond, P. T., Constructing Multifunctional Virus-Templated Nanoporous Composites for Thin Film Solar Cells: Contributions of Morphology and Optics to Photocurrent Generation. *The Journal of Physical Chemistry C* **2015,** *119* (25), 13987-14000.
168. Cardoso, V. S.; Quelemes, P. V.; Amorin, A.; Primo, F. L.; Gobo, G. G.; Tedesco, A. C.; Mafud, A. C.; Mascarenhas, Y. P.; Corrêa, J. R.; Kuckelhaus, S. A.; Eiras, C.; Leite, J. R.

S.; Silva, D.; Dos Santos Júnior, J. R., Collagen-based silver nanoparticles for biological applications: synthesis and characterization. *Journal of Nanobiotechnology* **2014,** *12* (1).
169. Jiang, X. C.; Chen, C. Y.; Chen, W. M.; Yu, A. B., Role of citric acid in the formation of silver nanoplates through a synergistic reduction approach. *Langmuir* **2010,** *26* (6), 4400-8.
170. Kumar, A.; Kumar, V., Biotemplated Inorganic Nanostructures: Supramolecular Directed Nanosystems of Semiconductor(s)/Metal(s) Mediated by Nucleic Acids and Their Properties. *Chemical Reviews* **2014,** *114* (14), 7044-7078.
171. Huang, J.; Lin, L.; Sun, D.; Chen, H.; Yang, D.; Li, Q., Bio-inspired synthesis of metal nanomaterials and applications. *Chemical Society Reviews* **2015,** *44* (17), 6330-6374.
172. Liu, H.; Zhang, H.; Wang, J.; Wei, J., Effect of temperature on the size of biosynthesized silver nanoparticle: Deep insight into microscopic kinetics analysis. *Arabian Journal of Chemistry* **2020,** *13* (1), 1011-1019.
173. Agnihotri, S.; Mukherji, S.; Mukherji, S., Size-controlled silver nanoparticles synthesized over the range 5–100 nm using the same protocol and their antibacterial efficacy. *RSC Adv.* **2014,** *4* (8), 3974-3983.
174. Chen, D.; Qiao, X.; Qiu, X.; Chen, J., Synthesis and electrical properties of uniform silver nanoparticles for electronic applications. *Journal of Materials Science* **2009,** *44* (4), 1076-1081.
175. Jebril, S.; Khanfir Ben Jenana, R.; Dridi, C., Green synthesis of silver nanoparticles using Melia azedarach leaf extract and their antifungal activities: In vitro and in vivo. *Materials Chemistry and Physics* **2020,** *248*, 122898.
176. Jemal, K.; Sandeep, B. V.; Pola, S., Synthesis, Characterization, and Evaluation of the Antibacterial Activity ofAllophylus serratusLeaf and Leaf Derived Callus Extracts Mediated Silver Nanoparticles. *Journal of Nanomaterials* **2017,** *2017*, 1-11.
177. Dilshad, E.; Bibi, M.; Sheikh, N.; Tamrin, K. F.; Mansoor, Q.; Maqbool, Q.; Nawaz, M., Synthesis of Functional Silver Nanoparticles and Microparticles with Modifiers and Evaluation of Their Antimicrobial, Anticancer, and Antioxidant Activity. *Journal of Functional Biomaterials* **2020,** *11*.
178. Yin, I. X.; Zhang, J.; Zhao, I. S.; Mei, M. L.; Li, Q.; Chu, C. H., The Antibacterial Mechanism of Silver Nanoparticles and Its Application in Dentistry. *International journal of nanomedicine* **2020,** *15*, 2555-2562.
179. Abdali, Z.; Logsetty, S.; Liu, S., Bacteria-Responsive Single and Core-Shell Nanofibrous Membranes Based on Polycaprolactone/Poly(ethylene succinate) for On-Demand Release of Biocides. *ACS Omega* **2019,** *4* (2), 4063-4070.
180. Jayaraman, P.; Gandhimathi, C.; Venugopal, J. R.; Becker, D. L.; Ramakrishna, S.; Srinivasan, D. K., Controlled release of drugs in electrosprayed nanoparticles for bone tissue engineering. *Adv Drug Deliv Rev* **2015,** *94*, 77-95.
181. Rodriguez-Acosta, H.; Tapia-Rivera, J. M.; Guerrero-Guzman, A.; Hernandez-Elizarraraz, E.; Hernandez-Diaz, J. A.; Garza-Garcia, J. J. O.; Perez-Ramirez, P. E.; Velasco-Ramirez, S. F.; Ramirez-Anguiano, A. C.; Velazquez-Juarez, G.; Velazquez-Lopez, J. M.; Sanchez-Toscano, Y. G.; Garcia-Morales, S.; Flores-Fonseca, M. M.; Garcia-Bustos, D. E.; Sanchez-Chipres, D. R.; Zamudio-Ojeda, A., Chronic wound healing by controlled release of chitosan hydrogels loaded with silver nanoparticles and calendula extract. *J Tissue Viability* **2022,** *31* (1), 173-179.
182. Du, T.; Niu, X.; Li, Z.; Li, P.; Feng, Q.; Fan, Y., Crosslinking induces high mineralization of apatite minerals on collagen fibers. *Int J Biol Macromol* **2018,** *113*, 450-457.

183. Keogh, M. B.; FJ, O. B.; Daly, J. S., A novel collagen scaffold supports human osteogenesis--applications for bone tissue engineering. *Cell Tissue Res* **2010,** *340* (1), 169-77.
184. Chan, E. C.; Kuo, S. M.; Kong, A. M.; Morrison, W. A.; Dusting, G. J.; Mitchell, G. M.; Lim, S. Y.; Liu, G. S., Three Dimensional Collagen Scaffold Promotes Intrinsic Vascularisation for Tissue Engineering Applications. *PLoS One* **2016,** *11* (2), e0149799.
185. Shuai, C.; Yang, W.; Feng, P.; Peng, S.; Pan, H., Accelerated degradation of HAP/PLLA bone scaffold by PGA blending facilitates bioactivity and osteoconductivity. *Bioact Mater* **2021,** *6* (2), 490-502.
186. Sl Shanthi, P. M.; Ashok, M.; Balasubramanian, T.; Riyasdeen, A.; Akbarsha, M. A., Synthesis and characterization of nano-hydroxyapatite at ambient temperature using cationic surfactant. *Materials Letters* **2009,** *63* (24-25), 2123-2125.
187. Iafisco, M.; Foltran, I.; Sabbatini, S.; Tosi, G.; Roveri, N., Electrospun nanostructured fibers of collagen-biomimetic apatite on titanium alloy. *Bioinorg Chem Appl* **2012,** *2012*, 123953.
188. Horvat, G.; Pantic, M.; Knez, Z.; Novak, Z., Preparation and characterization of polysaccharide - silica hybrid aerogels. *Sci Rep* **2019,** *9* (1), 16492.
189. Valliant, E. M.; Turdean-Ionescu, C. A.; Hanna, J. V.; Smith, M. E.; Jones, J. R., Role of pH and temperature on silica network formation and calcium incorporation into sol–gel derived bioactive glasses. *J. Mater. Chem.* **2012,** *22* (4), 1613-1619.
190. Eivazzadeh-Keihan, R.; Chenab, K. K.; Taheri-Ledari, R.; Mosafer, J.; Hashemi, S. M.; Mokhtarzadeh, A.; Maleki, A.; Hamblin, M. R., Recent advances in the application of mesoporous silica-based nanomaterials for bone tissue engineering. *Mater Sci Eng C Mater Biol Appl* **2020,** *107*, 110267.
191. Perumal, S.; Ramadass, S.; Madhan, B., Sol-gel processed mupirocin silica microspheres loaded collagen scaffold: a synergistic bio-composite for wound healing. *Eur J Pharm Sci* **2014,** *52*, 26-33.
192. Darmakkolla, S. R.; Tran, H.; Gupta, A.; Rananavare, S. B., A method to derivatize surface silanol groups to Si-alkyl groups in carbon-doped silicon oxides. *RSC Advances* **2016,** *6* (95), 93219-93230.
193. Ding, Y.; Chu, X.; Hong, X.; Zou, P.; Liu, Y., The infrared fingerprint signals of silica nanoparticles and its application in immunoassay. *Applied Physics Letters* **2012,** *100* (1).
194. Andrade, Â. L.; Ferreira, J. M. F.; Domingues, R. Z., Zeta potential measurement in bioactive collagen. *Materials Research* **2004,** *7* (4), 631-634.
195. Lewandowska-Lancucka, J.; Fiejdasz, S.; Rodzik, L.; Koziel, M.; Nowakowska, M., Bioactive hydrogel-nanosilica hybrid materials: a potential injectable scaffold for bone tissue engineering. *Biomed Mater* **2015,** *10* (1), 015020.
196. Narciso, A. M.; da Rosa, C. G.; Nunes, M. R.; Sganzerla, W. G.; Hansen, C. M.; de Melo, A. P. Z.; Paes, J. V.; Bertoldi, F. C.; Barreto, P. L. M.; Masiero, A. V., Antimicrobial green silver nanoparticles in bone grafts functionalization for biomedical applications. *Biocatalysis and Agricultural Biotechnology* **2021,** *35*.